

**Deep Learning-based Forecasting and Energy
Management Algorithms for Smart Grid Applications**

by

Amirhossein Dolatabadi

A thesis submitted in partial fulfillment of the requirements for the degree of

Doctor of Philosophy

in

Energy Systems

Department of Electrical and Computer Engineering
University of Alberta

Abstract

With the increasing global problems concerning energy security and climate change, new challenges in social progress and human survival have come to the fore. Requiring no fuel, and being renewable and non-polluting, renewable energy (RE) resources, typically from photovoltaic and wind sources, have attracted extensive attention worldwide. However, due to their stochasticity, uncertainty, and intermittency, RE resources could pose considerable challenges to the optimal operation of the energy systems despite their non-polluting and widely available nature. This changing environment necessitates the accurate and efficient operation of the RE-integrated energy system. On the other hand, the rapidly growing applications of artificial intelligence and machine learning techniques can contribute to reducing energy costs, maintaining the balance between generation and demand, and satisfying consumers' needs.

The existing literature on the scheduling and operation of active distribution systems falls short in several aspects, such as RE prediction performance, cost-effective operation, and realistic scheduling. This research aims to 1) develop a new deep learning-based model integrating the discrete wavelet packet transform (DWPT) and bidirectional long short-term memory (BLSTM) to capture deep temporal features of wind speed time series precisely, 2) investigate a light detection and ranging (LiDAR)-aided deep learning model to learn the powerful spatial-temporal characteristics from the input wind fields,

3) propose a novel model-free deep reinforcement learning (DRL) approach to optimize the compressed air energy storage (CAES) energy arbitrage in the presence of a solar irradiance forecasting model, 4) utilize a deep deterministic policy gradient (DDPG) framework to develop an intelligent controller to schedule the energy hub optimally, and 5) analyze the optimal operation of the biogas-integrated multi-source multi-product facility in the presence of the supervised federated neural architecture search (SFnAS) technique.

The first study in this thesis applies the DWPT to extract the features of the wind time series. It then uses the BLSTM network as a combination of LSTM networks and bidirectional RNNs to capture deep temporal features with high abstraction. The second study extends the network of the first work by combining it with 2-D convolutional neural networks (CNNs) for capturing high levels of abstractions in the wind fields provided by LiDAR. In the third study, the CNN-BLSTM model presented in the second work is used to train a DRL agent that optimizes the self-scheduling of the CAES-PV system. The fourth study upgrades the DRL framework of the third work by introducing the DDPG for more smooth control actions. Finally, the fifth study investigates the dynamic scheduling framework for an energy hub with a biomass-solar hybrid renewable system. Furthermore, an SFNAS technique has been presented to eliminate the need for manual engineering of deep neural network models and the unnecessary computational burden associated with them. The comparative results based on realistic case studies demonstrate the effectiveness and applicability of the proposed frameworks compared to the state-of-the-art methods in the recent literature.

Preface

This thesis is an original work by Amirhossein Dolatabadi. As detailed in the following, some chapters of this thesis have been published or submitted for publication as scholarly articles in which Professor Yasser Abdel-Rady I. Mohamed was the supervisory author and has contributed to concepts formation and the manuscript composition.

A version of Chapter 3 has been published as:

- A. Dolatabadi, H. Abdeltawab and Y. A. -R. I. Mohamed, "Hybrid Deep Learning-Based Model for Wind Speed Forecasting Based on DWPT and Bidirectional LSTM Network," in *IEEE Access*, vol. 8, pp. 229219-229232, 2020, doi: 10.1109/ACCESS.2020.3047077.

A version of Chapter 4 has been published as:

- A. Dolatabadi, H. Abdeltawab and Y. A. -R. I. Mohamed, "Deep Spatial-Temporal 2-D CNN-BLSTM Model for Ultrashort-Term LiDAR-Assisted Wind Turbine's Power and Fatigue Load Forecasting," in *IEEE Transactions on Industrial Informatics*, vol. 18, no. 4, pp. 2342-2353, April 2022, doi: 10.1109/TII.2021.3097716.

A version of Chapter 5 has been published as:

- A. Dolatabadi, H. Abdeltawab and Y. A. -R. I. Mohamed, "Deep Reinforcement Learning-Based Self-Scheduling Strategy for a CAES-PV System Using Accurate Sky Images-Based Forecasting," in *IEEE Transactions on Power Systems*, vol. 38, no. 2, pp. 1608-1618, March 2023, doi: 10.1109/TPWRS.2022.3177704.

A version of Chapter 6 has been published as:

- A. Dolatabadi, H. Abdeltawab and Y. A. -R. I. Mohamed, "A Novel Model-Free Deep Reinforcement Learning Framework for Energy Management of a PV Integrated Energy Hub," in *IEEE Transactions on Power Systems*, 2022, doi: 10.1109/TPWRS.2022.3212938.

Materials in Chapter 7 have been submitted as three articles:

- A. Dolatabadi, H. Abdeltawab and Y. A. -R. I. Mohamed, "SFNAS-DDPG: A Biomass-based Energy Hub Dynamic Scheduling Approach via Connecting Supervised Federated Neural Architecture Search and Deep Deterministic Policy Gradient," submitted to the *IEEE Transactions on Industrial Informatics*.
- A. Dolatabadi, H. Abdeltawab and Y. A. -R. I. Mohamed, "Evolutionary-Based Neural Architecture Search for An Efficient CAES and PV Farm Joint Operation Strategy Using Deep Reinforcement Learning" IEEE PES GTD International Conference and Exposition, 2023, 5-pages, accepted for presentation.
- A. Dolatabadi, H. Abdeltawab and Y. A. -R. I. Mohamed, "An Improved Actor-Critic Reinforcement Learning with Neural Architecture Search for the Optimal Control Strategy of a Multi-Carrier Energy System", IEEE PES GTD International Conference and Exposition 2023, 5-pages, accepted for presentation.

To My Mom, Dad, and My Beloved Wife

Acknowledgements

I would like to express my sincere gratitude to my supervisor, Prof. Yasser Abdel-Rady I. Mohamed. His great support and supervision during this work have helped me immensely in shaping my research goals and have, collectively, been vital to the completion of this thesis. This research and dissertation would not have been possible without his suggestions and comments on my work and ideas that have helped me refine and evolve them efficiently. Along the same note, I would also like to thank Dr. Hussein M. Abdeltawab for offering his precious time and valuable feedback on my work.

Also, I would like to extend special thanks to my examining committee members, Prof. Yasser A. I. Mohamed, Prof. Venkata Dinavahi, Prof. Hao Liang, Prof. Xingyu Li, and Prof. Xiaozhe Wang for taking the time to review this thesis.

I would like to gratefully acknowledge the financial support provided by the Alberta Innovates Graduate Student Scholarships for Data-enabled Innovation program (GSS-DEI). I am truly honored and thankful to receive this prestigious scholarship.

Finally, and on a personal note, I need to express my gratitude and appreciation for everything that my parents and my brother has done for me; this thesis is dedicated to them. My warmest appreciation also extends to my beloved wife, Haniyeh. She has helped me stay mentally fit and has stood by my side through the thick and thin of life. I would also like to thank Prof. Behnam Mohammadi ivatloo from my alma mater who initiated me into the world of power systems.

Contents

1 Introduction	1
1.1 Background	1
1.2 Research Motivations	2
1.3 Research Objectives	4
1.4 Research Methodology	5
1.5 Research Contributions	7
1.6 Thesis Organization	7
2 Literature Survey	9
2.1 Deep Learning-based Forecasting Approaches	9
2.1.1 Wind Speed Time Series Prediction	10
2.1.2 Wind Turbine's Power and Fatigue Load Forecasting .	13
2.2 Deep Reinforcement Learning-based Energy Management Al-	
gorithms	14
2.2.1 Self-Scheduling Strategy for a CAES-PV System	14
2.2.2 Energy Management of a PV Integrated Energy Hub .	17
2.2.3 Dynamic Scheduling of a Biogas-Based Energy Hub in	
the presence of neural architecture search (NAS)	21
3 Deep Learning-Based Model for Wind Speed Forecasting Based	
on DWPT and Bidirectional LSTM Network	26
3.1 Methodology	27
3.1.1 Delay Embedding and Dynamic Reconstruction Theory	27
3.1.2 Time-Series Decomposition	28

3.1.3 Bidirectional Long Short-Term Memory (BLSTM) Net-	
work	32
3.2 Realistic Wind Speed Forecasting Case Study Definition	34
 3.2.1 Datasets	34
 3.2.2 Parameter Details	36
 3.2.3 Evaluation Criteria	38
3.3 Experimental Results and Discussion	38
 3.3.1 NREL M2 Wind Speed Dataset	39
 3.3.2 Edmonton Wind Speed Dataset	45
 3.3.3 Multivariate Forecasting Task	48
3.4 Conclusion	49
4 Deep Spatial-Temporal 2-D CNN-BLSTM Model for Ultra-	
Short-Term LiDAR-Assisted Wind Turbine's Power and Fa-	
tigue Load Forecasting	50
 4.1 Principle of LiDAR Measurements	51
 4.2 Background Theories	52
 4.2.1 Wind Turbine Modeling	52
 4.2.2 Convolutional Neural Network (CNN)	54
 4.2.3 Bidirectional Long Short-Term Memory (BLSTM) Net-	
 work	56
 4.3 Case Study and Numerical Results	56
 4.3.1 Wind Turbine Simulation Environment	56
 4.3.2 TurbSim Wind Field Simulator	56
 4.3.3 FAST Wind Turbine Simulator:	57
 4.3.4 Data Description	58
 4.3.5 Evaluation Criteria For Wind Turbine Response Fore-	
 casting	59
 4.3.6 Results and Comparisons	59
 4.4 Conclusion	70

5 Deep Reinforcement Learning-Based Self-scheduling Strategy for a CAES-PV System Using Accurate Sky Images-Based Forecasting	71
5.1 Environment Model and The Hybrid Forecasting Framework	72
5.1.1 CAES Modeling	73
5.1.2 Deep Hybrid 2-D CNN-BLSTM Forecasting Model	75
5.2 Proposed Algorithm	76
5.2.1 Modeling PV-CAES Real-Time Energy Management Prob- lem as a Markov Decision Process	77
5.2.2 Deep Reinforcement Learning	78
5.3 Case Study and Numerical Results	80
5.3.1 Performance Evaluation of Solar Irradiance Forecasting Model	83
5.3.2 Effects of Weather Parameters in Solar Irradiance Fore- casting	86
5.3.3 CAES-PV Self-Scheduling Problem	87
5.3.4 Effects of Uncertainty Resources	89
5.4 Conclusion	90
6 A Novel Model-Free Deep Reinforcement Learning Frame- work for Energy Management of a PV-Integrated Energy Hub	91
6.1 Deep Reinforcement Learning (DRL) and Forecasting Framework	92
6.1.1 Deep Deterministic Policy Gradient (DDPG)	93
6.1.2 Deep Hybrid 2-D CNN-BLSTM Forecasting Model	95
6.2 Environment Model	96
6.2.1 CHP Units Modeling	96
6.2.2 Power-Only Units Modeling	98
6.2.3 Heat-Only Units Modeling	100
6.2.4 Fuel Cell Modeling	100
6.2.5 Power Balance	102
6.2.6 Objective Function	103

6.3 Case Study and Numerical Results	103
6.3.1 Implementing 2-D CNN-BLSTM Model for Solar Irra-	
diance Forecasting	106
6.3.2 PV-Integrated Energy Hub Scheduling Problem Based	
on 2-D CNN-BLSTM+DDPG Model	111
6.4 Conclusion	113
7 SFNAS-DDPG: A Biomass-based Energy Hub Dynamic Schedul-	
ing Approach via Connecting Supervised Federated Neural	
Architecture Search and Deep Deterministic Policy Gradient	115
7.1 Supervised Federated Neural Architecture Search And Hybrid	
2-D CNN-GRU Forecasting Model	117
7.1.1 NAS Agents As Base Learners	117
7.1.2 Hybrid Deep 2-D CNN-GRU Structure	119
7.2 Environment Model and Problem Formulation	119
7.2.1 Power-Only Units	119
7.2.2 Thermal Units	120
7.2.3 CHP Units	120
7.2.4 Biomass-based Boiler Units	121
7.2.5 Fuel Cell unit	122
7.2.6 Power Balance	124
7.2.7 Objective Function	125
7.3 Deep Deterministic Policy Gradient Algorithm	125
7.4 Numerical Study	128
7.4.1 Design Prediction Model With SFNAS Method	129
7.4.2 Biomass-based Energy Hub Dynamic Scheduling Prob-	
lem based the proposed SFNAS-DDPG	134
7.5 Conclusion	135
8 Conclusions and Future Work	138
8.1 Conclusions	138

8.2 Future Work	141
---------------------------	-----

Bibliography	143
---------------------	------------

List of Tables

3.1 Forecasting results of the proposed model (DWPT+BLSTM) with different training data size.	35
3.2 Comparison of forecasting performance for the NREL 1-hour dataset.	41
3.3 Comparison of forecasting performance for the NREL 10-minute dataset.	41
3.4 Comparison of forecasting performance for different input structures. (NREL 1-hour dataset)	44
3.5 MAE for different time steps. (NREL 1-hour dataset)	45
3.6 Comparison of forecasting performance for the Edmonton dataset.	46
4.1 Characteristics of NREL 5-MW Wind Turbine	57
4.2 Cross-Validation results of proposed model with some typical BLSTM structures for 1-step ahead power forecasting.	59
4.3 Forecasting performance comparison for 1-step and 2-step ahead tasks.	61
5.1 Cross-Validation results of the proposed solar irradiance forecasting model with some typical BLSTM-CNN structures.	83
5.2 Comparison of GHI Forecasting Results.	84
5.3 CAES-PV Scheduling Results For the Year 2019.	90
6.1 Comparison of GHI Forecasting Results.	110
6.2 Energy Hub Average Daily Operating Costs.	112
7.1 Hyperparameter bounds for SFNAS algorithm	131

7.2 Forecasting Task Results for the Best Architectures Found by SFNAS and Baseline NAS.	134
7.3 The Average Daily Operating Cost for the Proposed Multi- Carrier Energy System.	134

List of Figures

1.1 Organization of the thesis.	8
3.1 (a) DWT decomposition process. (b) DWPT decomposition procedure.	31
3.2 (a) General structure of a typical LSTM unit. (b) Sequential schematic of the LSTM blocks. (c) Structure of the bidirectional framework.	32
3.3 (a) Mutual information variation. (b) False nearest neighbors variation.	37
3.4 Forecasting result of the proposed model for the NREL 1-hour test data.	39
3.5 Forecasting result of the proposed model for the last week of NREL 1-hour test data.	40
3.6 Forecasting results for the last day of NREL 10-minute test data. (a) DWT+LSTM. (b) DWPT+LSTM. (c) DWT+MLSTM. (d) DWT+BLSTM. (e) DWPT+MLSTM. (f) DWPT+BLSTM.	43
3.7 Comparison of forecasting results for the last week of NREL 1-hour test data.	44
3.8 Forecasting results for the last week of Edmonton 1-hour test data. (a) DWT+LSTM. (b) DWPT+LSTM. (c) DWT+MLSTM. (d) DWT+BLSTM. (e) DWPT+MLSTM. (f) DWPT+BLSTM.	47
3.9 Comparison of multivariate and univariate forecasting results for the NREL 1-hour test data.	48

4.1	Different types of LiDAR-based on installation location.(a) Nacelle-mounted LiDAR. (b) Ground-based LiDAR	52
4.2	Overall Structure of 2-D CNN-BLSTM framework.	55
4.3	Different wind field components generated by TurbSim. (a) streamwise (longitudinal) component u . (b) transverse (cross-wise) component v . (c) vertical component w	58
4.4	Wind power forecasting comparison of four 2D-CNN-based models for the first 60 steps (600 sec) of test data. (a) 2D-CNN. (b) 2D-CNN-MLP. (c) 2D-CNN-LSTM. (d) 2D-CNN-BLSTM. . .	63
4.5	Comparison of power forecasting RMSE results for 1-step up to 6-step ahead tasks (step time = 10 sec).	64
4.6	Regression plots of the proposed method (2D-CNN-BLSTM): (a) Wind power (kW); (b) fatigue load (kN.m).	65
4.7	Fatigue load forecasting results comparison of proposed 2D-CNN-BLSTM and baseline model for the first 60 steps (600 sec) of test data. (a) baseline model. (b) proposed 2D-CNN-BLSTM model.	67
4.8	Wind power forecasting comparison of three Image-based models for the first 60 steps (600 sec) of test data in case of LiDAR failure. (a) 2D-CNN-MLP. (b) 2D-CNN-LSTM. (c) 2D-CNN-BLSTM.	68
4.9	Comparison of power and fatigue load forecasting results with different spatiotemporal models.	69
5.1	The schematic of proposed hybrid 2-D CNN-BLSTM solar irradiance forecasting model.	75
5.2	The overall diagram of the proposed DRL+2-D CNN-BLSTM for CAES-PV self-scheduling problem.	76
5.3	Comparison of forecasting results for a typical day with clear sky, partially cloudy, and cloudy conditions (i.e., 2019-05-27). .	85

5.4 Comparison of forecasting errors for different input vectors: a) RMSE, b) MAPE, c) MAE.	85
5.5 The comparison of self-scheduling results for a typical period 2019-06-01 to 2019-06-05 (a) PV and price profiles, (b) model-based step function [126], (c) model-based linear AA [24], (d) DRL, (e) DRL+2D-CNN-BLSTM.	88
6.1 Overview of the proposed 2-D CNN-BLSTM prediction framework.	96
6.2 CHP units' power-heat feasible region: a) Type 1, b) Type 2.	99
6.3 Power-only units' valve-point effects.	99
6.4 Dynamic performance curve of the FC unit.	102
6.5 Structure of the proposed PV-integrated energy hub.	104
6.6 The evolution of episodic operational costs associated with the proposed DDPG framework.	107
6.7 The overall architecture of the proposed DDPG+2-D CNN-BLSTM for PV-integrated energy hub scheduling problem.	107
6.8 Comparison of forecasting results for a typical day in summer with sunny and clear conditions (i.e., 2017-06-26).	110
6.9 Comparison of forecasting results for a typical day in winter with partly cloudy, and cloudy conditions (i.e., 2017-11-17).	111
7.1 Schematic diagram of the proposed SFNAS methodology.	117
7.2 Valve-point effects on the fuel cost of a power-only unit.	120
7.3 Nonlinear relationship between biogas production and temperature.	122
7.4 An illustration of the FC unit's dynamic performance curve.	124
7.5 The schematic of the proposed SFNAS-DDPG framework for the dynamic scheduling of biomass-based energy hub.	133
7.6 The evolution of weight (λ_i) for the gradient term in the momentum update.	135

7.7 The evolution of training and validation losses of the proposed	
CNN-LSTM/BLSTM/GRU models (a) baseline NAS-based LSTM,	
(b) SFNAS-based LSTM, (c) baseline NAS-based BLSTM, (d)	
SFNAS-based BLSTM, (e) baseline NAS-based GRU, and (f)	
SFNAS-based GRU	136

List of Acronyms

RE	Renewable energy
WPT	Wavelet packet transform
DWPT	discrete wavelet packet transform
LSTM	Long short-term memory
BLSTM	Bidirectional long short-term memory
LiDAR	Light detection and ranging
DRL	Deep reinforcement learning
CAES	compressed air energy storage
DDPG	Deep deterministic policy gradient
NAS	Neural architecture search
SFNAS	Supervised federated neural architecture search
CNN	Convolutional neural network
AESO	Alberta Electric System Operator
AI	Artificial intelligence
GPU	Graphics processing unit
MILP	mixed-integer linear programming
SP	Stochastic programming
RO	Robust optimization
CHP	Combined heat and power

DG	Distributed generation
FC	Fuel cell
DNN	Deep neural networks
ML	Machine learning
DL	Deep learning
RNN	Recurrent neural network
ESS	Energy storage system
PV	Photovoltaic
DQN	Deep Q network
SoC	State of charge
EV	Electric vehicles
GA	Genetic algorithm
FL	Federated learning
NREL	National Renewable Energy Laboratory
AMI	Average mutual information
SGD	Stochastic gradient descent
FAST	Fatigue, aerodynamics, structures, and turbulence
AFR	Air flow rate
HP	High pressure
GHI	Global horizontal irradiance
MDP	Markov decision process
ReLU	Rectifier linear units
FOR	Feasible operating region
GRU	Gated recurrent unit

Chapter 1

Introduction

1.1 Background

In recent decades, the research and development of renewable energies have gradually increased worldwide as an appealing solution to the high greenhouse gas emissions of fossil fuel-based energy resources, which raised worldwide concerns [108]. Compared to other renewable energy sources, wind and PV energy resources have attracted extensive attention due to their cleanliness and abundance. The total installed capacity of wind power in Canada has increased by an annual rate of 20% in the past few years, from 2,349MW in 2008 to 12,816MW in 2018 [25]. In particular, the government of Alberta, Canada, has set a firm target for the Alberta Electric System Operator (AESO) to move towards having 30% of Alberta's electricity coming from renewable energy sources (RESs) by the year 2030, with an estimated additional RESs integration of 5,000 MW to the grid. Accordingly, we can anticipate an increase in the contribution of wind and solar energy to our energy mix over the next several years. Although these RESs can be controlled to some extent, integrating them into the power system is a challenging task due to their variable and partially predictable nature. In the big data era, with the booming advancement of machine learning techniques as well as the development of graphics processing units (GPUs), deep learning-based methodologies as the new branch of artificial intelligence (AI) algorithms have been gradually developed and applied to many real-world applications [82]. Therefore, the

design and implementation of an accurate and comprehensive energy management framework can improve the operation of RES-based energy systems [30]. Moreover, wind- and PV-generated power forecasting plays a crucial role in energy management problems [124]. Therefore, it is considered an essential step in finding the most economical solution for the operation of power and energy systems with high RES penetration. Thus, investigating deep learning-based algorithms to address RES forecasting and, consequently, energy management problems is becoming an increasingly hot topic in the area of power and energy systems [49][62][73].

1.2 Research Motivations

The available literature on RES-based power and energy systems falls short in the following aspects:

1. The most significant challenge for the large-scale penetration of wind energy into power and energy systems is its uncertain and intermittent nature. The wind power generation mainly depends on the wind speed, which can dramatically fluctuate in few seconds and directly affect the stability, resilience, and robustness of the power system. For this reason, accurate wind speed prediction facilitates wind power facilities' integration into modern power systems. As of yet, there has been insufficient research on the application of deep learning techniques in the area of wind speed forecasting for improvement to be achieved from both the preprocessing and model aspects.
2. In the technical literature, wind turbine response forecasting is generally made using a wind speed time series measured at the hub height of the turbine, which ignores the chaotic and stochastic characteristics of wind turbulent flow over a rotor area. Thus, there is a pressing need to consider more extensive feature measurements of inflowing wind toward

the turbine, such as speed, direction, and turbulence.

3. In spite of being regarded as an advanced grid-scale storage technology, few studies have been conducted on the self-scheduling and energy trading of compressed air energy storage (CAES) facilities in the electricity markets. Aside from this, these works use piecewise linear characteristic curves and linearized thermodynamic constraints to formulate the scheduling problem in mixed-integer linear programming (MILP) form and solve it using conventional solvers. Ignoring the nonlinear thermodynamic constraints and practical limitations can prevent realistic analysis of the CAES technology; hence, making the results less robust.
4. To operate an energy hub in the most cost-effective way while dealing with operational constraints of interacted energy infrastructures, three main challenges have to be addressed. (i) Most studies related to energy hub systems adopt conventional optimization methods, such as stochastic programming (SP) or robust optimization (RO). Generally, these techniques require detailed and perfect knowledge of the system's parameters and operational model, resulting in high dependencies of decision-making in the accuracy of the employed system model and expert knowledge, which is very costly and challenging. (ii) Till now, in the energy hub operation area, most scheduling methods employ piecewise linearization modeling for the system units, such as combined heat and power (CHP), distributed generation (DG), and fuel cell (FC). However, this assumption creates some errors in the scheduling results and consequently, the obtained solution cannot be optimal for the practical operations of the energy hub. (iii) There is rarely any consideration of a comprehensive forecasting framework for the integration of renewables during the energy hub decision-making process, which could cause considerable challenges to the stability and security of the energy hub system.

- With biomass energy resources being widely distributed and its potential to support multiple forms of energy demands, such as electricity and thermal, the integrated operation of other RESs and biomass can offer a cost-effective alternative compared to utility grid operations. Literature has not yet addressed the physical characteristics and thermodynamic effects of temperature-sensitive biogas production at the operational stage. In the meantime, deep neural networks (DNN) models have made promising progress on several tasks, including prediction. However, their performance is still heavily influenced by the parameters and architecture of the neural network (the number of layers and the number of nodes, as well as the connectivity between layers). In most cases, it is challenging to evaluate how parameter settings influence the performance of the available models, even when they have a thorough understanding of both machine learning (ML) and deep learning (DL). Furthermore, recent studies in the field emphasize the use of higher-level models in order to obtain more accurate predictions, increasing the number of parameters included in the model. This has made exploring such large parameter spaces a more challenging undertaking. Neither expert knowledge nor empirical trial and error are always useful in this regard.

1.3 Research Objectives

Motivated by the significant role of RESs in future power and energy systems, this research aims to address the following points:

- Design a novel deep learning-based model integrating the discrete wavelet packet transform (DWPT) and bidirectional long short-term memory (BLSTM) to precisely capture deep temporal features and learn the time-varying relationship of wind speed time series.
- Propose a novel light detection and ranging (LiDAR)-assisted convolutional neural networks (CNN)-BLSTM model for the ultra-short-term

prediction of future wind turbine responses using upcoming sequences of full wind field components and hub-height wind speed time series.

3. Address the energy arbitrage problem of a CAES-PV facility by developing a model-free deep reinforcement learning (DRL) framework in the presence of a sky images-based short-term solar irradiance forecasting methodology.
4. Utilize the DDPG framework as a fully model-free and data-driven DRL method to develop an intelligent controller that can exploit information to optimally schedule the energy hub to minimize energy costs and emissions.
5. Develop a dynamic scheduling framework for a multi-source multi-product facility with a biomass-solar hybrid renewable system, taking into account the nonlinear characteristics of the biogas production facility, and propose a novel neural architecture search (NAS) technique to learn the architecture and model parameters of the DNNs.

1.4 Research Methodology

First, by applying the DWPT, both approximations and details parts are decomposed by passing through the filters to choose the frequency band related to the features of the original signal more adaptively. The BLSTM networks are incorporated to deal with the uncertainties more effectively as they have bidirectional memory capability (feedforward and feedback loops) to investigate both previous and future hidden layers data. To simultaneously improve the forecasting performance and decrease the learning complexity, the reconstructed state space of historical wind data is employed to reflect the evolution laws of wind speed. Second, the network is extended by combining the 2-D CNN and BLSTM for concurrently capturing high levels of abstractions in wind fields, thus forecasting wind output power and fatigue

load as two representatives of wind turbine responses. The LiDAR wind preview information is used as the 2-D-images of wind fields for the CNN. The proposed model employs 2D-CNN and BLSTM networks to better handle complex spatial-temporal features from the highly variable wind data compared to conventional forecasting methods, which simply use historical time series data. Third, by conducting comprehensive economic assessment studies, a DRL framework for a CAES-PV facility participating in the energy market is developed. Due to the nonconvex nature and highly intermittent parameters involved in the scheduling problem, the deep Q-network (DQN) agent is introduced to perform the optimal self-scheduling of the CAES-PV system incorporating the thermodynamic characteristics of the system. To address the uncertainties of electricity price and PV power output, especially during cloudy days, a novel hybrid 2D CNN-BLSTM model is adopted to predict the price and solar irradiance more accurately. Fourth, by upgrading the DRL agent of the third work, the optimal energy management problem of a PV integrated energy hub is assessed. A novel DDPG+2D-CNN-BLSTM approach as a fully model-free and data-driven DRL framework is proposed to provide an intelligent control strategy. The method can lead to a more efficient operation by considering nonlinear physical characteristics of the energy hub components like nonconvex feasible operating regions of combined heat and power (CHP) units, valve-point effects of power-only units, and fuel cell dynamic efficiency. Finally, by focusing on the ever-increasing role of biomass energy resources worldwide, the impact of several underlying factors on the cost-benefit analysis of a biomass-based energy hub is investigated using a entirely data-driven and model-free actor-critic DRL-based decision-making framework. The SFNAS approach is incorporated and employed to form a novel model-free and self-adaptable energy management algorithm for a RES-based multi-carrier energy supply infrastructure.

1.5 Research Contributions

The contributions of this thesis to the research field can be summarized as follows:

1. A hybrid deep learning-based model for wind speed forecasting based on DWPT and bidirectional LSTM network [25],
2. A deep spatial-temporal 2-D CNN-BLSTM model for ultra-short-term LiDAR-assisted wind turbine's power and fatigue load forecasting [26],
3. A deep reinforcement learning-based self-scheduling strategy for a CAES-PV system using accurate sky images-based forecasting [28],
4. A novel model-free deep reinforcement learning framework for energy management of a PV-integrated energy hub [27], and
5. An optimal model-free scheduling model incorporating a thermodynamic/economic analysis of a biogas-based energy hub.

1.6 Thesis Organization

This thesis is organized as shown in Figure 1.1. A brief literature survey related to deep learning-based forecasting and energy management algorithms for smart grid applications is presented in Chapter 2. Chapter 3 describes the wind speed forecasting approach based on DWPT and Bidirectional LSTM network. In Chapter 4, deep spatial-temporal 2-D CNN-BLSTM model for ultra-short-term LiDAR-assisted wind turbine's power and fatigue load forecasting is presented. Chapter 5 provides deep reinforcement learning-based self-scheduling strategy for a CAES-PV system using accurate sky images-based forecasting model. In Chapter 6, a fully model-free and data-driven DRL framework is proposed to develop an intelligent controller that can exploit information to optimally schedule the energy hub with the aim of minimizing

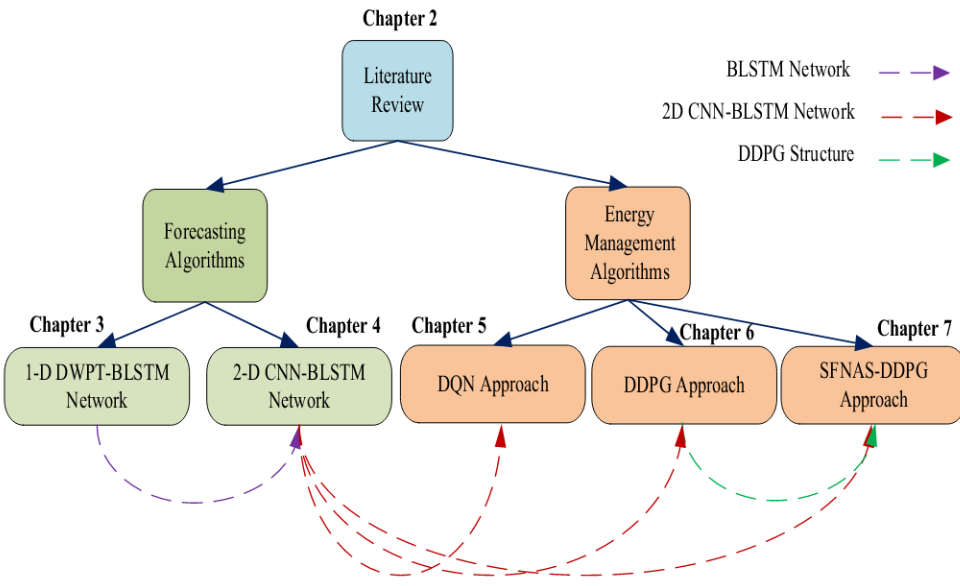


Figure 1.1: Organization of the thesis.

energy costs and emissions. In Chapter 7 the proposed SFNAS-DDPG framework as a dynamic scheduling framework for an energy hub with a biomass-solar hybrid renewable system is presented. Finally, Chapter 8 makes concluding remarks on the thesis and offers some potential directions for future research.

Chapter 2

Literature Survey

In this chapter, a brief review of previously proposed models and approaches in the areas of RE forecasting and smart grid energy management is provided.

2.1 Deep Learning-based Forecasting Approaches

In recent decades, the research and development of renewable energies have gradually increased worldwide as an appealing solution to the high greenhouse gas emissions of fossil fuel-based energy resources, which raised worldwide concerns [109]. Due to its cleanliness and abundance, wind energy has attracted extensive attention compared to others in the realm of renewable energy sources. The total installed capacity of wind power in Canada has increased from 2,349 MW in 2008 to 12,816 MW in 2018 at an annual rate of 20% within ten years [25]. In particular, the government of Alberta, Canada, has set a firm target for the AESO to move towards having 30% of Alberta's electricity coming from RESs by 2030, with an estimated additional RESs integration of 5,000 MW to the grid. It is anticipated that a significant portion of the 5,000 MW of renewable energy capacity will come from wind power [26]. Nonetheless, the most significant challenge for the large-scale penetration of wind energy in the power and energy systems is its uncertain and intermittent nature [31]. Wind power generation mainly depends on wind speed, which can dramatically fluctuate in a few seconds and directly affect the stability,

resilience, and robustness of the power system. For this reason, accurate wind speed prediction facilitates wind power facilities integration into modern power systems.

2.1.1 Wind Speed Time Series Prediction

Over the past few years, different wind speed time series prediction models have been developed in the literature [8, 74, 76, 77]. Based on the forecast time horizons, these models can be mainly classified into three categories [74]: 1) Short-term wind forecasting refers to the prediction of wind data in a period starting from several minutes to hours ahead. Economic dispatch, grid regulations, and real-time electricity market clearing depend on this type [77]. 2) Medium-term prediction is mainly for time horizons ranging from several hours to a week. This type of prediction benefits reserve markets and unit commitment [76]. 3) Long-term prediction is for a period starting from one week to years ahead. Long-term studies of wind power plants, such as maintenance issues or expansion planning, utilize this forecasting type [8].

Generally, wind speed and wind power prediction methodologies are divided into two groups: physical and statistical methods [130]. The physical forecasting methods use boundary conditions and physical parameters such as ambient temperature, atmospheric pressure, obstacles, and surface roughness [47]. These models often have excellent forecasting performance in the long-term period and large-scale areas due to the high computational burden. The computational fluid dynamics (CFD) and numerical weather prediction (NWP) are the most critical technologies in the physical models. The research work presented in [5] proposes a boundary layer scaling (BLS) technique based on the NWP model for long-term wind speed forecasting. The statistical forecasting models mainly use the wind time series data and try to find the mathematical relationships between the spatial-temporal samples or historical data, which yields accurate estimation results in the short-term prediction tasks. The Autoregressive (AR) model, autoregressive moving aver-

age (ARMA) model, and autoregressive integrated moving average (ARIMA) model are the most popular linear statistical approaches. In [20], an ARIMA model is introduced to represent the upper and lower bounds of wind power generation. However, the linear nature of these methods limits their ability to deal with challenging wind data prediction problems and handle nonlinear patterns. Recently, by developing artificial intelligence (AI) algorithms, different new methods for wind data forecasting have been quickly proposed. Compared with the linear statistical prediction methods, these models could provide a complicated nonlinear relationship for prediction tasks. An artificial neural network (ANN) is a promising AI tool for accurate time series forecasting [145]. Most ANN architectures introduced in the literature have only one single hidden layer and are shallow. For example, three types of typical shallow neural networks (SNNs), including adaptive linear element (ALE), backpropagation neural network (BPNN), and radial basis neural network (RBFNN) for one-hour-ahead wind speed prediction are employed and evaluated in [87]. It was observed that the performance is highly dependent on the hyperparameters of the networks, and none of the models can outperform others in terms of all criteria.

To compensate for the shortcomings of the above forward structures, recurrent neural networks (RNNs) have been proposed [130]. Unlike feedforward NNs, RNNs acquire the predicted value from the current inputs and the experience that leads to the better capturing of various patterns and temporal sequences. For example, to predict wind power time series, the authors of [130] use two RNN-based models: the nonlinear autoregressive with exogenous inputs (NARX) and Elman. Reference [97] presented a non-parametric probabilistic wind power forecasting method based on empirical dynamic modeling (EDM) and Takens' theorem. Difficulties in finding optimal structures in the search space of ANNs with several layers might be the main reason for using SNNs. However, SNNs are not capable of efficiently learning sophisticated features from the wind data; thus, they have the drawbacks of getting into

local minimum and over-fitting. Recently, with the booming advancement of machine learning techniques as well as the development of graphics processing units (GPUs), neural network-based deep-learning methodologies as the new branch of ANNs have been gradually developed [82]. In contrast to SNNs, such models can effectively extract inherent abstract features of the highly varying time series data. In [141], a novel deep belief network (DBN) model is employed for both deterministic and probabilistic wind speed forecasting. A combination of secondary decomposition (SD) and bidirectional gated recurrent unit (BiGRU) is presented in [156]. The presented model in [77] extracts unsupervised temporal features from wind speed data by restricted Boltzmann machines (RBM) and rough set theory. The long short-term memory (LSTM) architecture, which is a particular type of RNN with rich dynamics, was initially proposed by Hochreiter and Schmidhuber [55]. These networks overcome the vanishing gradient problem, causing losses of valuable information by introducing a gating mechanism and memory cells into RNNs [80]. Reference [6] evaluated the effect of performing deep-stacked LSTM and BLSTM in electricity load forecasting. Compared with abundant SNN forecasting research, only a few studies are related to deep learning-based forecasting for wind speed [129][151]. In [19], the authors proposed a two-layer structure based on extreme learning machine (ELM), Elman NN, and LSTM network to predict wind speed in 10-min and 1-hour ahead time intervals. As another example, in [63], a short-term wind speed forecasting model based on the combination of clustering and bidirectional LSTM (BLSTM) is proposed. All of these studies illustrated the effect of using deep networks on increasing prediction accuracy.

Besides, signal processing techniques can also considerably enhance the forecasting models' accuracy through data transformation, de-noising, and feature extraction. For example, a short-term wind speed prediction model based on wavelet packet transform (WPT) and SNN was proposed in [99]. In very recent literature, the authors of [155] combined improved empirical wavelet transform (IEWT) and least square support vector machine (LSSVM) to fore-

cast short-term wind speed. Although different signal processing methods have been widely used as a preprocessing approach in wind prediction models, minimal studies are made on integrating WPT and deep neural networks.

Another challenge in wind profile forecasting is the chaotic and stochastic characteristics of wind turbulent flow over a rotor area.

2.1.2 Wind Turbine's Power and Fatigue Load Forecasting

In the technical literature, wind turbine response forecasting is generally made using a wind speed time series measured at the hub height of the turbine. Nevertheless, the previously proposed approaches focus on the wind speed time series measured at the hub heights of the turbine, which ignore the chaotic and stochastic characteristics of wind turbulent flow over a rotor area [25]. Thus, there is a pressing need to consider more extensive feature measurements of inflowing wind towards the turbine, such as the speed, direction, and turbulence. Recently, as an advanced remote sensing wind measurement technology, light detection and ranging (LiDAR) has been proposed and attracted extensive attention to improve inaccurate and unstable measurements of nacelle vane [53]. Moreover, besides higher accuracy, other advantages of LiDAR over the conventional mechanical wind vanes and anemometers used in wind turbines are measuring diverse and longer distances and flexible installation. For example, in [165], the annual energy production increased by 1.83% through a LiDAR-based method for yaw error alignment. Results from [125] showed that LiDAR-aided wind speed measurement yielded fatigue or extreme load reduction on the wind turbine tower by 10%, thus improving the operation life of the wind turbine. Comprehensive analyses and discussions on the LiDAR-based wind turbine performance can be found in [23]. Although different efforts have been made to improve LiDAR-assisted control of wind turbines, minimal studies have been made on integrating such extensive wind field data and machine learning approaches to find wind turbine responses. In [105], a feedforward NN was employed for the extrapolation of the higher

heights wind speed using lower heights values.

It can be very beneficial to integrate accurate forecasting of renewable energy with deep reinforcement learning for energy management. As will be discussed next, this may have a wide range of applications.

2.2 Deep Reinforcement Learning-based Energy Management Algorithms

With the increasing global problems concerning energy security and climate change, new challenges in social progress and human survival have come to the fore. Requiring no fuel, and being renewable and non-polluting, RE resources, typically from PV and wind sources, have attracted extensive attention around the world. However, due to the uncertain and intermittent nature of these resources, it is generally very challenging for them to participate in energy markets and equally compete with conventional non-renewable energy producers. Consequently, to tackle these challenges, multi-carrier energy systems in the presence of energy storage systems (ESSs) are expected to play an influential role in improving the technical characteristics and economic sustainability of REs.

Three different energy systems will be investigated in this thesis. These systems witness serious energy management challenges, including renewable power forecasting and nonlinear system modeling.

2.2.1 Self-Scheduling Strategy for a CAES-PV System

There are different grid-scale ESSs at various levels of maturity. However, only pumped hydro energy storage (PHES) and compressed air energy storage (CAES) are technically and economically feasible alternatives for large-scale applications [22]. Environmental concerns and site constraints limit the further development of PHES. CAES is another promising bulk energy storage technology nowadays. It is advantageous in terms of fast response capability, large capacity, and long service time. It is free of geographical restriction,

and there are several available site options to host underground caverns for air storage, especially in North America with its abundant geological formations [37].

Despite being known as a developed grid-scale storage technology, not many works on self-scheduling and energy trading of CAES facilities in electricity markets are reported. An information gap decision theory (IGDT)-based self-scheduling formulation of CAES for participation in energy markets considering price forecasting errors is proposed in [127], while [71] suggests the application of CAES for the purpose of congestion relief in transmission systems as an ancillary service. In [110], a robust optimization approach is employed to investigate the optimal market participation of a merchant CAES in the presence of electricity market price uncertainty. Despite taking into consideration the presence of uncertainties in [71][110][127], the CAES thermodynamic characteristics are ignored.

The thermodynamic limitations may result in unprofitable and costly scheduling for the CAES facility, leading to overestimating the system's revenues. In [126], a self-scheduling model for a CAES facility's participation in electricity markets is proposed. The approach in [126] is extended by providing a look-ahead scheduling model in [72]. The authors conclude that the proposed approach provides optimal market participation decisions and enables achieving higher profits for a CAES system. Reference [24] assesses robust optimization (RO) and affine arithmetic (AA) models in self-scheduling of a CAES facility participating in electricity markets in the presence of the thermodynamic limitations of the facility. However, these works use the piecewise linear characteristic curves and linearized thermodynamic constraints to formulate the scheduling problem in mixed-integer linear programming (MILP) form solved by conventional solvers. Ignoring the nonlinear thermodynamic constraints and practical limitations can prevent realistic analysis of the CAES technology, hence, making the results less robust.

On the other hand, optimal scheduling and real-time balancing of modern

ESSs highly depend on the knowledge of different operation parameters, especially the production of REs. However, a few studies concentrate on pairing CAES with REs to reduce reliability concerns and obtain higher benefits. For instance, the authors of [59] propose a risk-constrained two-stage stochastic programming model for the self-scheduling problem of a CAES paired with a smart residential energy hub (SREH). The Monte Carlo simulation method is used to model the inaccuracies of electricity market prices, energy demands, and solar radiation. In [7], a RO model for self-scheduling of CAES paired with wind energy is presented. Both [7, 59] model the uncertainties of scheduling problems by probability density functions (pdfs), which despite being reliable, show non-linear behavior and need large amounts of scenarios for achieving high accuracy. Reference [46] provides a coordinated strategy for a hybrid power plant (HPP) consisting of a CAES aggregator and a wind power aggregator (WPA). The scheduling is formulated as a three-stage stochastic optimization problem to maximize the expected profit and mitigate wind power uncertainties. Nevertheless, RE-based CAES scheduling frameworks introduced in the literature do not contain a comprehensive forecasting framework for an accurate and stable prediction of REs.

Although the aforementioned approaches obtained acceptable results and achieved some success in the self-scheduling of CAES facilities, they may be unsuitable for real-time scenarios where the variations in the demand of CAES charging/discharging and the energy market situation are much more complex. In addition, these techniques are heavily dependent on expert knowledge; therefore, optimal scheduling for complex scenarios needs high calibration efforts frequently to tune and select the appropriate control parameters. Recent research indicates that model-free strategies that do not require any knowledge from the system model could achieve great success in complex decision-making problems [100]. This success makes up an attractive means for developing and implementing model-free techniques in many power and energy system applications, such as energy management and control of active

distribution systems [3, 17, 49, 94, 139]. Deep Reinforcement Learning (DRL) has been introduced in the literature by training deep neural networks (DNNs), as a universal function approximator, with reinforcement learning (RL) techniques [100]. Besides being model-free and self-adaptable, an advantage of the DRL model over model-based methods is the ability to learn a good control policy for a very complex environment from historical data. After the learning process of the controller, which is called the offline step, DRL can take the optimum actions with no expert tuning or external intervention. This feature provides a dynamic scheduling framework with superior robust performance.

2.2.2 Energy Management of a PV Integrated Energy Hub

Traditional independent operation of energy sectors cannot take advantage of the penetration of renewable energy resources and the synergies between multiple energy carriers. Co-ordinated operation of interacted energy systems is therefore required to boost an efficient transition to a cost-effective and low-carbon energy future. In this context, the energy hub has gained recognition for improving the reliability, resilience, and profitability of multi-carrier energy systems at the local level by redistributing supply and load across different energy divisions [111]. Energy hub offers innovative opportunities to enhance the energy system's flexibility for addressing renewable-based generation with the use of fast response cogeneration units (e.g., combined heat and power (CHP)). While being economical and environmentally friendly, renewable-based energy hubs could also cause considerable challenges to the economic and reliability of the energy system's operation due to both internal nonlinearities (e.g., CHP units) and external uncertainties (e.g., renewable energy). Thus, in this changing environment, accurate and stable scheduling of a renewable-based energy hub is a pressing issue for reshaping today's energy infrastructure toward a clean and sustainable energy system.

A large body of prior research on energy hub systems focuses on scheduling and operation [31, 173] or design and expansion planning areas [21, 32].

Reference [98] assesses a cooperative trading framework for the energy management problem of an energy hub. In [90], a monotone generalized nash game (MON-GNG) is proposed for the scheduling problem of a cluster of residential energy hubs. A robust chance-constrained framework for optimal decision-making of an energy hub is provided in [65], where diverse electrical, heating, and cooling demands and renewable power generation are taken into account. The intermittent nature of renewable energy generation poses a significant obstacle to the optimal day-ahead scheduling plans of an energy hub. Reference [169] develops a two-stage distributionally robust optimization technique in the presence of multimodal forecast errors for photovoltaic (PV) generation. The scheduling is formulated as a two-stage model to mitigate the cost in the first stage, and, as part of the second stage, a real-time dispatch is provided with forecasts of PV power output.

In the technical literature, significant efforts have been expended in developing model-based scheduling frameworks for optimal operation of multi-carrier energy systems, where optimal scheduling solutions for energy hub systems with a variety of generation units, demands, and storage devices are derived by solving operational cost minimization problems. In general, these optimization problems require highly depend on the knowledge of different operational parameters and models, and the optimal energy management schedule is developed using estimated exogenous parameters, such as the weather-dependent renewable generation, price patterns, and energy loads. As a consequence, the quality of the resulting scheduling policies is heavily subjected to the accuracy of the underlying system model. Nevertheless, it can be very challenging and costly to obtain an accurate model of the operational dynamics of the system. Although these optimization frameworks do not fully incorporate the inherent volatility associated with such parameters, robust optimization (RO) [159,169], information gap decision theory (IGDT) [31,60], and stochastic programming (SP) [65,102,112] methods have been developed to cope with these uncertainties. RO and IGDT model uncertainties as uncertainty sets,

whilst SP employs a set of possible scenarios.

While the aforementioned approaches obtained acceptable results and achieved some success in the scheduling of multi-carrier energy systems, they may not be suitable to efficiently manage multiple highly nonlinear units in a competitive energy market. These techniques are significantly dependent on expert knowledge; thus, optimal scheduling for complex scenarios needs high calibration efforts frequently to tune and select the appropriate control parameters. For example, RO has lower computational costs than SP; however, the resulting decision can be too conservative due to RO's inherent characteristic of hedging against the worst-case scenario of unknown parameters. Meanwhile, SP can suffer from a dramatic increase in optimization scale as the number of scenarios increases. This issue restricts the capability of SP framework to deal with multiple uncertain resources simultaneously. Moreover, these techniques usually use piecewise linear characteristic curves and linearized constraints to formulate the scheduling problem in a mixed-integer linear programming (MILP) form solved by conventional solvers. Ignoring the nonlinear constraints and practical limitations can prevent realistic analysis of the energy hub concept, making the results less robust and reliable.

In contrast, a recent study indicates that, when dealing with complex decision-making problems, model-free approaches which do not rely on any knowledge from the system model could achieve great success [100]. Deep Reinforcement Learning (DRL) has been developed as a model-free approach by applying reinforcement learning (RL) techniques to train deep neural networks (DNNs). DRL combines deep learning and RL to exploit more sophisticated control policies, which are more complex than those represented by shallow regression models or look-up tables. In the era of big data, by performing a successive interpretation of data, DRL can take advantage of the rising amount of data captured by numerous sensors to learn optimal decision-making solutions, thus, coping with the encapsulated uncertainties of data. Furthermore, besides being model-free and self-adaptable, DRL does not require any con-

straint sets of uncertainties or explicit modeling of probability distributions. These desirable properties provide an attractive means of developing and implementing DRL methods in various decision-making and control problems in energy systems, such as system control [34, 57], electric vehicles (EV) [148], and the emergency and voltage control of power system [35, 58].

Focusing on active energy system scheduling and control area, deep Q network (DQN) framework has been applied to various high-dimensional state and action spaces optimization environments, e.g., building energy management [104], industrial Internet of Things (IIoT) [143], battery energy storage system [14], and cyber uncertainties [36]. Although DQN, by employing a DNN for the Q-value function approximation, is considered a significant improvement compared to conventional Q-learning, it can suffer from poor performance when dealing with continuous action spaces. For instance, the authors of [18] discretize the charging/discharging power of Lithium-ion batteries into five levels, or the control action of the EV provides seven levels in [140]. Consequently, batteries or EVs are significantly less flexible in the scheduling problem due to the multi-dimensionality and continuity of energy management decisions. Thus, there is a pressing need for the adoption of continuous action spaces. The deep policy gradient (DPG) approach is first developed by using DNN to estimate the probability of taking action in a given state [104]. However, DPG generally has a high variance in its gradient estimates and low sampling efficiency, which causes slow convergence. In very recent literature, to overcome this shortcoming, a deep deterministic policy gradient (DDPG) framework has been developed and applied to a few power systems' decision-making problems, such as state of charge (SOC) control [123], volt-var control (VVC) in distribution networks [134], and electricity market participation [89]. An actor-critic architecture featured in DDPG offers the advantages of both Monte Carlo policy gradient and value-based methods. In DDPG, the learning of action space selection is carried out using fewer samples, resulting in fewer computational resources when compared to the Monte Carlo policy gra-

dient approach. On the other hand, compared with the value-based method, it can solve continuous action-based RL problems by learning stochastic policies. These features can provide a flexible scheduling framework with superior robust performance for the energy hub energy management problem. However, most DRL-based energy management studies focus only on one category, such as energy storage or EVs, ignoring the coordinated decision-making for diverse and complicated systems. It does not reflect operational reality.

2.2.3 Dynamic Scheduling of a Biogas-Based Energy Hub in the presence of neural architecture search (NAS)

Several recent representative studies have been reported on the optimization of energy hub systems from different perspectives, including optimal design and expansion planning [21,32], optimal power dispatch [31,173], energy trading scheme planning [27,29], voltage-frequency optimization [168], etc. The literature on integrating biomass energy resources into the energy hub concept is somewhat limited and scattered. Using climate-independent biomass energy, an energy hub can balance the stochastic output of weather-driven renewable RESs. In both [85], [160], the planning problem for a biomass-based energy facility was studied and formulated as a two-stage mixed-integer linear programming (MILP) model. While the authors in [85] focused on the optimal planning of solar and biogas energy for reducing the dependency of the energy hub system on battery storage systems in remote regions, the model proposed in [160] centered on the expansion planning of integrated electric power and biogas delivery networks. In terms of the scheduling and operation of biomass-based multi-carrier energy systems, the existing literature studies the use of biomass energy resources as a solution to the increasing demand for diversified and affordable energy services. In [147], a stochastic optimal operation strategy for an integrated solar and biomass system is proposed by considering the uncertainties in market prices and solar irradiation. Reference [173] assesses an optimal operation strategy for an energy hub with a

biogas-solar-wind hybrid renewable system. The approach in [173] is extended by providing a distributed stochastic scheduling framework for the coordinated operation of interconnected biogas-solar-wind systems in [157]. Both [69, 70] propose trading schemes for the biomass-concentrated solar system. Stochastic optimization and information gap decision theory (IGDT) approaches are leveraged to address uncertain factors.

Even though some advances were made, the aforementioned works also had three limitations. Firstly, they need to understand the dynamics of components. Developing a dynamic model that can accurately simulate components' behavior is challenging due to the many factors that influence it. Further, model-based approaches may differ in premises or performance in relation to particular components, so their generalizability may be limited. Secondly, algorithms require explicit knowledge of how uncertainty is represented (for example, RES production's probability distributions). Finally, a third limitation is the lack of support for an online control mechanism, particularly for large-scale solutions. Specifically, these methods need to perform the optimization by selecting the most optimal solution among a set of possible ones, regardless of the problem size.

Alternatively, the disadvantages described above can be overcome through the use of model-free learning-based techniques. Recently, some research has been conducted on applying reinforcement learning (RL) to the energy management problem of multi-carrier energy systems, such as Q-learning (QL) [78], QL-linear programming (LP) [45], and fuzzy QL [174]. The combination of RL and deep neural networks (DNN), as a powerful function approximator, has led to the development of deep reinforcement learning (DRL). Through multiple interpretations, DRL can leverage the growing data collected from a variety of sources, revealing optimum control policies and dealing with uncertainty related to the data. Additionally, DRL is a model-free, self-adaptive method that requires no explicit modeling of probability distributions or constraints on uncertainties. The application of deep Q network (DQN) concepts to en-

ergy systems' control and scheduling has been developed for different scenarios involving the optimization of state and action spaces in high dimensions, e.g., energy storage system [14], industrial Internet of Things (IIoT) [143], electric vehicles (EV) [148], cyber uncertainties [36], and building energy management [104]. Although DQN has been regarded as a considerable improvement over conventional QL in approximating Q-value functions, its performance is suboptimal if the action spaces of the environment are continuous. DQN offers considerable advantages over QL, but its performance can be suboptimal regarding continuous action spaces. There are, for example, only five and seven levels of discrete control actions for lithium-ion batteries and EVs in [18] and [140], respectively. The adoption of a continuous action space is therefore of the utmost importance. This being the case, the deep deterministic policy gradient (DDPG) methodology was introduced and implemented on a few decision-making tasks involved in scheduling and controlling microgrids, including electricity market participation [89], distribution networks [134], volt-var control (VVC), and state of charge (SoC) control [123]. Through using both actor and critic networks, it provides both the benefits of value-based and Monte Carlo policy gradient approaches. Comparatively to the Monte Carlo policy gradient, DDPG uses fewer samples to learn action space selection, resulting in lower computational demands. Furthermore, in contrast to the value-based technique, stochastic policies can be used to address RL problems that involve continuous actions.

In the meantime, DNN algorithms have made promising progress in several tasks, including prediction. However, their performance is still heavily influenced by the parameters and architecture of the neural network (the number of layers and the number of nodes, as well as the connectivity between layers). In most cases, it is challenging to evaluate how parameter settings influence the performance of the available models, even when they have a thorough understanding of both machine learning (ML) and deep learning (DL). Furthermore, recent studies in the field emphasize the use of higher-level models

in order to obtain more accurate predictions, increasing the number of parameters included in the model. This has made exploring such large parameter spaces a more challenging undertaking. Neither expert knowledge nor empirical trial and error are always helpful in this regard. A neural architecture search (NAS) method finds the optimal network architecture for a given situation by defining a search space, a search strategy, and a performance estimation strategy [39,150]. NAS-developed network structures are proven to be superior to those constructed by hand in a variety of fields.

Over the past few years, the field of NAS has become an active area of research and experienced remarkable success [39,96,120]. A Bayesian optimization-based NAS has been used to optimize the structure of DNNs. For example, a new kernel captures the relevant parameters in [135] and a joint optimization of the architecture and hyperparameters is performed using Bayesian optimization in [164]. Recent proposals have attempted to turn NAS problems into RL problems. The NAS problem is addressed using Q-learning in [9,172]. To improve the search procedure described in [9], [10] uses a predictor. With shared DNN parameters, [114] increases the speed of search procedures. By developing a differentiable representation of the NAS model, gradient-based NAS techniques seek to optimize the parameters of the NAS. The performance of other neural networks is predicted by a neural network in [12,13]. An approach aimed at reducing training time and memory consumption for NAS is described in [15]. A generalization problem in DARTS models [93] is addressed in [86] by breaking the problem into sub-problems. Recent years have seen significant interest in evolutionary computation approaches to optimize DNN parameters. DNNs are employed as genotypes and phenotypes in a mutation-only Genetic algorithm (GA) in [118,149]. By evolving the cascades of convolutional filters, a GA for classification is presented in [115]. It is noteworthy that evolutionary-based NAS approaches result in neural networks of superior performance, but moderate in size, as shown in [39,96,120]. Additionally, privacy concerns are becoming more prevalent, which has led to

a growing interest in machine learning approaches that preserve the privacy of users. As a machine learning paradigm, federated learning (FL) deals with concerns about data privacy, particularly when working with distributed and heterogeneous information [79]. Thus, FL combined with NAS is capable of effectively addressing privacy concerns associated with NAS.

Chapter 3

Deep Learning-Based Model for Wind Speed Forecasting Based on DWPT and Bidirectional LSTM Network

In this chapter, a novel deep learning-based model integrating DWPT and BLSTM is developed to precisely capture deep temporal features and learn the time-varying relationship of wind speed time series. First, by applying the DWPT, both approximations and details parts are decomposed by passing through the filters to choose the frequency band related to the features of the original signal more adaptively. Then, the BLSTM networks are incorporated to deal with the uncertainties more effectively as they have bidirectional memory capability (feedforward and feedback loops) to investigate both previous and future hidden layers' data. To simultaneously improve the forecasting performance and decrease the learning complexity, the reconstructed state space of historical wind data is employed to reflect the evolution laws of wind speed. Two case studies using real-world wind speed datasets gathered from the Flatirons campus (M2) of the National Renewable Energy Laboratory (NREL) located in Colorado, USA, and the weather station of Edmonton, Canada, are implemented to demonstrate the effectiveness and superiority of the proposed hybrid method compared to the shallow architectures and state-of-the-art deep learning models in the recent literature.

This Chapter is structured as follows. Section 3.1 motivates and explains the delay embedding methodology, the WPT approach, and the BLSTM network. Then, it describes how they are employed to develop the proposed wind prediction model. The details of real-world wind speed datasets, parameter settings, and the well-known error criteria for evaluating the forecasting method are introduced in Section 3.2. Section 3.3 conducts two 1-hour and 10-minute real-world wind speed datasets to demonstrate the efficiency and applicability of the proposed algorithm, and Section 3.4 draws the conclusion.

3.1 Methodology

In this Section, first, the notation and concept of Takens' embedding theorem are explained, which are used in this work as an effective tool to form the reconstructed state space. Then, the proposed DWPT-BLSTM framework is introduced to capture deep temporal features from the reconstructed wind speed time series.

3.1.1 Delay Embedding and Dynamic Reconstruction Theory

In a chaotic system, the initially unobservable dynamics of interest can be reconstructed by employing Takens' embedding and dynamic reconstruction theories [97]. According to Takens' theorem, a new state space can be constructed such that its evolution of observations is equivalent to that of the original one. Building a delay embedding comes down to defining two parameters: normalized embedding delay λ , which determines each delay vector's optimal autocorrelation value, and embedding dimension d , which means the size of the set of most recent observations.

In a dynamical system and discrete-time environment, the observable output y_t is described as follows:

$$y_t = f(x_t) \quad (3.1)$$

where $f(\cdot)$ and x_t represent the dynamics of the system and nonlinear scalar-valued function, respectively. Based on the delay embedding theorem, reconstructed dynamics with embedding dimension d and normalized embedding delay λ , $\{y_t^{rec}\}$, can be formulated as follows:

$$y_t^{rec} = [y_t, y_{t-\lambda}, \dots, y_{t-(d-1)\lambda}] \quad (3.2)$$

The normalized embedding delay λ is determined heuristically based on the average mutual information (AMI) method [42]. By this method, the first minimum of the mutual information between y_t and $y_{t-\lambda}$ is the optimal value of λ . Besides, the false nearest neighbors (FNN) technique is applied to find the proper value of embedding dimension d . Furthermore, the first minimum of the FNN determines the acceptable minimum value of d under changes in the embedding dimension from $d \rightarrow d + 1$, which satisfies the sufficient condition $d \geq 2D + 1$ (D represents the state space dimension of the unknown dynamics) [51]. Based on the discussion mentioned above, both evolutions $y_t^{rec} \rightarrow y_{t+1}^{rec}$ and $x_t \rightarrow x_{t+1}$ are similar.

Therefore, to handle the forecasting problem of time series $\{x_t\}$, it is better to forecast the time series $\{y_t^{rec}\}$. The following mapping can represent this:

$$y_{t+1}^{predicted} = F(y_t^{rec}) \quad (3.3)$$

where $y_{t+1}^{predicted}$ is the forecasted value of the time series $\{y_t\}$ for the next time-step. It is worth noting that with different F , equation (3.4) can be extended to a multi-step prediction form.

$$y_{t+\tau}^{predicted} = F'(y_t^{rec}) \quad (3.4)$$

Since the wind data time series shows chaotic behavior from a dynamic system point of view, the reconstructed state-space model is employed to transform it into a suitable form of machine learning methods.

3.1.2 Time-Series Decomposition

The wavelet transform (WT) represents an excellent tool to capture the wind speed dynamics and temporal patterns since wind speed has a time-varying

nature and spreading frequency spectrum. By using WT, an initial wind data signal is decomposed into a set of wavelets, which in turn represent a better behavior than the original wind data series.

Compared to other signal decomposition methods, wavelet analysis can better reveal temporal features of the wind speed sequential data, such as discontinuities in higher derivatives, breakdown points, self-similarity, and trends [162]. Additionally, signal de-noising or compressing without any remarkable degradation are the other essential features of the WT. The WT is categorized into two groups: continuous wavelet transform (CWT) and discrete wavelet transform (DWT) [42]. A CWT of the signal $f(t)$ is described as follows [138]:

$$\text{CWT}_f(\alpha, \beta) = \langle f(t), \psi_{\alpha, \beta}(t) \rangle = \int_{-\infty}^{+\infty} f(t) \psi_{\alpha, \beta}^*(t) dt \quad (3.5)$$

$$\Psi_{\alpha, \beta}(t) = \frac{1}{\sqrt{|\alpha|}} \psi\left(\frac{t - \beta}{\alpha}\right) \quad (3.6)$$

where $\psi(t)$ and Ψ denote the mother wavelet and set of wavelets, respectively. α as a scaling coefficient determines the spread of the wavelet, and β as a translation coefficient controls the central position. Compared to the Fourier transform (FT), which represents the signal as a combination of sines and cosines, by using the CWT, a set of wavelets is generated associated with a mother wavelet, ψ , and predefined values of the scale and translation coefficients respect to the original non-stationary signal [33]. However, the CWT method is not easily applicable to the desired tasks due to substantial redundant information and a very high computational burden. According to (3.5) and (3.6), CWT is continuously achieved by continuously scaling and translating the mother wavelet and shifting it over the signal to obtain the correlation between them. Furthermore, there is not any analytical solution for most cases, which leads to numerical calculation methods and, consequently, higher computational complexity. DWT, as a digital counterpart of CWT, is

introduced to address these issues. Therefore, instead of following the proposed procedure, the signal is analyzed at different resolutions with various frequency bands. This type of WT applies a binary system to subsample the CWT, decreasing the redundant information while retaining the principal characteristics. It dramatically improves efficiency and keeps accuracy just as same as the CWT [119]. The DWT is expressed as (3.7), where v and k denote integers. β_0 and α_0 are a fixed dilation steps and the translation factor, respectively. There are two different sets of functions in DWT, wavelet, and scaling functions, which are related to high-pass and low-pass filters, respectively, as presented in (3.8) and (3.9).

$$\psi_{v,k}(t) = \frac{1}{\sqrt{\alpha_0^v}} \psi\left(\frac{t-k\beta_0\alpha_0^v}{\alpha_0^v}\right) \quad (3.7)$$

$$\psi(2^v t) = \sum_{k=1}^K g_{v+1}(k) \varphi(2^{v+1}t - k) \quad (3.8)$$

$$\varphi(2^v t) = \sum_{k=1}^K h_{v+1}(k) \varphi(2^{v+1}t - k) \quad (3.9)$$

where $g(k)$ and $h(k)$ denote the wavelet and scaling filters, respectively. ψ and φ are the wavelet and scaling functions, respectively. Subsequently, a signal $f(t)$ is written as follows:

$$\begin{aligned} f(t) &= \sum_{k=1}^K \xi_{v-1}(k) \psi(2^{v-1}t - k) \\ &\quad + \sum_{k=1}^K \zeta_{v-1}(k) \varphi(2^{v-1}t - k) \end{aligned} \quad (3.10)$$

$\xi_{v-1}(k)$ and $\zeta_{v-1}(k)$ are the coefficients calculated using the inner products of wavelet and scaling functions with the signal as follows:

$$\xi_{v-1}(k) = \langle f(t), \psi_{v,k}(t) \rangle \quad (3.11)$$

$$\zeta_{v-1}(k) = \langle f(t), \varphi_{v,k}(t) \rangle \quad (3.12)$$

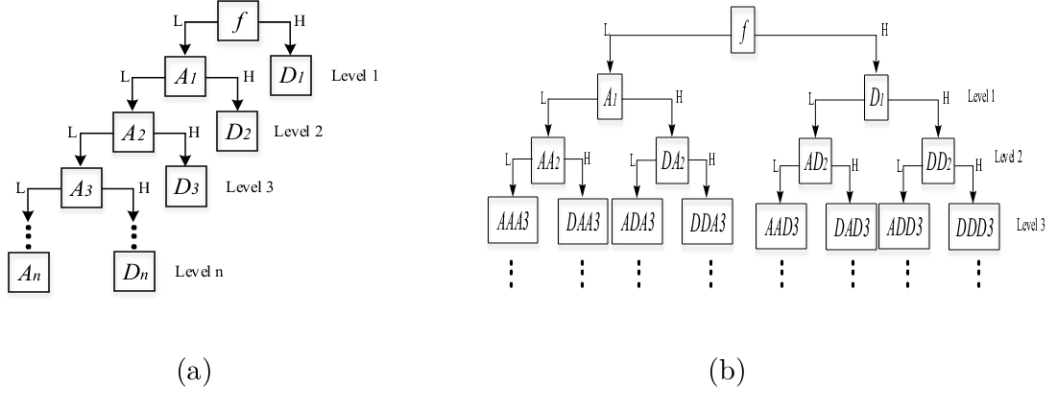


Figure 3.1: (a) DWT decomposition process. (b) DWPT decomposition procedure.

Based on the multiresolution approach developed by Mallat, a signal can be broken down into “approximations” associated with the general trend of the analyzed signal (A) and “details” related to the high-frequency parts (D) [50]. Then, approximations are consecutively decomposed into lower-resolution components to obtain a multilevel decomposition process. Figure 3.1(a) displays the analytical approach of the DWT method.

Nonetheless, the DWT can suffer from the curse of the frequency resolution problem as the resolution of WT decreases with the increasing signal frequency, given that details are not decomposed into shorter frequency intervals [162]. The discrete wavelet packet transform (DWPT) is a more accurate subdivision approach that can overcome the proposed defects of DWT. In the DWPT process, both approximations and details are decomposed by passing through the filters compared to the classic DWT that only uses approximations [170]. Furthermore, the frequency band related to the features of the original signal is selected more adaptively to reflect the necessary characteristics of the analyzed signal. As a result, DWPT shows more flexibility in both time/frequency and time/scale transformations by further decomposing of high-frequency elements. The decomposition procedure of a DWPT is described in Figure 3.1(b).

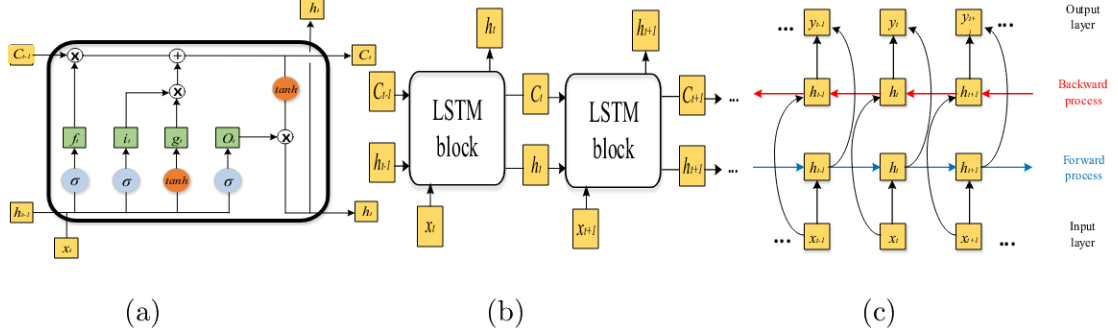


Figure 3.2: (a) General structure of a typical LSTM unit. (b) Sequential schematic of the LSTM blocks. (c) Structure of the bidirectional framework.

3.1.3 Bidirectional Long Short-Term Memory (BLSTM) Network

Along with the development of computer capabilities, data-driven techniques have gradually become the dominant tools to deal with time series forecasting tasks, especially in the case of stochastic and chaotic nonlinear time series [82]. Furthermore, RNNs, consisting mainly of sequence-based architectures to find the temporal correlations between past circumstances and the current information, have been widely applied in processing sequentially dependent data domains. RNNs try to establish a prediction framework for finding dependencies between inputs and outputs based on only a self-learning process instead of using a mathematical model.

Although RNNs have recently obtained more accurate forecasting results than conventional feedforward networks, these models have two main drawbacks: 1) RNNs have a weak ability to learn and address long-range dependencies due to the exploding or vanishing of gradient problem. Gradient exploding/vanishing refer to the situations that training back-propagated errors in the steepest descent algorithm increase/decrease exponentially fast to infinity/zero over time due to the multiple gradient calculations. This problem limits the capability of the network to learn temporal correlations when the time horizon is extended reliably. 2) RNNs do not consider the future context's information, which requires more backward relations modeling [138].

LSTM architecture is employed here as an alternative network to tackle them efficiently. The first issue is that LSTM networks are more complex and improved RNNs with an internal state capable of propagating data through multiple time steps and temporal processing characteristics of time series data. Let $l \in [1, L]$ be the layer of LSTM, which contains cyclically connected special blocks known as memory blocks. Figure 3.2(a) illustrates the general structure of the LSTM block architecture, where each block has one or more memory cells, and three multiplicative units called an input, an output, and forget gates, representing operators for respectively continuous writing, reading, and resetting of data in the cell. Also, Figure 3.2(b) shows the information connection procedure during the subsequent time steps in an un-rolled LSTM network. The past state or the explanatory variables are the candidates of the new information memorized by the input gate. The output gate controls the impact of memory content on the node output, whereas the forget gate can discard irrelevant information. Succinctly, the forward pass associated with the LSTM architecture is formulated as follows [80]:

$$f_t = \sigma(W_x^f x_t + W_h^f h_{t-1} + b^f) \quad (3.13)$$

$$i_t = \sigma(W_x^i x_t + W_h^i h_{t-1} + b^i) \quad (3.14)$$

$$g_t = \tanh(W_x^g x_t + W_h^g h_{t-1} + b^g) \quad (3.15)$$

$$o_t = \sigma(W_x^o x_t + W_h^o h_{t-1} + b^o) \quad (3.16)$$

$$C_t = g_t \odot i_t + C_{t-1} \odot f_t \quad (3.17)$$

$$h_t = \tanh(C_t) \odot o_t \quad (3.18)$$

where σ and \tanh represent the logistic sigmoid and the hyperbolic tangent activation functions, respectively, whereas f, i, o are the activation vectors related to the forget, input, and output gates, respectively. The weight matrices W and bias vector b to be optimized during the training procedure.

To solve the second problem of RNNs, the bidirectional concept is incorporated into the proposed LSTM model to capture the whole temporal horizon's information. Based on Figure 3.2(c), a structure including two different recurrent networks with the same output is capable of both forward and backward training processes [121]. The proposed topology has been widely applied in the speech recognition domain due to its capability to efficiently recognize a word by using not only the previous words but also the whole sentence [166]. Motivated by the proposed principle, here, the necessary information is completely exploited by the explanatory variables during each time step. This process leads to better prediction performance. Moreover, besides better training time, an advantage of the proposed bidirectional networks over unidirectional RNNs is robustness to the biased inputs and model uncertainties [138].

Bidirectional LSTM (BLSTM) models, as a combination of LSTM networks and bidirectional RNNs, can simultaneously memorize long-term dependencies and process the information bidirectionally. More specifically, when deep structures are built, one can achieve much higher data representation capability compared to traditional RNNs or LSTMs.

3.2 Realistic Wind Speed Forecasting Case Study Definition

In this Section, the details of real-world wind speed datasets, parameter settings, and the well-known error criteria for evaluating the forecasting method are introduced.

3.2.1 Datasets

The historical wind speed time series used in this work are measured from two different sites: 1) the Flatirons campus (M2) wind site of the National Renewable Energy Laboratory (NREL) located in Colorado, USA, obtainable from the NREL National Wind Technology Center (NWTC) website [61]. The data were obtained by applying a next-generation mesoscale NWP system called

Table 3.1: Forecasting results of the proposed model (DWPT+BLSTM) with different training data size.

Dataset	Range (%)	MAPE (%)	Training time
NREL 1-hour	1 Jan 2017 to 31 Dec 2018	6.16	00:09:11
NREL 1-hour	1 Jan 2016 to 31 Dec 2018	6.04	00:16:48
NREL 10-min	1 Jan 2000 to 31 Mar 2000	3.29	00:08:11
NREL 10-min	1 Oct 1999 to 31 Mar 2000	3.24	00:17:05

Weather Research and Forecasting (WRF), developed for operational forecasting needs and atmospheric research tasks. 2) Edmonton, Canada historical wind speed data [25]. The historical weather data are courtesy of Environment and Climate Change Canada and combined from multiple Environment and Climate Change Canada data sources to be accurate.

The chosen NREL datasets include wind speed data in 1-hour and 10-minute intervals from 1 January 2017 to 31 December 2018 and 1 January 2000 to 31 March 2000, respectively. The time period of the Edmonton dataset is from 1 January 2017 to 31 December 2018 with the hour unit. Table 3.1 shows the impacts of choosing bigger datasets on forecasting accuracy and computational time. As seen from this Table, using bigger training datasets increases the time up to double while having a negligible impact on the learning capability. Whole datasets are further split into three subsets for different purposes, namely the training set for building up the model, the validation set for an unbiased assessment during tuning the parameters of the model, and the testing set for the last evaluation of the model built. In this study, the training and validation sets account for 70% and 20% of the dataset, respectively, and the remaining data are allocated for testing the forecasting performance of the proposed method. In other words, the data partitioning is 0.7/0.2/0.1.

3.2.2 Parameter Details

It is worth noting that based on the state space reconstruction methodology, the input size of the network is determined by the dimension of delay vectors. From a dynamic systems point of view, the prediction task is considered the prediction of system states since a series of observations about the system is seen as a time series. In other words, the observations in the time series are a nonlinear projection of the system's state variables onto the observation variables. To this end, a small set of the most recent previous observations is used as state variables to construct an equivalent version of the original state space [97]. In this way, two parameters of the space need to be calculated: embedding delay λ , which optimally determines the level of autocorrelation corresponding to each delay vector, and embedding dimension d , which are mathematically equivalent to the size of the proposed observations' set. The utility functions of the TISEAN toolbox called *mutual*, and *false_nearest* are employed in this work to find the proper values of λ and d , respectively. Figs. 3.3(a) and 3.3(b) show the variations of the average mutual information and the percentage of false nearest neighbors, respectively. As shown in Figure 3.3(a), the average mutual information between wind speed at times t and $t - \lambda$ reaches its first local minimum at 18, which is chosen as the optimal value of λ . Moreover, as depicted in Figure 3.3(b) and based on the first minimum of the false nearest neighbors percentage, seven can be selected as the minimum acceptable value of d . Note that this value is not in contrast to the seasonality of time series data. λ means that the value time series at time t and at a time $t - \lambda$ can participate in the reconstructed space as two consecutive members due to the essential independence. On the other hand, the independence level is not so much as to say there is not any correlation between them. It is noteworthy that choosing two seasonal data points may lead to high redundant information, which is not desirable. Furthermore, wind speed data at time $t - 1$ to $t - 6$ (based on mutual information) are also added to the input vector to highlight the correlation of time series.

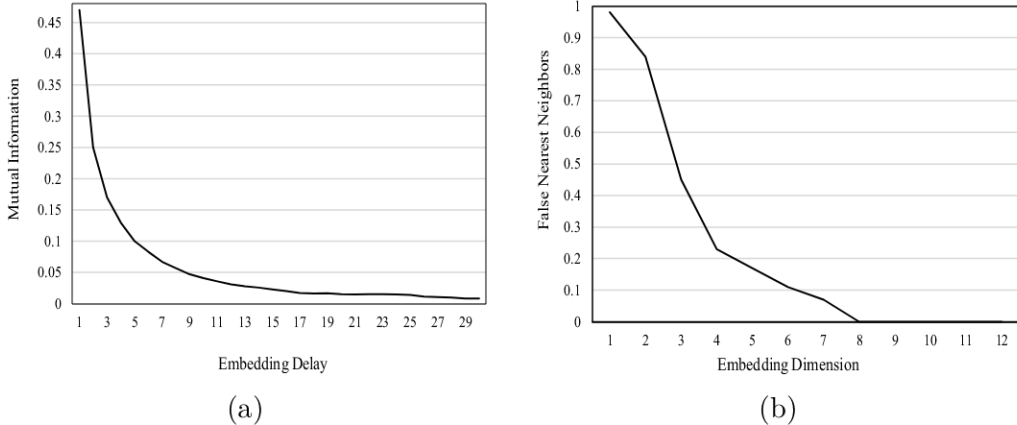


Figure 3.3: (a) Mutual information variation. (b) False nearest neighbors variation.

The proposed hybrid forecasting framework starts with determining the optimal values of embedding delay λ and dimension d parameters for the given datasets. To reduce the sensitivity of the BLSTM network to the data scale and accelerate the training procedure, the input vectors are normalized and scaled to the range of $(0, 1)$ according to their nature. It is assumed that there is no false or missing data because of the normal performance of measuring instruments during this time period. Then, db4 three-level DWPT as a comprehensive signal decomposition method is adopted. As there is no global theory or clear method to determine hyper-parameters associated with the BLSTM network, and they are completely data-dependent. Therefore, a random search method is applied on set $\psi = \{10, 20, \dots, 200\}$ to configure the proposed deep BLSTM network optimally. Although better-optimized configurations could be obtained by using heuristic algorithms or grid search methods compared to the proposed random search, these search algorithms have a very high computational burden and remarkable running time. The proposed BLSTM network is initialized with 100 units, three hidden layers, 50 epochs, and a batch size of 20. Besides, the simulation of each model runs 30 times to alleviate the randomness influence and avoid a suboptimal solution. Adaptive Moment Estimation (Adam), as a computationally efficient optimizer, is applied to optimally calculate the weights and biases of

the network and minimize the loss function. Adam is an adaptive learning rate optimization method that shows slightly better performance in practical applications compared to other popular optimization algorithms such as RMSProp, stochastic gradient descent (SGD), Adadelta, and Adagrad. In this study, all the experiments are implemented in MATLAB 2019 software. The workstation used is configured with an Intel Core TM i7-8700 3.2 GHz CPU and 32 GB of RAM.

3.2.3 Evaluation Criteria

The root means square error (RMSE), mean absolute error (MAE), and mean absolute percentage error (MAPE) are employed as three evaluation metrics to evaluate the prediction results as follows:

$$RMSE = \sqrt{\frac{1}{N} \sum_{i=1}^N (d(i) - y(i))^2} \quad (3.19)$$

$$MAE = \frac{1}{N} \sum_{i=1}^N |d(i) - y(i)| \quad (3.20)$$

$$MAPE = \frac{1}{N} \sum_{i=1}^N \left| \frac{d(i) - y(i)}{d(i)} \right| \times 100\% \quad (3.21)$$

where $d(i)$, $y(i)$ and N represents the desired output, the actual output, and the number of samples, respectively.

3.3 Experimental Results and Discussion

In this Section, two practical case studies of wind speed prediction in Colorado, USA, and Edmonton, Canada, are carried out. The simulation results and comparison with benchmark methods are presented to validate the performance of the proposed model.

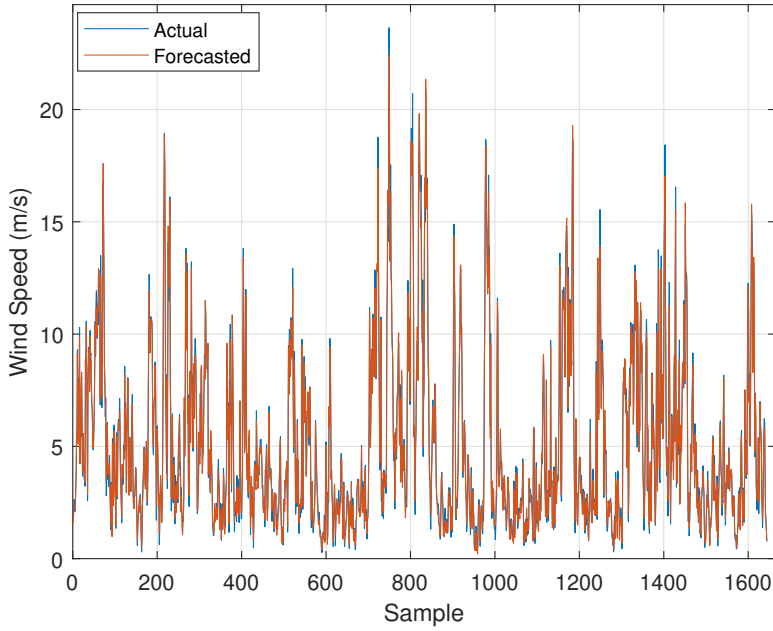


Figure 3.4: Forecasting result of the proposed model for the NREL 1-hour test data.

3.3.1 NREL M2 Wind Speed Dataset

After tuning the parameters and specifying the optimal structure, the model is trained by using the training set. The average time required to train the network is entirely dependent on the structure complexity, and for the proposed model, it is about 10 minutes, which makes it applicable for real-time wind speed forecasting purposes. In the testing step, only the feed-forward process is used to find the output of the network; thus, it has negligible time complexity and is, therefore so faster. Figure 3.4 shows the forecasting results of the proposed model over the test data. In order to provide better visualization, the results for the last week are also shown in Figure 3.5. As can be seen, the forecasted results (the orange line) follow the trend of the real measurements (the blue line) and are very close to them, which implies that the dynamic characteristics of the wind speed data are effectively captured by the model. Tables 3.2 and 3.3 compare the results of the proposed hybrid method

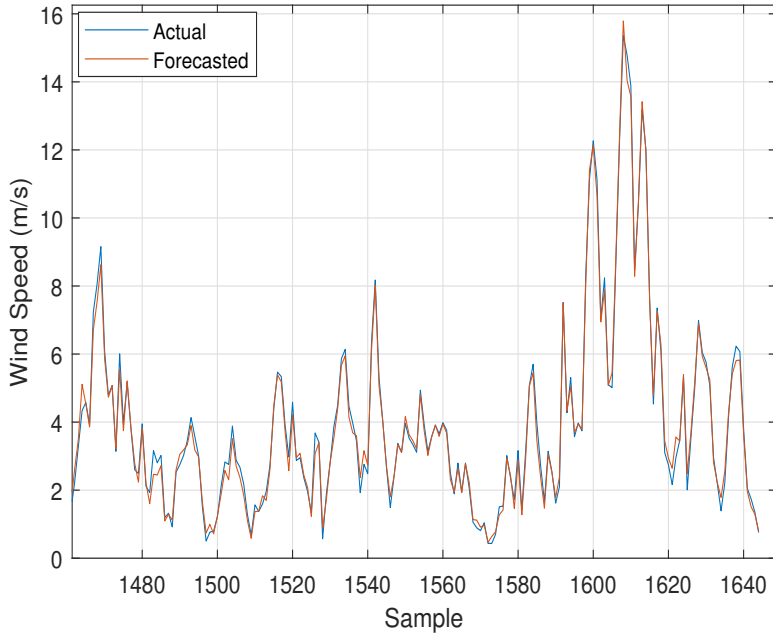


Figure 3.5: Forecasting result of the proposed model for the last week of NREL 1-hour test data.

with some benchmark models recently employed in the literature, including different combinations of DWT and DWPT with BPNN, RNN, DBN, LSTM, MLSTM, and BLSTM for 1-hour and 10-minute, respectively. The procedure of designing an optimal structure for the other models is similar to that of the proposed hybrid model. The optimal number of layers and hidden nodes are determined to be 3 and 30 for the BPNN and RNN, respectively. The DBN network has three hidden layers with 30 hidden nodes in each layer. The structures of the typical LSTM and MLSTM models are considered to be the same as the BLSTM network to provide a better comparison. According to the results, the RNN network outperforms BPNN due to its dynamic behavior. The DBN has generally higher forecasting accuracy compared to shallow architectures, i.e., BPNN and RNN. It has 9.15% and 8.74% MAPE improvements for the RMSE and MAPE over RNN in the 1-hour case. LSTM-based models, LSTM, MLSTM, and BLSTM, show promising prediction results by achieving significantly lower error metrics compared to BPNN RNN, and DBN.

Table 3.2: Comparison of forecasting performance for the NREL 1-hour dataset.

Forecasting method		RMSE (m/s)	MAE (m/s)	MAPE (%)	Training time
DWT+BPNN [145]		0.684	0.472	16.23	00:02:05
DWPT+ BPNN		0.513	0.363	10.60	00:03:11
DWT+RNN [130]		0.541	0.392	13.87	00:04:16
DWPT+ RNN		0.415	0.305	8.92	00:05:13
DWT+DBN [141]		0.539	0.387	13.34	00:04:18
DWPT+DBN		0.377	0.266	8.14	00:05:22
DWT+LSTM [151]		0.534	0.384	12.09	00:04:45
DWPT+LSTM		0.351	0.253	7.35	00:05:03
DWT+MLSTM [158]		0.501	0.354	10.08	00:10:37
DWPT+MLSTM		0.348	0.251	7.07	00:11:50
DWT+BLSTM [63]		0.507	0.365	10.21	00:07:26
Proposed (DWPT+BLSTM)	0.339	0.249	6.16	00:09:11	

Table 3.3: Comparison of forecasting performance for the NREL 10-minute dataset.

Forecasting method		RMSE (m/s)	MAE (m/s)	MAPE (%)	Training time
DWT+BPNN [145]		0.455	0.281	9.74	00:01:58
DWPT+ BPNN		0.311	0.199	5.83	00:02:58
DWT+RNN [130]		0.439	0.277	9.31	00:02:39
DWPT+ RNN		0.297	0.194	5.07	00:03:15
DWT+DBN [141]		0.392	0.275	8.34	00:02:57
DWPT+DBN		0.283	0.186	4.52	00:04:03
DWT+LSTM [151]		0.354	0.267	7.66	00:04:11
DWPT+LSTM		0.267	0.177	4.40	00:04:45
DWT+MLSTM [158]		0.244	0.159	3.91	00:09:07
DWPT+MLSTM		0.164	0.106	3.77	00:10:24
DWT+BLSTM [63]		0.247	0.165	4.16	00:06:55
Proposed (DWPT+BLSTM)	0.157	0.093	3.29	00:08:11	

As shown in Tables 3.2 and 3.3, the proposed method achieves the lowest RMSE, MAPE, and MAE values and procures the best prediction performance compared to the other benchmark models. It can also be observed that models with DWPT have better performance than those with DWT. For example, DWPT+ BPNN improves RMSE and MAE by 31% and 29%, respectively, compared to DWT+ BPNN. These improvements result from the fact that applying the DWPT transformation yields more detail and approximation coefficients and, consequently, better forecasting.

Moreover, using BLSTM leads to considerable improvement, especially in the 10-minute case, compared to LSTM. BLSTM provides advantages mainly by reducing the forecast errors while increasing the training time and complexity of the model. Note that the training time for the models with BLSTM is still much less than the prediction time scale of one hour. To better show how different models predict the highly volatile wind speed time series, the forecasting results of different networks for the 10-minute and 1-hour datasets are visualized in Figure 3.6 and Figure 3.7, respectively. As shown, the performance of the proposed hybrid model is much better than other shallow or deep learning-based models, especially when wind speed time series has an abrupt change due to using more meaningful information and better generalization capability.

To verify the performance of the reconstructed state-space model, the 1-hour case study is repeated for different input structures. Table 3.4 shows the results of some typical input structures for different values of d and λ . As shown in this table, both the increase and the decrease in the input vector parameters reduce the performance according to the forecasting indices.

On the other hand, Table 3.5 shows the MAE of different models for 1-hour up to 3-hour ahead wind speed prediction task. The proposed architecture, DWPT+BLSTM, procures remarkably better results than other deep and shallow architectures for larger prediction time steps. DWPT+BLSTM improves MAE by 6.7% and 3% for 2-hour ahead prediction compared to

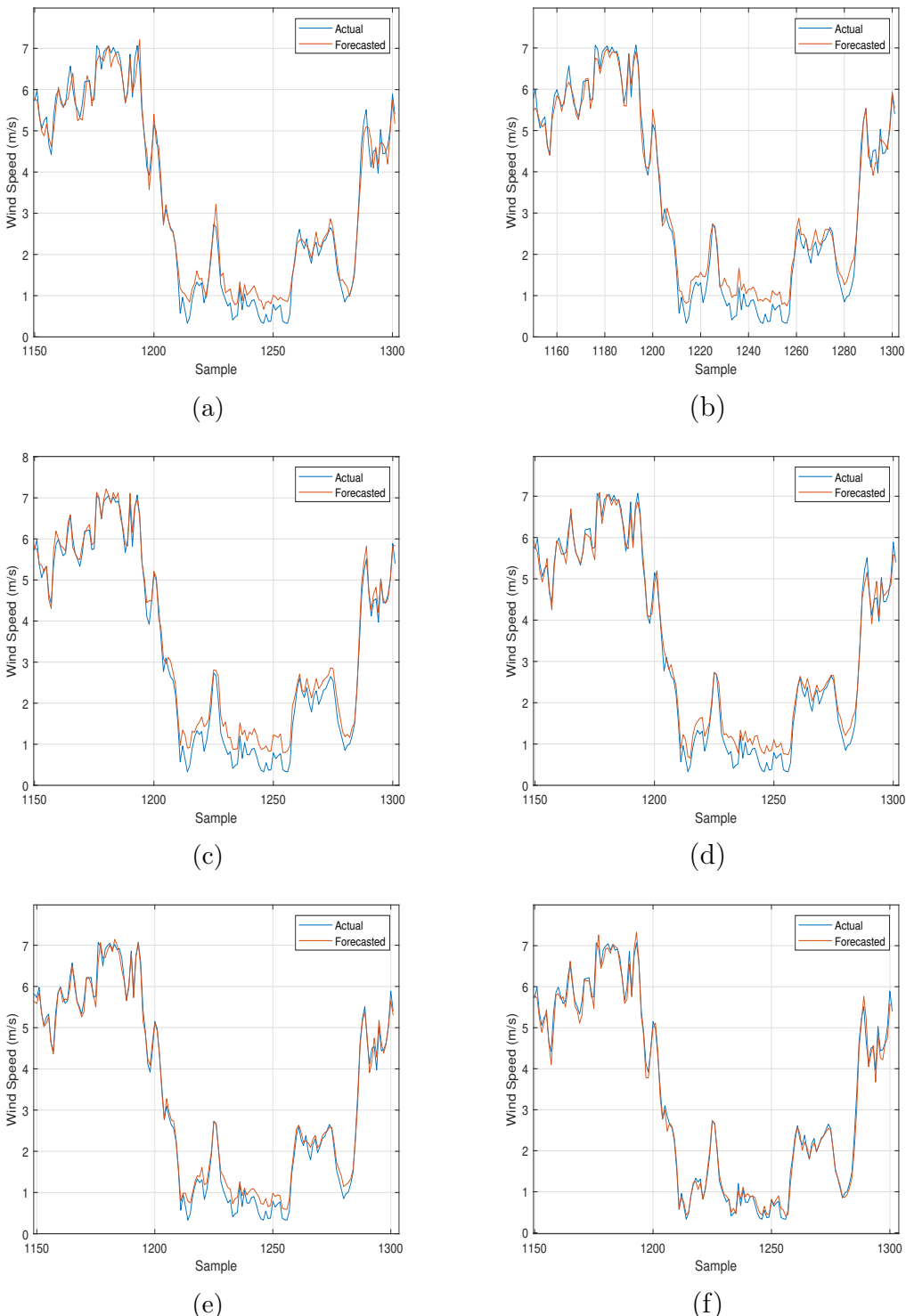


Figure 3.6: Forecasting results for the last day of NREL 10-minute test data. (a) DWT+LSTM. (b) DWPT+LSTM. (c) DWT+MLSTM. (d) DWT+BLSTM. (e) DWPT+MLSTM. (f) DWPT+BLSTM.

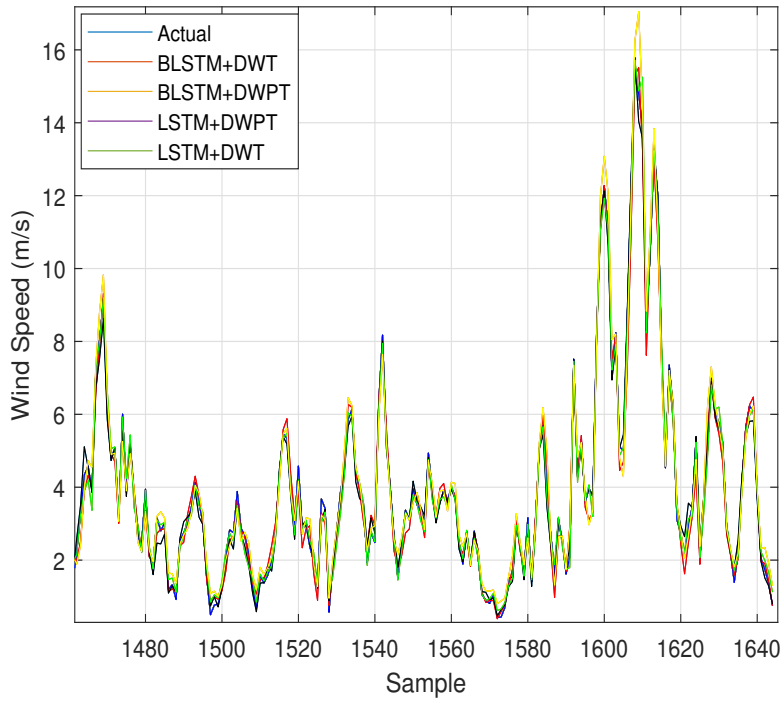


Figure 3.7: Comparison of forecasting results for the last week of NREL 1-hour test data.

Table 3.4: Comparison of forecasting performance for different input structures. (NREL 1-hour dataset)

Input vector structure (d, λ)	RMSE (m/s)	MAE (m/s)	MAPE (%)
(3, 14)	0.512	0.456	12.84
(5, 16)	0.384	0.274	8.95
(7, 18)	0.339	0.249	6.16
(9, 20)	0.367	0.267	6.35
(11, 22)	0.486	0.397	10.08

Table 3.5: MAE for different time steps. (NREL 1-hour dataset)

Forecasting	1-hour	2-hour	3-hour
DWT+BPNN [146]	0.472	0.691	1.162
DWPT+ BPNN	0.363	0.438	0.642
DWT+RNN [131]	0.392	0.513	0.778
DWPT+ RNN	0.305	0.357	0.511
DWT+DBN [142]	0.387	0.510	0.756
DWPT+DBN	0.266	0.341	0.494
DWT+LSTM [152]	0.384	0.506	0.748
DWPT+LSTM	0.253	0.332	0.487
DWT+MLSTM [81]	0.354	0.499	0.715
DWPT+MLSTM	0.251	0.328	0.473
DWT+BLSTM [64]	0.365	0.492	0.711
Proposed (DWPT+BLSTM)	0.249	0.318	0.441

DWPT+DBN and DWPT+MLSTM, respectively. Such improvement increases to about 10.7% and 6.8% for 3-hour ahead prediction. This shows the deep feature extraction ability of the proposed deep network. It is worth noting that, although the training time increases as the time horizon is extended, it is still negligible compared to the forecasting time step.

3.3.2 Edmonton Wind Speed Dataset

In this study, historical hourly wind speed data from Edmonton, Canada is used as the second dataset to show the applicability and effectiveness of the proposed model in dealing with different locations which have various wind speed characteristics. To perform a fair comparison, the time period is considered to be from 1 January 2017 to 31 December 2018. Similar prediction comparison results are obtained for Edmonton dataset, as shown in Table 3.6. The proposed DWPT+BLSTM model can still forecast future wind speed with the highest accuracy, which demonstrates the consistency and stability of the method. It is still the best forecasting model according to the error metrics

Table 3.6: Comparison of forecasting performance for the Edmonton dataset.

Forecasting method		RMSE (m/s)	MAE (m/s)	MAPE (%)	Training time
DWT+BPNN [146]		0.758	0.602	15.79	00:02:36
DWPT+ BPNN		0.507	0.383	8.97	00:03:04
DWT+RNN [131]		0.615	0.481	12.22	00:03:19
DWPT+ RNN		0.439	0.338	8.27	00:04:22
DWT+DBN [142]		0.582	0.449	11.61	00:03:27
DWPT+DBN		0.385	0.273	7.88	00:04:41
DWT+LSTM [152]		0.577	0.437	10.19	00:03:05
DWPT+LSTM		0.296	0.231	6.51	00:04:11
DWT+MLSTM [81]		0.526	0.392	9.21	00:09:02
DWPT+MLSTM		0.277	0.221	6.44	00:09:56
DWT+BLSTM [64]		0.490	0.371	8.64	00:06:41
Proposed (DWPT+BLSTM)	0.253	0.197	4.82	00:07:24	

value followed by the DWPT+MLSTM method. Furthermore, forecasting performance of different models with their corresponding errors for the last week of the Edmonton test data are shown in Figure 3.8. From this figure, it can be seen that the errors of DWPT-based models range from -1 to 1 m/s while for those with DWT can even approach to 5 m/s. Both DWPT+MLSTM and DWPT+BLSTM models have high potential to forecast the overall behavior of the wind speed time-series and they can follow the sharp spikes accurately. However, DWPT+MLSTM needs around 22% more training time compared to DWPT+BLSTM, while DWPT+BLSTM has 33.6% less MAPE. In summary, as the forecasting results illustrate, we can find that the proposed DWPT+BLSTM framework can predict Edmonton hourly wind data effectively better than the benchmark methods.

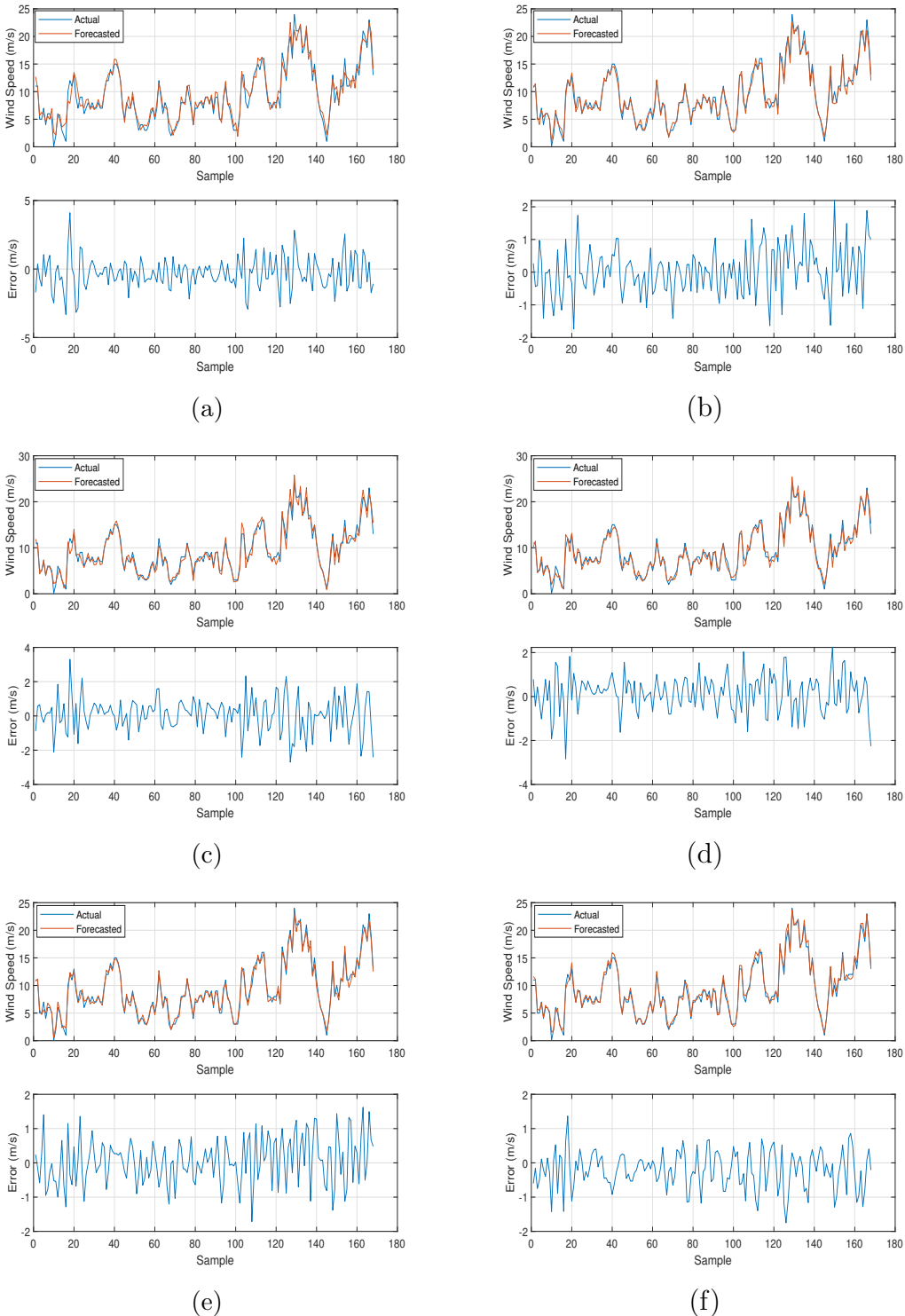


Figure 3.8: Forecasting results for the last week of Edmonton 1-hour test data. (a) DWT+LSTM. (b) DWPT+LSTM. (c) DWT+MLSTM. (d) DWT+BLSTM. (e) DWPT+MLSTM. (f) DWPT+BLSTM.

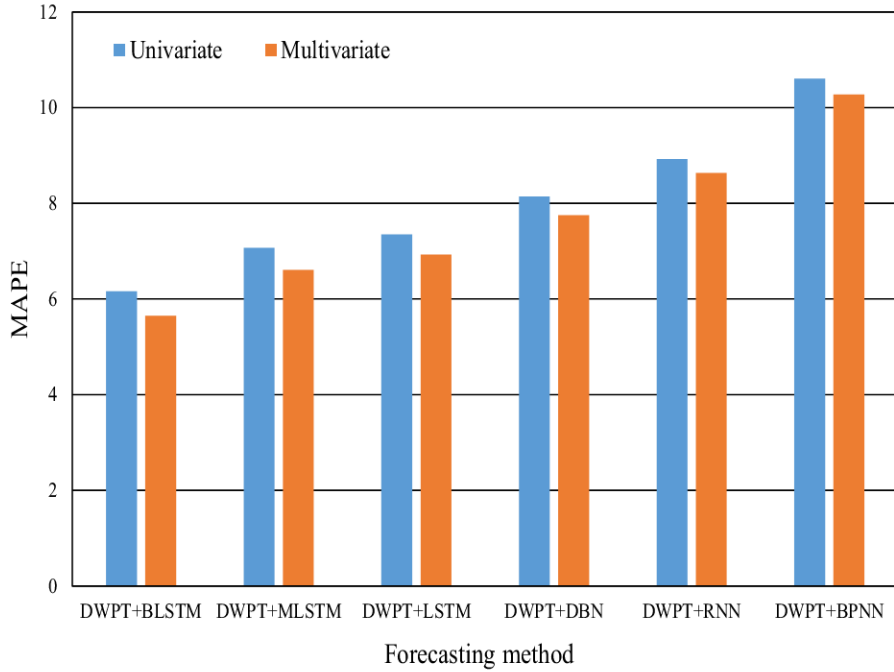


Figure 3.9: Comparison of multivariate and univariate forecasting results for the NREL 1-hour test data.

3.3.3 Multivariate Forecasting Task

In this subsection, the ambient temperature at 80 m altitude is considered an extra feature. Figure 3.9 compares the prediction performance of the proposed model with DWPT+MLSTM and DWPT+LSTM. As we expected, it can be seen that the multivariate frameworks demonstrate slightly higher forecast accuracy than the models without exogenous input. In the multivariate forecasting, DWPT+BPNN and DWPT+RNN produce the MAPE of 10.27% and 8.63%, respectively. For DWPT+DBN and DWPT+LSTM methods, MAPEs of multivariate tasks are 7.75% and 6.92%, respectively. Similar improvements are made for DWPT+MLSTM and DWPT+BLSTM models. Comparing DWPT+MLSTM with DWPT+BLSTM, for the multivariate prediction, DWPT+BLSTM method can improve MAPE by 14.52%. DWPT+BLSTM can predict the most accurate multivariate wind speed forecasting task, which can get the best forecasting metrics in the real data. This

finding can verify the superiority of the proposed DWPT+BLSTM framework.

3.4 Conclusion

Accurate knowledge of the variability and availability of wind speed is a very crucial issue for the operation and scheduling of the smart grid. In this work, a new hybrid deep learning-based approach is proposed for short-term wind speed prediction. First, the DWPT is applied to effectively extract the features of the signal by decomposing the raw wind speed time series into several sub-layers. The input vector is built by using the theory of dynamic reconstruction, which not only increases the accuracy of the results but also decreases the learning complexity by determining the optimal structure of inputs. Moreover, the BLSTM network, as a combination of LSTM networks and bidirectional RNNs is incorporated to capture deep temporal features with high abstractions. The proposed model is evaluated on a publicly available real-world dataset, of which the forecasting accuracy is comprehensively compared to multiple benchmarks in the literature. The proposed BLSTM+DWPT framework shows the smallest metrics and generally achieves the best forecasting performance in the dataset. For example, BLSTM+DWPT has demonstrated 34% and 32% improvement in RMSE and MAE when compared with BLSTM+DWT.

Chapter 4

Deep Spatial-Temporal 2-D CNN-BLSTM Model for Ultra-Short-Term LiDAR-Assisted Wind Turbine’s Power and Fatigue Load Forecasting

In this chapter a LiDAR-aided deep learning model is presented to learn the powerful spatial-temporal characteristics of the input wind fields. The combination of 2-D CNNs and BLSTM units is used to concurrently capture high levels of abstractions in wind fields, thus forecasting wind output power and fatigue load as two representatives of wind turbine responses. The LiDAR wind preview information is used as the 2-D-images of wind fields for the CNN. Moreover, the BLSTM is incorporated with the proposed CNN to improve the forecasting accuracy further and learn deep temporal features. The aero-elastic 5-MW reference wind turbine of NREL is used to evaluate the performance of the proposed model compared to the state-of-the-art deep-learning-based architectures in the recent literature.

This Chapter is organized as follows. Section 4.1 introduces the LiDAR and wind turbine modeling methodologies. In Section 4.2, the overall body of the proposed framework, which consists of 2-D CNN and BLSTM networks, is

presented. Then, the numerical results are presented and discussed in Section 4.3. Finally, the conclusion is drawn in Section 4.4.

4.1 Principle of LiDAR Measurements

Generally, there are two types of LiDAR installations: 1) Nacelle-mounted LiDAR, which is similar to the nacelle vane required to be deployed on the nacelle rooftop and can measure freestream wind at 50 to 200 meters distance in front of the turbine blades as shown in Figure 4.1(a). 2) Ground-based LiDAR, which demands to be located on the ground and can vertically emit a laser beam to measure freestream wind as shown in Figure 4.1(b). A LiDAR sensor mounted on the nacelle can overcome the above-stated disadvantages, as it can provide a sufficiently early preview measurement of the undisturbed inflow over the entire rotor area at a far distance. Moreover, it is worth noting that a nacelle-mounted LiDAR can reliably determine the speed and direction of the wind regardless of the rotor turbulence, which is possible by manipulating the location of the beam in front of the rotor. The wind speed measurement along the direction of i -th LiDAR laser beam can be modeled by equations (4.1) and (4.2) [113].

$$v_i^{los} = \int_{-\infty}^{+\infty} (l_i^x u(a) + l_i^y v(a) + l_i^z w(a)) f_L(a) da \quad (4.1)$$

$$f_L(a) = \frac{e^{-4 \ln 2 (a/W)^2}}{\int_{-\infty}^{+\infty} e^{-4 \ln 2 (a/W)^2} da} \quad (4.2)$$

where $f_L(a)$ is the weighting function at the distance a . The simplified version of equation (4.1) can be expressed by equation (4.3).

$$v_i^{los} = l_i^x u_i + l_i^y v_i + l_i^z w_i \quad (4.3)$$

where v_i^{los} is wind vector $[u_i \ v_i \ w_i]^T$ projection in the i -th focus point in the direction of normalized laser beam vector with the length f_i :

$$\begin{bmatrix} l_i^x \\ l_i^y \\ l_i^z \end{bmatrix} = \frac{1}{f_i} \begin{bmatrix} x_i \\ y_i \\ z_i \end{bmatrix} \quad (4.4)$$

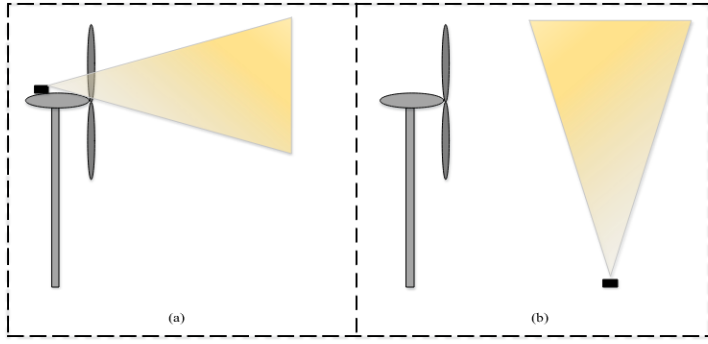


Figure 4.1: Different types of LiDAR-based on installation location.(a) Nacelle-mounted LiDAR. (b) Ground-based LiDAR

4.2 Background Theories

To enhance the forecasting accuracy and reliability of the wind turbine response, it is essential to learn the spatial-temporal patterns, which improves the knowledge of a turbulent wind field. In this section, the structure of the designed wind turbine response forecasting method is described in full detail.

4.2.1 Wind Turbine Modeling

In the real world, the horizontal axis wind turbine of the MW class typically adopts different active de-loading and nacelle direction control strategies by using the predicted wind speed and wind direction data. However, traditional wind field measurement methods such as anemometer and vane have a common drawback. They can only cover a limited close vicinity of their location; therefore, these approaches would not have an appropriate performance to be applied to the wind turbine response prediction task. On the other hand, accurate wind data measurement has a crucial role in the optimal harvesting of wind power and increasing turbine fatigue lifespan by decreasing the induced parasitic load on the blades and main bearing. For example, reference [41] showed that for 7.5° to 15° of yaw error, the power loss in a wind turbine is in the range of 2.4% to 13%.

The wind speed at height p_y and distance p_x from the hub center of the turbine is $v_{p_x, p_y}(a_i)$, which is measured by LiDAR at distance a_i in front of the turbine. On the other hand, the wind field at a distance a_i will reach the turbine after time $t_i = \frac{a_i}{v_{avg}}$, where v_{avg} denotes the average wind speed. By assuming uniform average wind speed for the proposed measurement grid:

$$v_{p_x, p_y}(a_i) = v_{p_x, p_y}(v_{avg} \cdot t_i) \simeq v_{p_x, p_y}(t + t_i) \quad (4.5)$$

$p_x \in [-\varphi, \varphi]$ and $p_y \in [-\gamma, \gamma]$ ($\frac{2\varphi}{\Delta p_x} = \mathbb{R}_{p_x}$ and $\frac{2\gamma}{\Delta p_y} = \mathbb{R}_{p_y}$ are the resolutions in the vertical and horizontal directions). The effective uniform speed that will have the same effect as the wind speed grid at time t_i can be defined as follows:

$$v(t) = \theta(v_{p_x, p_y}(t)) \quad \forall p_x \in [-\varphi, \varphi] \text{ and } p_y \in [-\gamma, \gamma] \quad (4.6)$$

The wind turbine output power can be described by the following equation:

$$\begin{aligned} P_o^{wt}(s) &= \frac{\eta^{wt} P_i^{wt}(s)}{(\tau_m s + 1)(\tau_e s + 1)} \simeq \frac{\eta^{wt} P_i^{wt}(s)}{\tau_m s + 1} \\ &= G(s) P_i^{wt}(s) \end{aligned} \quad (4.7)$$

P_i^{wt} is the input power of the turbine and can be calculated as follows.

$$P_i^{wt} = \frac{1}{2} \rho A_R v^3 C_p(\lambda, \beta) \quad (4.8)$$

v is the magnitude of the wind velocity component which is perpendicular to the rotor plane. From equation (4.8), it can be seen that the wind turbine extracted power increases with the cube of the v . Apart from affecting the generated power, inaccurate estimations of wind speed and wind direction will also have a significant effect on the turbine's structural loads. From the wind farms operator's point of view, a premature fatigue failure problem can be problematic as the drivetrain of a wind turbine needs much more maintenance cost and downtime than the other subassemblies of the wind turbine.

Under this background, the most significant issue is calculating the wind turbine's fatigue load. In this work, we consider the tower bending moment

as a measure of fatigue load [161]. The thrust force, which is the main cause of the tower bending moment, is described by the following equation:

$$F_{thrust}^{wind} = \frac{1}{2} \rho A_R v^2 C_t(\lambda, \beta) \quad (4.9)$$

The details of the C_t and C_p are stated in [52] as 2-D lookup tables.

By using the convolution operation, the wind turbine output power is expressed as:

$$\begin{aligned} P_o^{wt}(t + t_i) &= \int_0^{t+t_i} g(t) P_i^{wt}(t + t_i - \tau) d\tau \\ &= g(t) * P_i^{wt}(\tau + t_i) \end{aligned} \quad (4.10)$$

Finally, it is worth noting that all the above-mentioned procedure can be used for wind turbine fatigue load by replacing Eq. (4.8) with Eq. (4.9). The structure of the proposed deep spatial-temporal feature learning model, namely 2-D CNN-BLSTM, is visualized in Figure 4.2. As presented in the figure, 2-D wind field images and 1-D wind time series data are fed to the 2D-CNN and BLSTM deep learning architecture to extract spatial and temporal features from each wind data, respectively. These branches operate independently of each other until they are concatenated.

4.2.2 Convolutional Neural Network (CNN)

Due to the superior ability of conventional algorithms in solving complex tasks, CNNs have been successfully used in many areas. CNNs have powerful self-tuning & learning capability; thus, they can efficiently capture complex spatial features from highly varying wind flows. The convolutional layers provide translation invariance ability by using a set of learnable kernels and inductive bias of local connectivity, decreasing the number of learning parameters and, consequently, increasing generalization capability. Such a convolution operator is equivalent to moving kernels over spatial positions, which for the q^{th} feature map of the l^{th} layer is defined as given in equation (4.11) [122].

$$x_l^q = f \left(\sum_{p \in N_q} (x_{l-1}^p \otimes k_l^{pq}) + b_l^q \right) \quad (4.11)$$

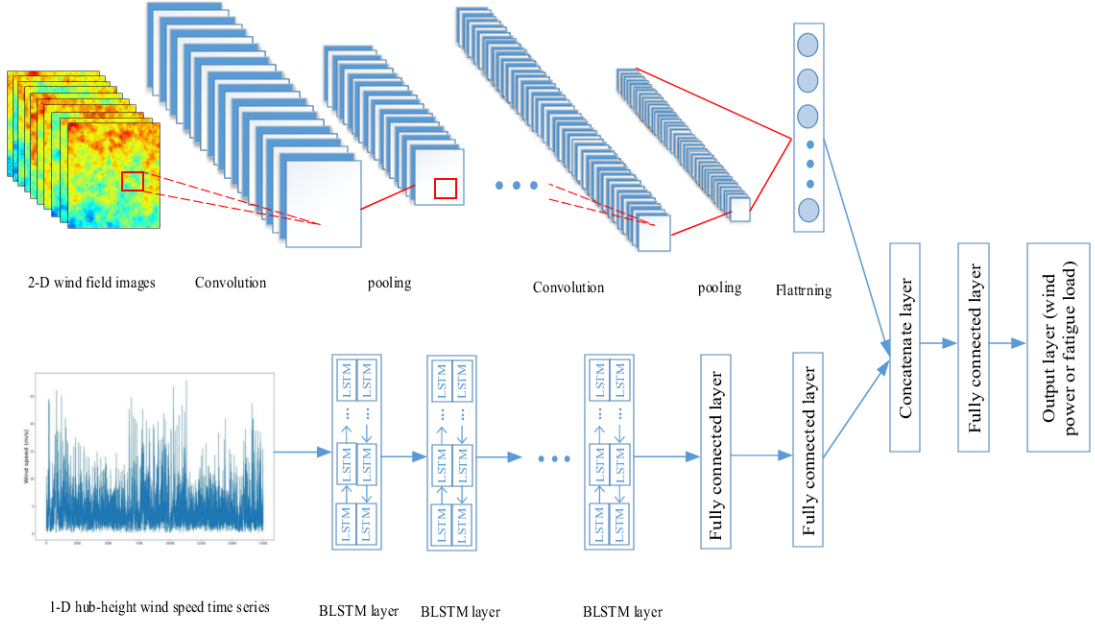


Figure 4.2: Overall Structure of 2-D CNN-BLSTM framework.

$f(\cdot)$ is a nonlinear activation function, and \otimes denotes a convolution operation.

Then, a pooling layer is integrated to reduce the computational cost of the deep CNN network and, consequently the possibility of over-fitting by down-sampling feature maps. The pooling operation can be defined mathematically by:

$$x_l^q = f_{down}(x_{l-1}^q) \quad (4.12)$$

where $f_{down}(\cdot)$ represents the down-sampling function. Average-pooling and max-pooling operations are the two popular pooling strategies in the CNNs. In this work, max-pooling is chosen to produce a feature map containing the most prominent features. Finally, the fully-connected layer is utilized to flatten the 2-D feature maps and make them suitable for putting through the activation function as follows:

$$x_l = g_{fc}(\xi_l x_{l-1} + b_l) \quad (4.13)$$

In a deep CNN with multiple filters with different kernel sizes, deep spatial

features can be effectively extracted. It is worth noting that this benefit emerged due to the shared weights, local connectivity, and receptive fields features of CNNs.

4.2.3 Bidirectional Long Short-Term Memory (BLSTM) Network

The details of the deep BLSTM network can be found in Section 3.1, including the mathematical representation of the blocks used for the proposed hybrid framework.

4.3 Case Study and Numerical Results

In this Section, the simulation environment applied in this research and the details of datasets are explained first, and a comprehensive prediction evaluation and comparison with well-known benchmark models are performed subsequently.

4.3.1 Wind Turbine Simulation Environment

In this work, the 5-MW reference horizontal axis wind turbine of the National Renewable Energy Laboratory (NREL) is used as a full nonlinear aero-elastic model to perform a broad range of wind speeds simulations [67]. Table 4.1 shows the detailed characteristics of the proposed NREL wind turbine.

4.3.2 TurbSim Wind Field Simulator

TurbSim is a full-field, stochastic, turbulent-wind simulator developed by the NREL. It uses statistical models to generate realistic time series of longitudinal, crosswise, and vertical components of the wind field [66]. Taylor's frozen wind hypothesis is utilized to simulate wind signals; that is, the wind field is modeled as a turbulence box marching toward the turbine. Thus, the wind fields do not evolve with time and are assumed to be frozen from the LIDAR focal point until the turbine. The height and width of the wind field grid are

Table 4.1: Characteristics of NREL 5-MW Wind Turbine

Symbol	Parameter	Value
P_{rated}	Rated power	5 MW
M_{rated}	Rated generator torque	43.1 kNm
V_{in}	Cut-in wind speed	3 m/s
V_{rated}	Rated wind speed	11.4 m/s
V_{out}	Cut-out wind speed	25 m/s
h_{hub}	Hub height	90 m
R_{rotor}	Rotor radius	63 m

chosen to be 145 *m* large enough to encompass the entire rotor disk of the proposed wind turbine. Moreover, the hub is horizontally centered in the grid, so the top of the grid can be determined by the turbine hub height plus the rotor radius.

4.3.3 FAST Wind Turbine Simulator:

The fatigue, aerodynamics, structures, and turbulence (FAST) code developed by the NREL is used to simulate the response of the proposed turbine by providing a full nonlinear and high-fidelity turbine response simulation [68]. The wind field vectors created by the TurbSim are applied to the FAST turbine simulator to compute the turbine's output signal and state vector. In this study, electrical generator power (GenPwr) and low-speed shaft torque (LSShftTq) are considered as the wind turbine responses' representatives. It should be noted that we enabled the degrees of freedom (DOFs) associated with first and second blade flap-wise modes (2×3 DOFs), first and second tower side-to-side modes (2 DOFs), first and second tower fore-aft modes (2 DOFs), first and second blade edgewise mode (2×3 DOFs), drive-train mode (1 DOF), and generator mode (1 DOF).

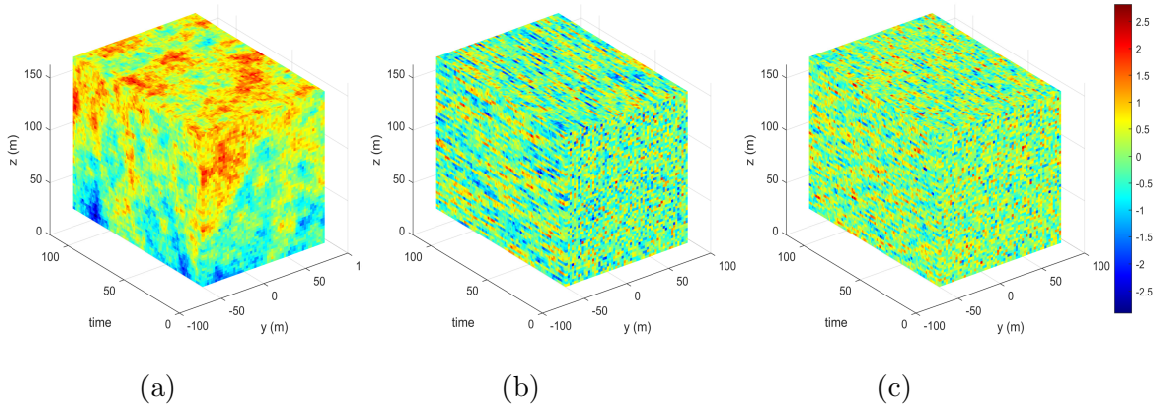


Figure 4.3: Different wind field components generated by TurbSim. (a) streamwise (longitudinal) component u . (b) transverse (crosswise) component v . (c) vertical component w .

4.3.4 Data Description

The proposed approach aims to perform the ultra-short-term forecasting of wind turbine responses by taking the 2-D-images of wind fields and hub-height wind speed time series as inputs for the CNN and BLSTM networks, respectively. This means that besides hub height wind speed time series, upcoming wind fields are also utilized to increase the capability of the proposed model on capturing complex wind data abstractions.

As mentioned earlier, the NREL TurbSim package generates turbulent wind fields, and the NREL FAST turbine simulator is used to model high-order aeroelastic nonlinear wind turbines. As depicted in Figure 4.3, each Turbsim simulation generates 3×3 -D wind field components vectors $u_{ph \times pv \times pt}$, $v_{ph \times pv \times pt}$ and $w_{ph \times pv \times pt}$ in x, y, and z directions, respectively, where ph and pv denote the number of horizontal and vertical points in the spatial grid, respectively, and pt represents the temporal dimension of the vector. A broad range of the wind fields is generated according to various mean longitudinal wind speeds from 6 to 24 m/s with 2 m/s resolution steps to ensure that the forecasting model could be trained with different wind field characteristics. The complete data set contains 3000 wind fields and the corresponding electrical generator power and low-speed shaft torque. In this work, the training, validation and

Table 4.2: Cross-Validation results of proposed model with some typical BLSTM structures for 1-step ahead power forecasting.

BLSTM structure	RMSE (kW)	MAE (kW)	MAPE (%)	Online execution time (ms)
[100 100]	63.48	29.14	2.26	0.31
[250 250]	63.01	28.78	2.21	0.38
[100 100 50]	58.13	25.64	1.93	0.46
[250 250 50]	56.27	23.77	1.92	0.61
[250 250 100]	61.22	26.94	2.02	0.73
[250 250 250]	61.38	27.18	2.11	0.81

testing sets account for 75%, 15%, and 10% of the dataset, respectively [63].

4.3.5 Evaluation Criteria For Wind Turbine Response Forecasting

The details of evaluation metrics to evaluate the forecasting performance can be found in Subsection 3.2, including the mathematical models of the metrics.

4.3.6 Results and Comparisons

To verify the efficiency and validity of the proposed framework, several single and hybrid forecasting approaches that have been proposed in the literature are chosen as the benchmarks. ARIMA, MLP, DBN, IPDL, GRU, LSTM, and BLSTM models use 1D-wind speed time series, 2D-CNN use 2D-wind fields images, and 2D-CNN-MLP, 2D-CNN-GRU, and 2D-CNN-LSTM use both of them similar to the proposed 2D-CNN-BLSTM model. As these machine learning models are completely data-dependent, all hyperparameters, such as the number of neurons in each layer and the number of layers in each model, are optimally tuned using the training data according to common practice recommended by the deep learning community [48]. The optimal number of

hidden layers for MLP model is determined to be 2, with 50 hidden nodes in each layer. The DBN is established by using three hidden layers with 100, 125, and 125 units, respectively. The overall structure of the GRU, LSTM and B-LSTM networks are composed of three main hidden layers with 250, 250, and 50 units, respectively. The IPDL model consists of three stacked layers with a linear regression model at the top. The CNN structure comprises six layers, including three convolution layers, three pooling layers, and a flattening layer. To verify the performance of the validation, the 1-step ahead power forecasting case study is repeated for different network structures. Table 4.2 shows the cross-validation results of some typical BLSTM structures with a different number of layers and blocks. As shown in this table, both the increase and decrease in the network parameters reduce the performance according to the forecasting indices. The online computation time of the proposed method for different network parameters is calculated in Table 4.2. Considering that the sampling time scale of the forecasting is 10 s or longer, the computational time of around 0.6 ms is relatively fast enough to guarantee reliable and safe wind turbine real-time operation. Moreover, all models are implemented in Python with the Keras library and TensorFlow as the backend [1]. The workstation used is configured with an Intel Core TM i7-8700 3.2 GHz CPU, NVIDIA GPU GeForce GTX 1070 GPU, and 32 GB of RAM.

Table 4.3 compares the forecasting results and provides the average test RMSE, MAE, and MAPE for ultra-short-term generated power and load predictions with 1-step (10 sec) and 2-step (20 sec) ahead tasks, respectively. This table clearly shows that the proposed method (2D-CNN-BLSTM) outperforms the other benchmarking models and has the best performance in both 1-step and 2-step ahead forecasting tasks. The results show that machine learning models perform better than ARIMA as a linear statistical model. DBN has the largest error range and randomness, which is due to the pretraining and supervised training process. The IPDL model yields more accurate predictions when compared to the classic DBN. According to the results, GRU and

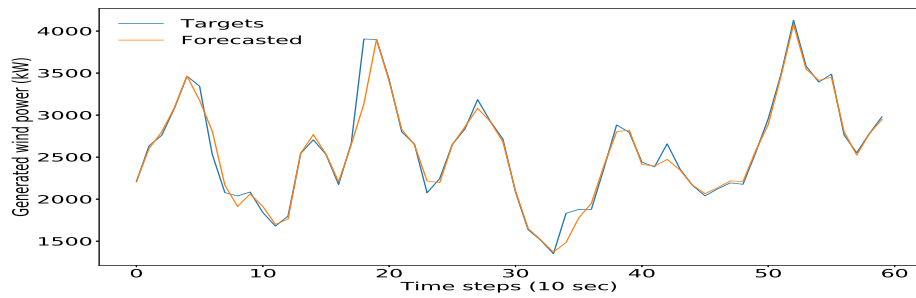
Table 4.3: Forecasting performance comparison for 1-step and 2-step ahead tasks.

Method	1-Step (10 sec)				2-step (20 sec)				1-Step (10 sec)				2-step (20 sec)			
	RMSE (kW)	MAE (kW)	MAPE (%)	RMSE (kW)	MAE (kW)	MAPE (%)	RMSE (kN.m)	MAE (kN.m)	MAPE (%)	RMSE (kN.m)	MAE (kN.m)	MAPE (%)	RMSE (kN.m)	MAE (kN.m)	MAPE (%)	
ARIMA [43]	351.80	219.17	21.76	463.82	424.34	32.43	591.51	326.42	32.27	746.58	717.64	43.85				
DBN [92]	338.63	214.31	20.59	458.91	408.70	32.02	589.72	318.43	29.85	718.89	668.54	40.66				
MLP [45]	325.68	196.64	19.32	424.78	391.36	27.56	560.59	295.98	27.49	650.23	577.73	34.54				
GRU [84]	277.63	163.73	15.81	369.46	342.68	24.07	535.97	255.62	20.93	548.01	437.58	27.11				
LSTM [153]	281.02	165.66	16.04	365.71	338.51	22.83	534.71	255.57	20.07	542.23	435.43	25.64				
IPDL [77]	267.16	159.93	15.38	342.07	312.22	21.39	466.69	247.91	19.72	537.64	421.80	23.96				
BLSTM [25]	263.01	154.38	15.29	330.08	298.21	21.01	454.46	239.34	17.96	518.56	398.44	23.80				
2D-CNN	234.02	107.08	8.64	241.29	140.37	9.25	252.95	97.9	8.11	282.95	193.81	10.86				
2D-CNN-MLP	176.23	77.31	6.61	190.57	139.49	8.49	197.17	87.94	7.66	234.86	185.55	9.94				
2D-CNN-GRU	150.89	52.97	3.66	160.05	68.49	4.73	110.38	59.18	5.31	153.34	123.02	6.90				
2D-CNN-LSTM	148.33	51.38	3.61	155.61	64.82	4.46	110.22	59.19	5.29	150.59	111.56	5.73				
2D-CNN-BLSTM	58.34	24.73	1.98	67.02	41.05	2.74	102.61	51.22	4.55	145.11	105.58	5.41				

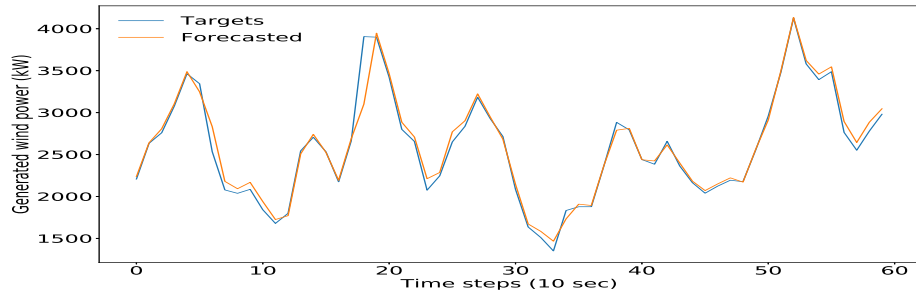
LSTM approaches outperform shallow architecture, MLP, since these deep recurrent networks can better model the highly nonlinear temporal features of wind time series. As the variant of LSTM, the forecasting metrics of GRU are closer to those of LSTM, but in 2-step ahead scenarios LSTM has a remarkable improvement in all criteria. BLSTM is the best single-time series-based architecture compared to the LSTMS and MLP models. Moreover, using wind fields has a significant effect on the prediction accuracy, which can be understood by comparing the first three models, MLP, LSTM, BLSTM, with other 2D-CNN-based ones. For example, the RMSE of 2D-CNN-MLP for 1-step and 2-step ahead wind power predictions are 176 kW and 190.57 kW, respectively, which are increased to 325.68 kW and 424.78 kW for the single MLP model. MAPE result of 2D-CNN-BLSTM for 1-step predictions is 1.98 which reaches 2.74 in the 2-step compared to the best time series-based approach, single BLSTM, which has MAPE of 15.29 and 21.01 in 1-step and 2-step, respectively. Therefore, applying single-time series-based models for longer-term predictions cannot yield reliable performance. 2D-CNN-MLP has 24.69% power RMSE and 22.05% load RMSE improvements over a single 2D-CNN. These improvements are further increased to 36.61% and 56.42% for the power RMSE and load RMSE results, respectively, when the MLP is replaced by the deep LSTM network. The more precise forecast shows the better generalization capability of the deep recurrent models.

The proposed 2D-CNN-BLSTM obtains better results compared to 2D-CNN-LSTM. 2D-CNN BLSTM outperforms 2D-CNN-LSTM with 51.86% and 13.46% MAE improvements in power and load 1-step ahead forecasts. Furthermore, this model decreases MAE by 36.67% and 5.36% for power and load 2-step ahead prediction tasks, respectively. The higher accuracy of 2D-CNN-BLSTM indicates the superiority of the bidirectional learning method to effectively capture the previous and future hidden features of the proposed wind data.

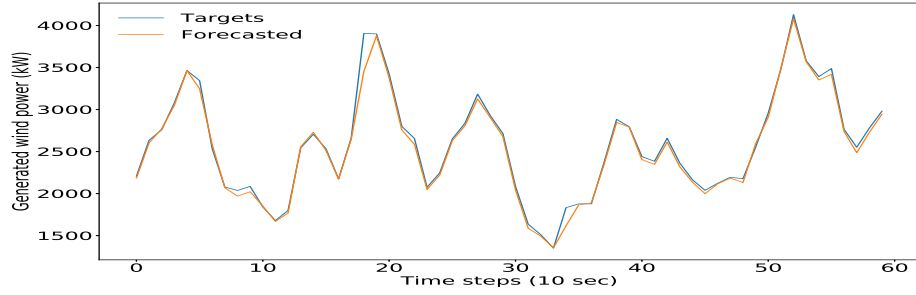
To provide better visualization, Figure 4.4 demonstrates the wind power 1-



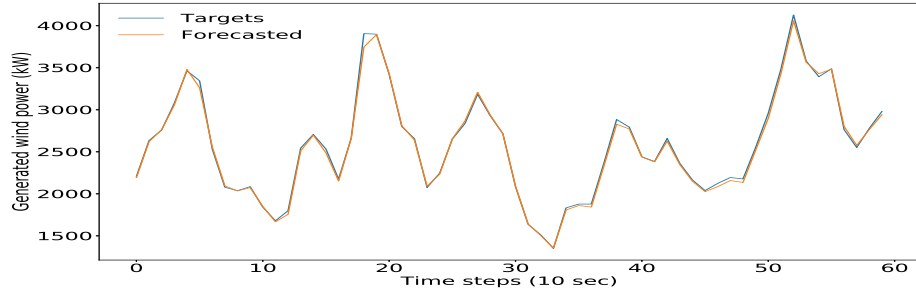
(a)



(b)



(c)



(d)

Figure 4.4: Wind power forecasting comparison of four 2D-CNN-based models for the first 60 steps (600 sec) of test data. (a) 2D-CNN. (b) 2D-CNN-MLP. (c) 2D-CNN-LSTM. (d) 2D-CNN-BLSTM.

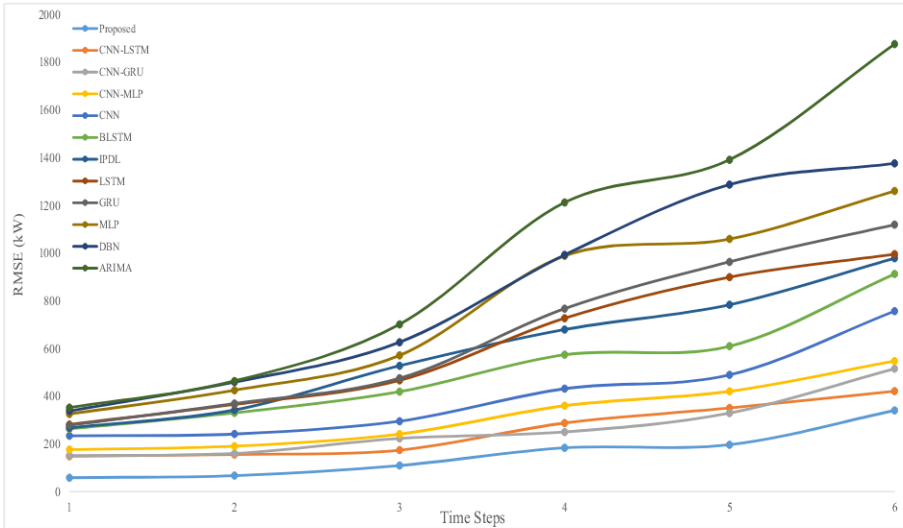
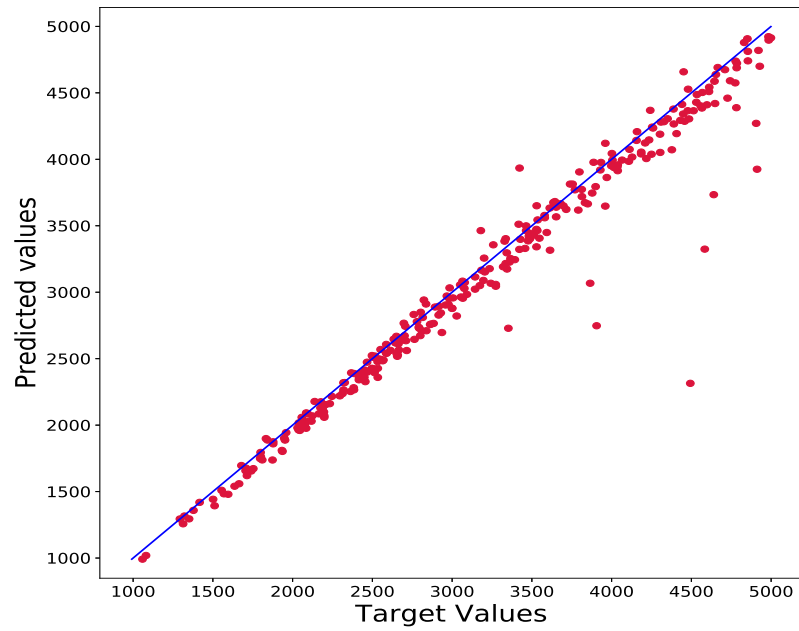


Figure 4.5: Comparison of power forecasting RMSE results for 1-step up to 6-step ahead tasks (step time = 10 sec).

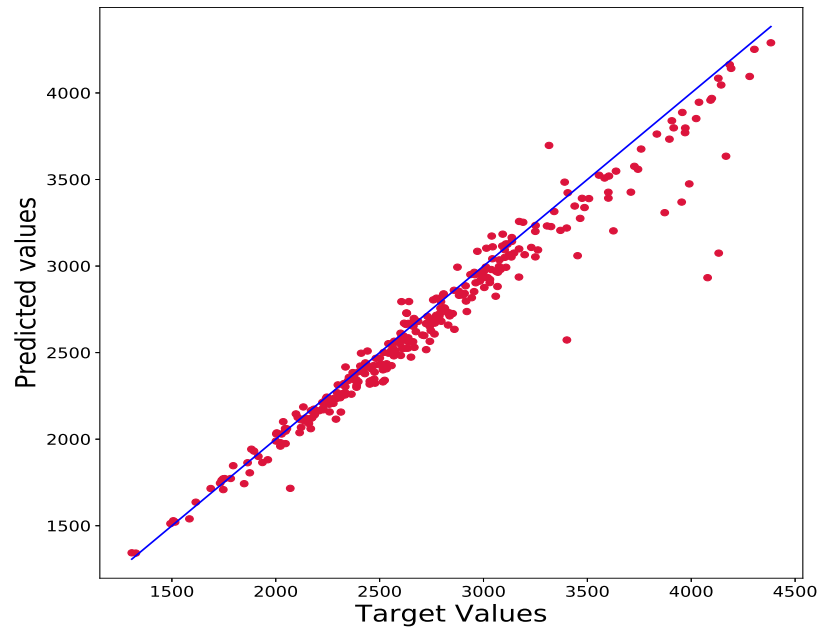
step ahead prediction results of the four models, which use both 1D-wind speed time series and 2D-wind fields as inputs. As shown in this figure, 2D-CNN is dominated by 2D-CNN-MLP, and 2D-CNN-LSTM has relatively better performance in spike points than both of them. Our deep hybrid model significantly outperforms all of them and can follow the sharp spikes accurately.

Figure 4.5 depicts the performance comparison of all single and hybrid models for extended time horizons from 1-step ahead to 6-step ahead prediction tasks. For the extended prediction time step, hybrid models with more complex structures are needed to achieve high accuracy by using both 1-D and 2-D data. As shown in Figure 4.5, single architectures are dominated by hybrid deep learning models in all time horizons. BLSTM and IPDL have relatively good performance compared to CNN-based models; however, for larger forecasting time steps, the plot shows that hybrid frameworks outperform single ones.

Figure 4.6 illustrates the regression responses of the proposed method for wind output power and fatigue load as two representatives of wind turbine responses. As seen in this figure, the predicted values mostly stay below the



(a)



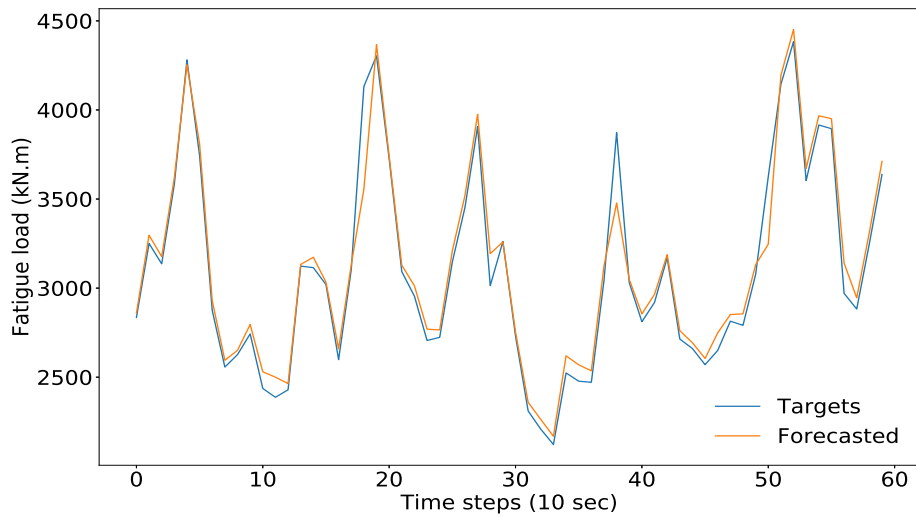
(b)

Figure 4.6: Regression plots of the proposed method (2D-CNN-BLSTM): (a) Wind power (kW); (b) fatigue load (kN.m).

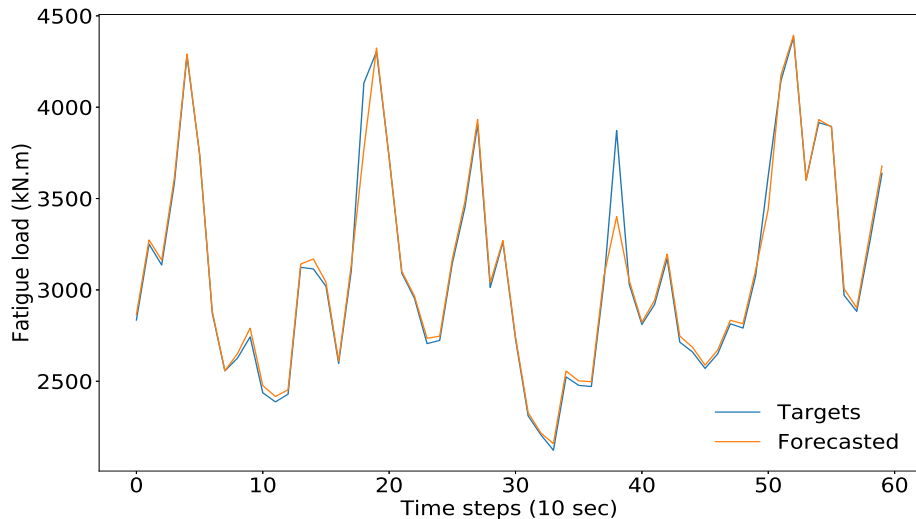
blue line and show slightly higher error in wind powers above 4500 kW and higher than 4000 kN.m fatigue loads. The fatigue load case has faced some higher errors compared to the wind power case, which seems to be reasonable in that the fatigue load is highly influenced by the dynamic interactions between the turbine structure and the wind flow. Overall, as it is clear, our proposed method shows acceptable performance in both tasks and can help us to make more accurate results.

To investigate the effect of wind fields snapshots on the performance of our proposed model in another way, another extension of 2D-CNN-BLSTM is designed as our baseline. This baseline methodology only uses a longitudinal component of the wind field, u , instead of entire wind field components. Figure 4.7 compares the 1-step ahead load prediction results of proposed and baseline models. As it is clear, our proposed method, by considering all wind fields components, shows slightly better performance and generalization capability than the baseline model, which considers only streamwise component, especially when the load time series has an abrupt change. It should be noted that the main limitation of this work lies in the fact that these improvements are conditioned to have an adequate preview of wind data provided by the LiDAR sensor, which is still a high-cost solution. In case the LiDAR system is failed due to an unknown reason and consequently, 2D wind field images are not available, the proposed framework can still be used to forecast as it is a kind of ensemble learning and combined CNN and BLSTM networks in a parallel manner. Figure 4.8 compares the wind power 1-step ahead prediction results of the three models, which previously used both 1D-wind speed time series and 2D-wind fields as inputs. As shown in this figure, all of the methods have relatively higher prediction error than the normal situation (Figure 4.4). The figure shows that the predicted values of 2D-CNN-BLSTM generally conform well with the target values with low average error levels.

Figure 4.9 compares the ultra-short-term generated power and load 1-step forecasting performance of the proposed model with spatiotemporal prediction



(a)



(b)

Figure 4.7: Fatigue load forecasting results comparison of proposed 2D-CNN-BLSTM and baseline model for the first 60 steps (600 sec) of test data. (a) baseline model. (b) proposed 2D-CNN-BLSTM model.

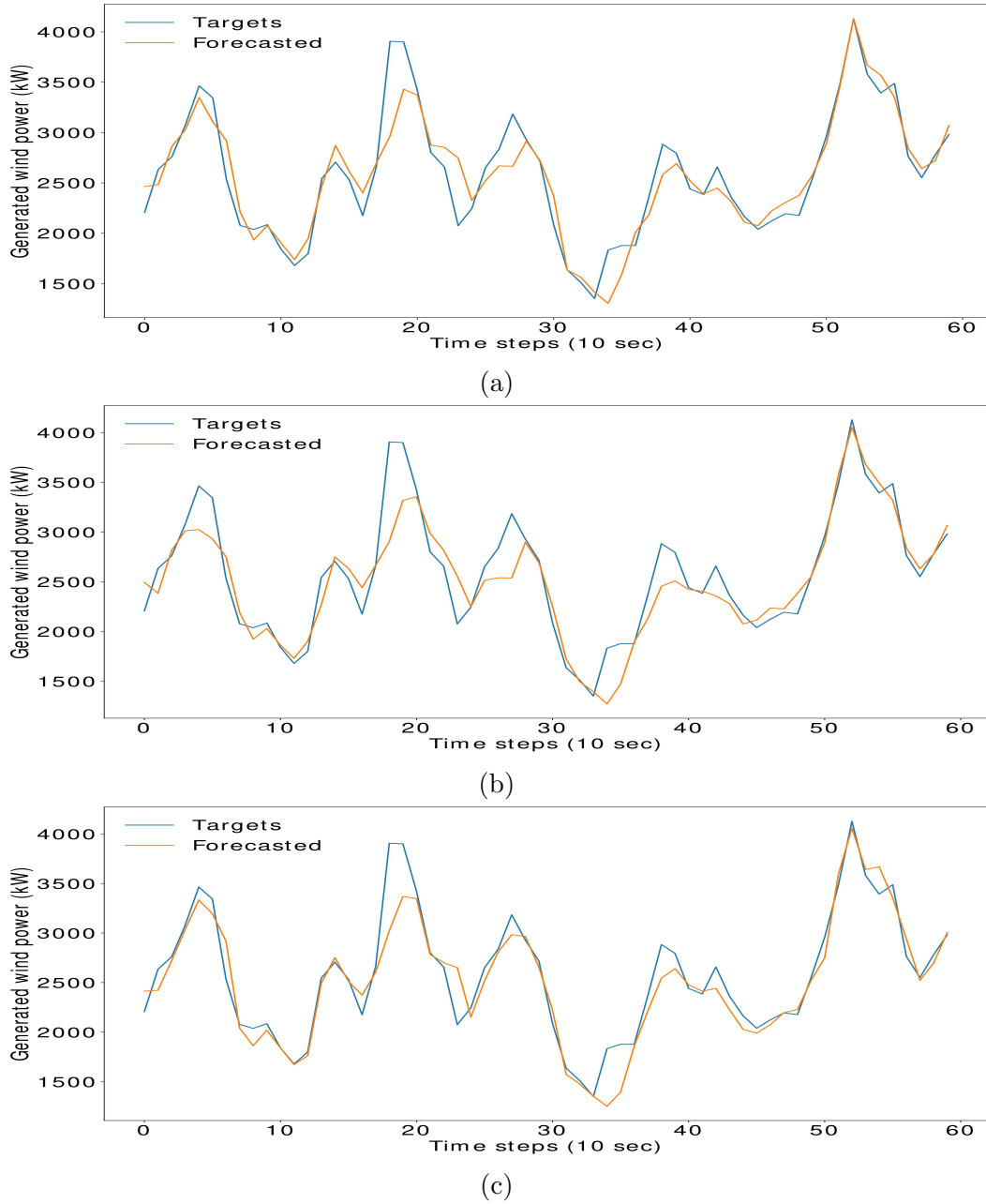


Figure 4.8: Wind power forecasting comparison of three Image-based models for the first 60 steps (600 sec) of test data in case of LiDAR failure. (a) 2D-CNN-MLP. (b) 2D-CNN-LSTM. (c) 2D-CNN-BLSTM.

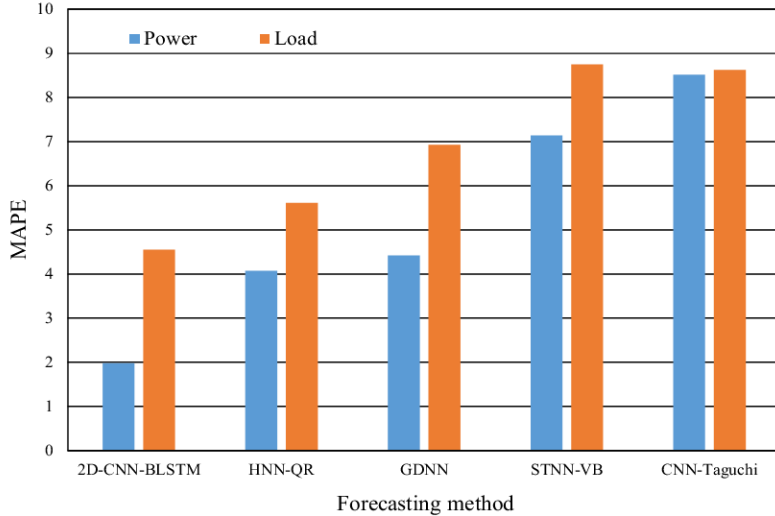


Figure 4.9: Comparison of power and fatigue load forecasting results with different spatiotemporal models.

methods which have been recently employed in the literature, including GDNN [75], CNN-Taguchi [56], HNN-QR [163], and STNN-VB [95]. It is worth noting that the procedure of designing an optimal structure for the other frameworks is similar to that of the proposed 2D-CNN-BLSTM model. In the generated power prediction task, CNN-Taguchi and STNN-VB produce the MAPE of 8.52% and 7.14%, respectively. For GDNN and HNN-QR models, MAPEs of power forecast are 4.42% and 4.07%, respectively. Comparing HNN-QR with 2D-CNN-BLSTM, for the wind power prediction, 2D-CNN-BLSTM method can improve MAPE by 51.35%. A similar trend can be seen for load forecasting. 2D-CNN-BLSTM can forecast the most accurate ultra-short-term power and load prediction tasks, which can get the best forecasting metrics. This finding can verify the superiority of the proposed 2D-CNN-BLSTM model.

4.4 Conclusion

This work develops a novel LiDAR-assisted deep 2-D CNN-BLSTM model for the ultra-short-term prediction of future wind turbine responses using upcoming sequences of full wind field components and hub-height wind speed time series before reaching the turbine blades as inputs. As a data-driven framework, the performance of the proposed model is determined solely by the potential interactions hidden in the wind field and time series data rather than the physical equations or predetermined distribution types. Thus, it can avoid the dual risks of model incorrectness or distribution type misspecification. The NREL 5-MW reference horizontal axis wind turbine with FAST are utilized for simulations. Realistic 3-D wind field components vectors are generated by NREL TurbSim. The proposed 2-D CNN-BLSTM model is designed for ultra-short-term forecasting of wind turbine response and shows the high-quality outputs with the smallest metrics. For example, it has demonstrated 78% and 75% improvement in RMSE compared to single BLSTM and 2-D CNN models, respectively.

The proposed model employs 2D-CNN and BLSTM networks to better handle complex spatial-temporal features from the highly variable wind data compared to conventional forecasting methods, which simply use historical time series data. The main advantage of the proposed model over other deep learning-based forecasting methods is that it uses wind preview information provided by LIDAR as an advanced remote sensing wind measurement technology. Thus, it can be helpful for wind farm operators as an efficient tool in yaw misalignment and de-loading control strategies.

Chapter 5

Deep Reinforcement Learning-Based Self-scheduling Strategy for a CAES-PV System Using Accurate Sky Images-Based Forecasting

In this chapter, a model-free DRL method is presented to optimize the CAES energy arbitrage in the presence of a sky images-based short-term solar irradiance forecasting model. In this study, the following challenges have to be addressed. (i) Most data-driven solar irradiance prediction models have employed networks (1-D and 2-D) in a serial manner. In doing so, the first network's extracted features have a significant influence on the next network's training. (ii) The one-directional LSTM structure solely obeys the recursive procedure, which feeds back the previous information in an iterative manner that could introduce some error in the prediction of spike points. (iii) Most CNN-based approaches, instead of using 2-D images, have just used time series-based matrices by converting 1-D time series data to a matrix form and then applying it to the CNN. Considering the limitations of previous studies, we propose a DRL-based real-time self-scheduling framework for a CAES-PV facility participating in the energy market incorporating the thermodynamic characteristics of the CAES technology. Incorporating a com-

prehensive nonlinear mathematical model of the CAES system in the presence of the highly random and fluctuant solar irradiance on cloudy days, makes the self-scheduling problem’s environment very complex for the DRL agent. The proposed model properly learns the optimized control actions for CAES-PV facility under such a complicated environment. DRL can optimize scheduling policy directly based on the historical data compared to pdf-dependent models such as stochastic programming. From the DRL agent’s point of view, its phenomenal adaptivity and ability to output decent scheduling results are highly attributed to the function approximation of DNN. In this context, a novel deep-learning-based 2-D CNNs and BLSTM model for high-precision short-term solar irradiance forecasting is incorporated with DRL framework. Sky images and numerical measurements are used to capture high levels of abstractions in solar irradiance. It should be mentioned that the studied CAES-PV is a privately-owned price-taker facility that has a very small capacity compared to the supply-side size of the market; thus, its operation cannot alter the market price.

This Chapter is organized as follows: Section 5.1 provides the problem formulation of the proposed environment model for the DRL framework, CAES facility model, including its thermodynamic characteristics, and deep 2-D CNN-BLSTM forecasting model with sky images. Then, Section 5.2 describes the proposed DRL-based controller for the CAES-PV system. The case studies used to assess the effectiveness of the proposed controller are presented in Section 5.3. Lastly, Section 5.4 gives a conclusion.

5.1 Environment Model and The Hybrid Forecasting Framework

In this Section, the comprehensive mathematical model of the CAES facility is formulated, where its thermodynamic characteristics are taken into account. The deep-learning-based hybrid 2-D CNN-BLSTM model for solar irradiance prediction using sky images is presented next. All variables and parameters

in the equations are also summarized at the beginning of the paper as nomenclature for quick reference.

5.1.1 CAES Modeling

The cavern pressure, air flow rate (AFR), and the efficiency of the compressor/turbine are the most essential thermodynamic conditions that can limit the energy capacity of the CAES. The goal of the CAES-PV system is to maximize its profit through participation in the energy market. In this study, a comprehensive nonlinear mathematical model of CAES system based on the thermodynamic characteristics to describe the CAES behavior more realistically is formulated as follows:

$$OC_t = C_t^{NG} + P_t^{dch} \cdot \mu^e + P_t^{ch} \cdot \mu^c \quad \forall t \in T \quad (5.1)$$

$$SoC_{t+1} = SoC_t + \zeta (SoC_t, P_t^{ch}) - \psi (P_t^{dch}) \quad \forall t \in T \quad (5.2)$$

$$SoC^f \leq SoC_{t+1} \quad \forall t = T \quad (5.3)$$

$$SoC_1 = SoC^i \quad \forall t \in T \quad (5.4)$$

$$P_{min}^{ch} \cdot I_t^{ch} \leq P_t^{ch} \leq P_{max}^{ch} \cdot I_t^{ch} \quad \forall t \in T \quad (5.5)$$

$$P_{min}^{dch} \cdot I_t^{dch} \leq P_t^{dch} \leq P_{max}^{dch} \cdot I_t^{dch} \quad \forall t \in T \quad (5.6)$$

$$I_t^{ch} + I_t^{dch} \leq 1 \quad \forall t \in T \quad (5.7)$$

The operating cost (5.1) consists of three terms. The first term represents the cost of burning natural gas during discharge; the second and third terms denote the operational and maintenance costs of the expander and compressor, respectively. In (5.2), the state of charge of the air storage cavern is defined for the next hour. The initial and minimum SoC levels of the cavern

are calculated in (5.3) and (5.4), respectively. Equations (5.5) and (5.6) constrain the charging and discharging capacities of the CAES, respectively. The operational mode constraint of the CAES facility is specified by (5.7), where the CAES facility can not charge and discharge simultaneously.

In [54, 126, 167], the thermodynamic-based relationships during charging/discharging are investigated. It is shown that the pressure of the cavern plays a critical role in AFR during charging/discharging. During the charging of the cavern by the compressor, the cavern pressure starts to increase, and consequently, the compressor AFR decreases. Therefore, AFR during the charging process can be defined as a function of the cavern SoC. During the discharge process, based on the data in [167], as the operating point of the high pressure (HP) turbine goes below the nominal value, so decreases the turbine's efficiency, making AFR per MW greater, thus increasing natural gas consumption and HR.

Based on the above discussion, discharging, charging, and the cost of natural gas consumption functions can be represented as follows:

$$\zeta(SoC_t, P_t^{ch}) = \frac{AFR^{ch}(SoC_t) \times 3600 \times P_t^{ch}}{AMC^{max}} \quad (5.8)$$

$$\psi(P_t^{dch}) = \frac{AFR^{dch}(P_t^{dch}) \times 3600 \times P_t^{dch}}{AMC^{max}} \quad (5.9)$$

$$C_t^{NG} = HR(P_t^{dch}) \times P_t^{dch} \times \lambda^{NG} \quad (5.10)$$

The aforementioned equations for considering the thermodynamic conditions are modeled as linear interpolations or step functions in [54, 126, 167], which have two main drawbacks: 1) They increase the number of auxiliary and binary variables; thus, their high computational complexity limits the usefulness of such models for online energy management tasks. 2) step functions' discontinuities and the approximate nature of the linear interpolations could cause costly operational decisions, and consequently unprofitable energy management for the facility.

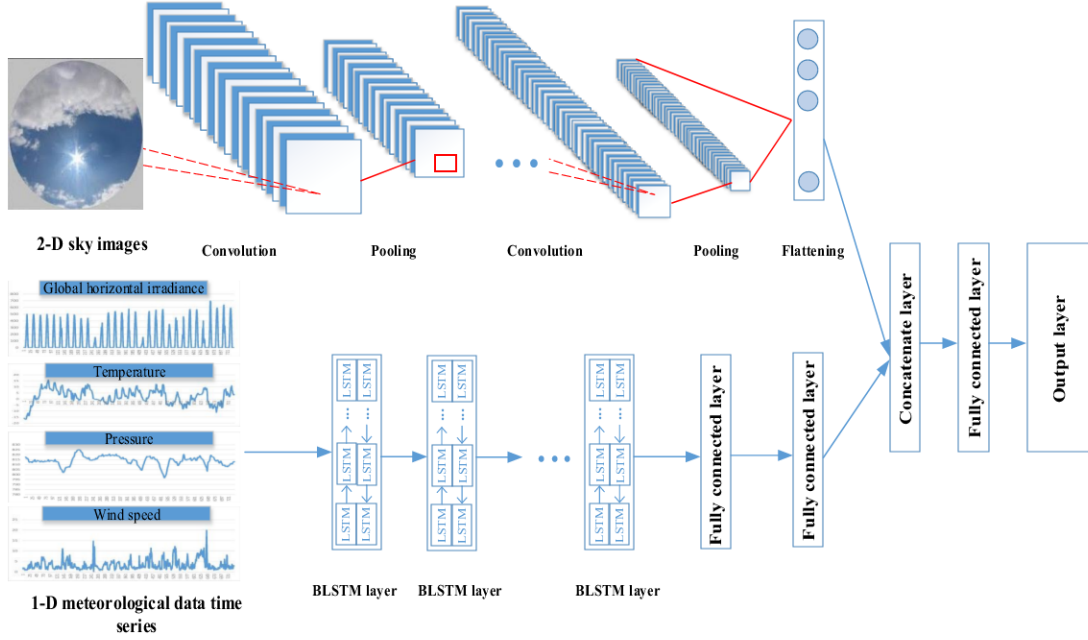


Figure 5.1: The schematic of proposed hybrid 2-D CNN-BLSTM solar irradiance forecasting model.

5.1.2 Deep Hybrid 2-D CNN-BLSTM Forecasting Model

Boosted by an aggressive increase of PV generation in power and energy markets, an accurate and stable prediction of solar forecasting has gained much attention in recent years. Solar irradiance plays a crucial role in the forecast of solar power generation and is highly influenced by meteorological and atmospheric variables. However, a comprehensive sky image-based forecasting model for solar irradiance has not yet been well-studied. In this study, a hybrid solar irradiance forecasting framework is presented, in which a sequence of sky images and time series of different meteorological components are employed by deep CNN and BLSTM networks, respectively. The numerical meteorological features, including global horizontal irradiance (GHI), atmosphere pressure, relative humidity, temperature, direct normal irradiance, and wind speed, are employed to increase the capability of the proposed hybrid forecasting framework for capturing complex solar data abstractions. In addition, the calendar

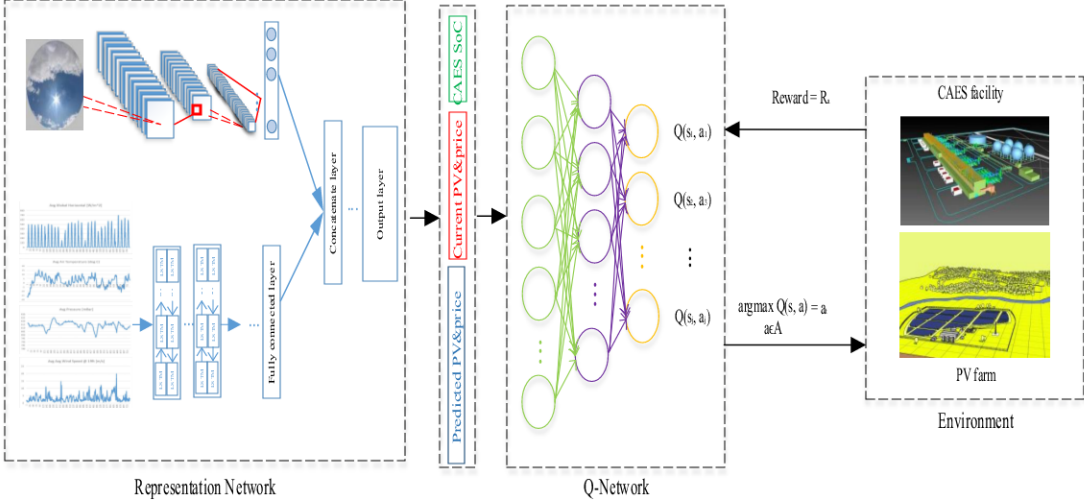


Figure 5.2: The overall diagram of the proposed DRL+2-D CNN-BLSTM for CAES-PV self-scheduling problem.

features, i.e., the hour of the day and month of the year, are included as input labels. The structure of the proposed deep 2-D CNN-BLSTM forecasting model is visualized in Figure 5.1. The details of the deep BLSTM network can be found in Subsection 4.2 including the mathematical representation of the networks for the proposed hybrid framework.

5.2 Proposed Algorithm

This Section presents the main concepts of the real-time energy management of a CAES-PV, where the thermodynamic characteristics of CAES facility, stochastic generation of PV panels, and uncertainty in real-time electricity price are taken into account. The overall diagram of the proposed framework, DRL+2-D CNN-BLSTM, is illustrated in Figure 5.2. The fundamental elements of the proposed DRL-based controller for the scheduling problem of the CAES-PV system are defined as follows:

5.2.1 Modeling PV-CAES Real-Time Energy Management Problem as a Markov Decision Process

The energy management problem of PV-CAES can be formulated as Markov Decision Process (MDP) with discrete time step T . The decision-making process of situations with partly random outcomes that are partly under the control of a decision maker can be mathematically modeled by MDP, which can be solved by the DRL algorithm. A finite horizon discounted MDP is a five-tuple $(\mathbf{S}, \mathbf{A}, \mathbf{P}(\cdot, \cdot), \mathbf{R}(\cdot, \cdot), \gamma)$, where \mathbf{S} is the system states vector, \mathbf{A} is the action vector, $\mathbf{P}(\cdot, \cdot)$ is the function of state transition, $\mathbf{R}(\cdot, \cdot)$ is the immediate reward function set, and $\gamma \in [0, 1]$ is a discount factor. The essential details about the MDP framework corresponding to the energy management problem of CAES-PV are provided as follows.

1. State space: The system state space vector at a time step t is represented as $s_t = \{SoC_t, \lambda_t^e, \hat{\lambda}_{t+1}^e, P_t^{PV}, \hat{P}_{t+1}^{PV}\}$. This vector encapsulates five types of information: (1) SoC_t represents the state of charge of CAES at t ; (2) λ_t^e and $\hat{\lambda}_{t+1}^e$ indicate the current and forecasted electricity price for time t and $t + 1$, respectively; (3) P_t^{PV} and \hat{P}_{t+1}^{PV} denote the current and forecasted available PV power for time t and $t + 1$, respectively. Based on the predicted price and PV power, additional information signals are provided in the state vector to make the best control action by the DRL agent. Moreover, it is worth noting that, according to the Markov property of MDP, the conditional probability distribution of a state solely depends upon the previous one step, not on any memory.
2. Action space: Given the CAES-PV system state at time step t , the decision action is represented by a_t which corresponds to the charging/discharging power decisions. The action vector a_t is limited by the set of all feasible actions determined by the CAES-PV system framework at time step t defined in (5.1)-(5.10). Let $a_t \in A_t$ be positive during the charging mode of the CAES and negative when it is discharging. Due to the limit of the allowed maximum charging/discharging power of the

CAES, action a_t is constrained as below [126]:

$$-P_{max}^{dch} \leq a_t \leq P_{max}^{ch} \quad (5.11)$$

- 3. State transition: The mapping $T^s : s_t \times a_t \rightarrow P_t^s$ is the transition from the state of the system at time t to the state at $t + 1$ by choosing action a_t , where $P_t^s = p(s' = s_{t+1} | s = s_t, a = a_t)$.
- 4. Reward: The agent receives the immediate reward $R_a(s, s')$ at time step t after transition from the state s to the new state s' . From a CAES-PV system scheduling standpoint, such a function is equivalent to the net profit of the CAES-PV operation cost at time step t , which is defined as given in equation (5.12). The first term in the reward function shows the energy arbitrage revenue and the second term is the operation cost of the CAES facility.

$$(P_t^{PV} + P_t^{dch} - P_t^{ch}) \times \lambda^e - OC_t \quad (5.12)$$

The cumulative rewards for the proposed energy management problem are denoted as [17]:

$$R^{\text{cumulative}} = \sum_{t=1}^T (P_t^{PV} + P_t^{dch} - P_t^{ch}) \times \lambda^e - OC_t \quad (5.13)$$

5.2.2 Deep Reinforcement Learning

The action-value function determines the quality of the action under a given system state for the charging/discharging decision of the CAES-PV system, which is defined as [49]:

$$Q^\pi(s, a) = \mathbb{E}^\pi \left[\sum_{n=0}^{N-1} (R_{t+n} | s = s_t, a = a_t) \cdot \gamma^n \right] \quad (5.14)$$

The discount factor γ makes a balance between the importance of the immediate reward and future rewards. The CAES-PV system charging/discharging policy π maps from the system states to the charging/discharging schedule.

This energy management problem seeks to maximize the action-value function by choosing the optimal policy π^* as [3]:

$$Q^*(s, a) = \max_{\pi} Q^{\pi}(s, a) \quad (5.15)$$

The intermittent and stochastic nature of PV power and uncertainties of the energy market's prices make it challenging to find the optimal policy analytically. A RL-based solution tries to iteratively explore the environment and update the action-value function, $Q^{\pi}(s, a)$, using the following Bellman equation [17]:

$$Q(s_t, a_t) \leftarrow Q(s_t, a_t) + \alpha \left[\left(R_t + \max_a Q(s_{t+1}, a) \cdot \gamma \right) - Q(s_t, a_t) \right] \quad (5.16)$$

As the iterations continue, the action-value function, $Q(s, a)$ converges to the $Q^*(s, a)$. Then, the ε -greedy policy is used to determine the optimal schedule.

$$a^* = \arg \max_{a \in A} Q^*(s, a) \quad (5.17)$$

To explore the environment for a better reward, the agent can randomly select a schedule with probability ε ; otherwise, choose the greedy action with probability $1 - \varepsilon$. In general, in Q-learning, a look-up table is used to approximate $Q^*(s, a)$. However, Q-learning has confronted an extremely large table in the CAES-PV scheduling problem due to the continuous and high-dimensional state spaces; thus, it makes it intractable to update such a large table. DRL is a model-free RL algorithm to approximate $Q^*(s, a)$ using a deep neural network (DNN) with weights θ as a Q-network [100].

$$Q^{\pi}(s, a) \approx Q(s, a; \theta) \quad (5.18)$$

The Q-network is trained by minimizing the mean-squared error loss function between $Q(s, a)$ and the temporal difference (TD) target.

$$\mathcal{L}(\theta) = \mathbb{E} \left[\left(R_t + \max_a Q(s_{t+1}, a_{t+1}; \bar{\theta}) \cdot \gamma - Q(s_t, a_t; \theta) \right)^2 \right] \quad (5.19)$$

It is worth noting that the targets in DRL are based on the network's weights and biases compared to supervised learning, which considers fixed targets. Therefore, by differentiating (5.19) with respect to θ , Q-learning gradient can be written as follows.

$$\Delta_{\theta}\mathcal{L}(\theta) = \mathbb{E} \left[\left(R_t + \max_a Q(s_{t+1}, a_{t+1}; \theta) \cdot \gamma - Q(s_t, a_t; \theta) \right) \Delta_{\theta}Q(s_t, a_t; \theta) \right] \quad (5.20)$$

Usually, to reduce the computational cost of the loss function optimization, it is expedient to use stochastic gradient descent (SGD) algorithms instead of using the full expectations of the gradient. However, deep Q-learning methods suffer from the oscillation or divergence problem because of updating the parameters based on highly correlated consecutive transitions. In this study, the experience replay mechanism is used to break the temporally correlated transitions and alleviate this limitation [103, 139]. Furthermore, this process can provide a more stable training process for minibatch optimization algorithms [91]. More specifically, when the transitions are stored in the experience replay, one can achieve much higher data efficiency by reusing the samples.

5.3 Case Study and Numerical Results

The intention of the proposed methodology is to schedule and operate a PV farm and CAES facility together to work as a hybrid power plant to participate in the energy market. For numerical simulation and comparison purposes, the offered framework is applied to a PV farm with a maximum power of 50 MW. The CAES facility with 100/60 MW of discharging/charging power and 9.48 Mkg air mass of cavern capacity. CAES facility characteristics such as energy ratio, heat rate, and VOM of compressor and expander are taken from [126]. The natural gas price is considered to be 3.5\$/GJ. In this case study, the charging/discharging AFR and the heat rate curves provided in Section II are employed to obtain a more realistic view of the thermodynamic characteristics of the facility.

The Solar Radiation Research Laboratory (SRRL) dataset of the National

Renewable Energy Laboratory (NREL), as the largest publicly available dataset, located in Colorado (latitude = 39.74° North, longitude = 105.18° West, elevation = 1,828.8m) is used in the case study [132]. To avoid the obstacle presence and hazy sky, the original images are circularly cropped by a 256×256 binary mask. Both the numerical data and sky images are normalized using the maximum values before being used by the proposed hybrid framework. The dataset of the training process includes six years of images and numerical data (from 2015-01-01 to 2020-12-31 with 1-hour intervals) to reduce the overfitting risk and ensure a stable training process. The first four years' datasets are applied as the training set, while the last two years' datasets are used for validation and testing. It is worth noting that all the meaningless zero and negative GHIs in the dataset, which occurred in the early morning and late night are discarded. The overall structure of the CNN is composed of six layers, including three convolution layers, three pooling layers, and a flattening layer. The BLSTM network consists of three main hidden layers with 350, 350, and 150 units. The CNN-BLSTM framework acts as a representation network; thus, its output is concatenated with the CAES SoC and fed into the Q network. To verify the validation performance of the CNN-BLSTM network, the solar irradiance forecasting task is repeated with various structures. The cross-validation results of some typical CNN-BLSTM structures with a different number of layers and blocks are given in Table [5.1]. From the forecast results, the impacts of different structure combinations can be obtained. Increasing or decreasing the number of layers in both CNN and BLSTM networks significantly reduces the forecasting performance according to the indices.

The Q network is a fully connected neural network with two layers of hidden neurons and rectifier linear units (ReLU) as the activation functions to a uniformly approximate continuous function. The optimal number of neurons for Q networks is 75 and 150 in each hidden layer, respectively. Algorithm [1] shows how to train a DQN agent based on the proposed framework. The

Algorithm 1: Deep Q-Learning for the proposed CAES-PV systems scheduling problem.

Input: CAES SoC, current & forecasted electricity prices, current & forecasted PV power.

Output: DQN for P_t decision making.

Initialize hyper-parameters.

Initialize DNN with random parameters θ .

Initialize the experience replay buffer M .

for $i \in \{\text{number of episodes}\}$ **do**

- Obtain the initial state space s_t .
- Forecast the PV power generation and electricity price by CNN-BLSTM framework
- for** $t \in \{\text{number of time slots}\}$ **do**

 - Select schedule a_t for CAES-PV based on ε -greedy search.
 - Execute schedule action a_t in emulator and observe immediate reward R_t .
 - Process to the new state s_{t+1} .
 - Store the transition (s_t, a_t, R_t, s_{t+1}) into M .
 - $k \leftarrow k + 1$;
 - if** $|M| \geq \text{batch_size}$ **then**

 - Sample random minibatch of transitions from M :
 - $\mathfrak{F} = \{(s_j, a_j, R_j, s_{j+1})\}_{j=1}^{\neq \mathfrak{F}}$.
 - Estimate the target:
 - $y_j = R_j + \gamma Q\left(s_{j+1}, \arg \max_{a'} Q(s_{j+1}, a'; \theta); \bar{\theta}\right)$.
 - Perform a gradient descent with loss:
 - $L(\theta) = \sum_{j=1}^{\neq \mathfrak{F}} [y_j - Q(s_t, a_t; \theta)]^2$.
 - Update parameters: $\theta_{t+1} = \theta_t - \eta \nabla_{\theta_t} L(\theta_t)$.
 - $\varepsilon \leftarrow \varepsilon \times \varepsilon^{\text{decay}}$

 - end if**

- end for**

end for

Table 5.1: Cross-Validation results of the proposed solar irradiance forecasting model with some typical BLSTM-CNN structures.

Network Structure	RMSE (W/m2)	MAPE (%)	MAE (W/m2)
[150 100]+2*Conv.	116.27	13.33	80.54
[250 250]+3*Conv.	88.16	9.64	59.62
[250 250 50]+2*Conv.	97.42	11.83	66.65
[350 350 150]+3*Conv.	80.02	7.64	51.95
[350 350 150]+4*Conv.	82.49	8.24	53.11
[400 400 150]+4*Conv.	84.06	8.27	54.25

network is trained using the Adam optimizer with a learning rate of 0.001. The action selection procedure is determined by the ε -greedy policy for allowing the DRL agent to jump out of locally optimal situations. The replay memory breaks undesired temporal correlation and speeds up the learning process by enabling learning from earlier memories. The charging/discharging action spaces are designed as suggested in [17] with the a step size of 0.2. The discount rate and mini-batch size are chosen to be 0.9 and 64, respectively. The policy is trained over 200 episodes. The training process takes about three hours on a workstation with a Core i7 processor running at 3.2 GHz, 32 GB of RAM, and GeForce GTX 1070 NVIDIA GPU. The code is implemented on the Keras library and TensorFlow as the backend. After the training process, it takes about 3 ms for the proposed strategy to output the control actions for the CAES-PV self-scheduling problem.

5.3.1 Performance Evaluation of Solar Irradiance Forecasting Model

In this study, the root-mean-square error (RMSE), mean absolute percentage error (MAPE), and mean absolute error (MAE) are adopted as three error indices to measure the prediction accuracy [25].

The proposed image-based CNN-BLSTM approach is compared with re-

Table 5.2: Comparison of GHI Forecasting Results.

Forecasting Method		RMSE (W/m ²)	MAPE (%)	MAE (W/m ²)
SARFIMA [117]		202.49	41.57	169.88
UC-M3 [40]		172.73	24.58	124.28
MTS-ESN [154]		156.96	21.62	112.09
LSTM- Choquet [2]		144.64	19.61	102.31
PCA-KNN [144]		125.83	17.89	82.04
RSAM [128]		121.85	16.22	81.96
K-means-CNN [171]		107.33	13.72	73.46
Proposed (CNN+BLSTM)	80.02	7.64	51.95	

cently proposed models for solar irradiance forecasting, including SARFIMA [117], UC-M3 [40], MTS-ESN [154], LSTM- Choquet [2], PCA-KNN [144], RSAM [128], and K-means-CNN [171]. The procedure of choosing the hyper-parameters for the benchmark models is similar to that of the proposed 2D-CNN-BLSTM approach [30]. Table 6.1 demonstrates the average test RMSE, MAPE, and MAE for GHI forecasting. This table clearly shows that the proposed hybrid 2D-CNN-BLSTM model has the lowest error range and the best performance. According to the results, the 2D-CNN-BLSTM has 25.45% RMSE and 29.28% MAE improvements over the benchmark with the best performance, K-means-CNN. These improvements are further increased to 53.67% and 58.2% for the RMSE and MAE results, respectively, when K-means-CNN is replaced by UC-M3 model. The more precise prediction performance shows the better generalization capability of the proposed model.

Figure 5.3 compares the GHI forecasting performance of the proposed model with other benchmark frameworks for a typical day with clear sky, partially cloudy, and cloudy conditions. By comparing 2D-CNN-BLSTM with others in different hours, one can see that the proposed approach outperforms all of the benchmark methods. For such a challenging day, the proposed deep 2D-

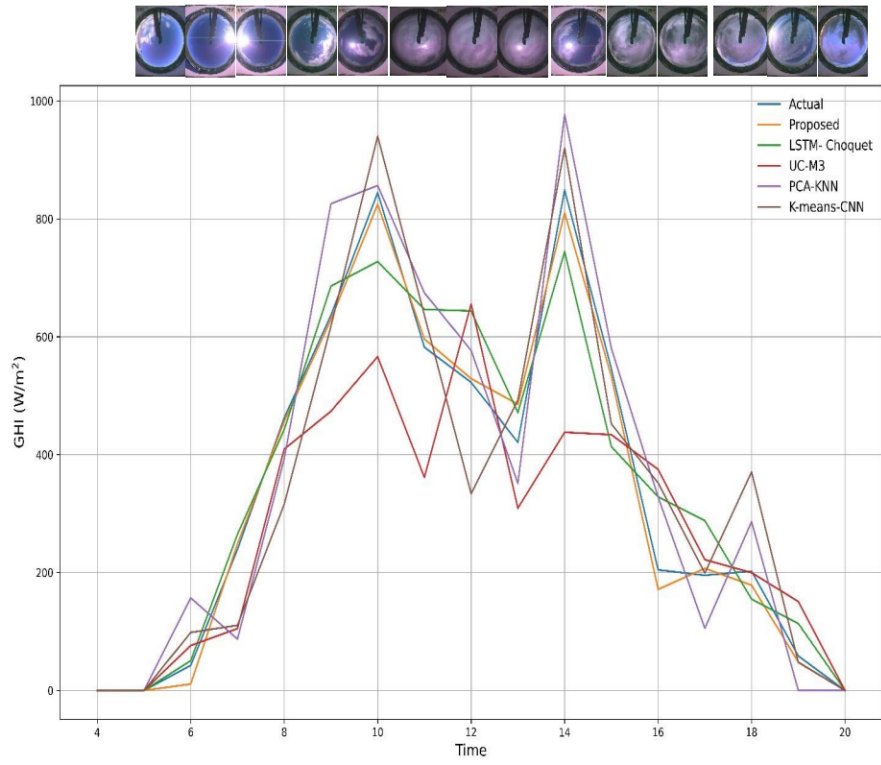


Figure 5.3: Comparison of forecasting results for a typical day with clear sky, partially cloudy, and cloudy conditions (i.e., 2019-05-27).

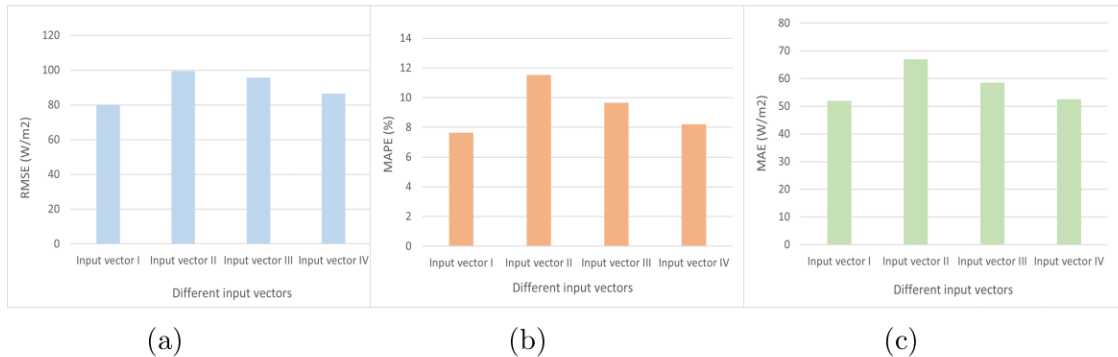


Figure 5.4: Comparison of forecasting errors for different input vectors: a) RMSE, b) MAPE, c) MAE.

CNN-BLSTM approach significantly shows better generalization capability and can follow the sharp spikes accurately. Moreover, the higher accuracy of the proposed model indicates the capability of the image-based model to capture complex data abstractions.

5.3.2 Effects of Weather Parameters in Solar Irradiance Forecasting

In this subsection, the impacts of the key weather factors on the solar forecasting task are evaluated. The forecast performance test is conducted by eliminating each of the key weather factors and quantifying their contributions. Figure 5.4 shows the forecast errors for four different cases with different input vectors as follows:

1. Input vector I: considering all of the numerical meteorological features.
2. Input vector II: input vector I without ambient temperature.
3. Input vector III: input vector I without wind speed
4. Input vector IV: input vector I without relative humidity.

As shown in this figure, after eliminating each key weather factor, the forecasting error indices are increased. As one can observe, the ambient temperature components greatly influence the forecasting results and ignoring them increases RMSE by 27.38%, MAPE by 50.91%, and MAE by 29.02%. Moreover, wind speed and relative humidity are two other significant factors that can improve the forecast performance. For example, by eliminating wind speed and relative humidity the RMSE of 80.02 W/m² reaches to 95.77 W/m² and 86.41 W/m², respectively. The results verify that the input weather features have significant contributions and impacts on the forecasting performance and cannot be ignored.

5.3.3 CAES-PV Self-Scheduling Problem

The performance of the proposed model is evaluated using the following scenarios:

1. Scheduling of the CAES-PV system with model-based step function approach proposed in [126].
2. Scheduling of the CAES-PV system with model-based linear AA method presented in [24].
3. Scheduling of the CAES-PV system with DRL model.
4. Scheduling of the CAES-PV system with the proposed DRL+2D-CNN-BLSTM framework.

After the training procedure and obtaining the optimal network parameters, the DQN agent is employed to make optimal scheduling decisions for the CAES-PV facility using the information provided by the proposed 2D-CNN-BLSTM model over the test period.

Figure 5.5 shows the comparison results over the first five days of June 2019, with a challenging solar irradiance profile. The charging/discharging actions are illustrated with magenta bars, the SoC, the electricity prices, and the PV output are illustrated with the blue, red, and yellow lines, respectively. As clearly evidenced by Figure 5.5, though the proposed DRL+2D-CNN-BLSTM approach keeps the SoC inside the min/max range, it can achieve the optimized charging/discharging strategy, even during cloudy hours with a highly uneven PV output profile. The model-based techniques, step function and linear AA, cannot efficiently signal the system to utilize both price variations and storage-renewable cooperation by optimizing the charging/discharging strategy and absorbing PV power during peak hours. As shown in Figure 5.5, both model-free methods can control the system appropriately according to price variations. However, DRL without a forecasting engine can not efficiently learn the optimized strategy. The proposed method (DRL+2D-CNN-BLSTM)

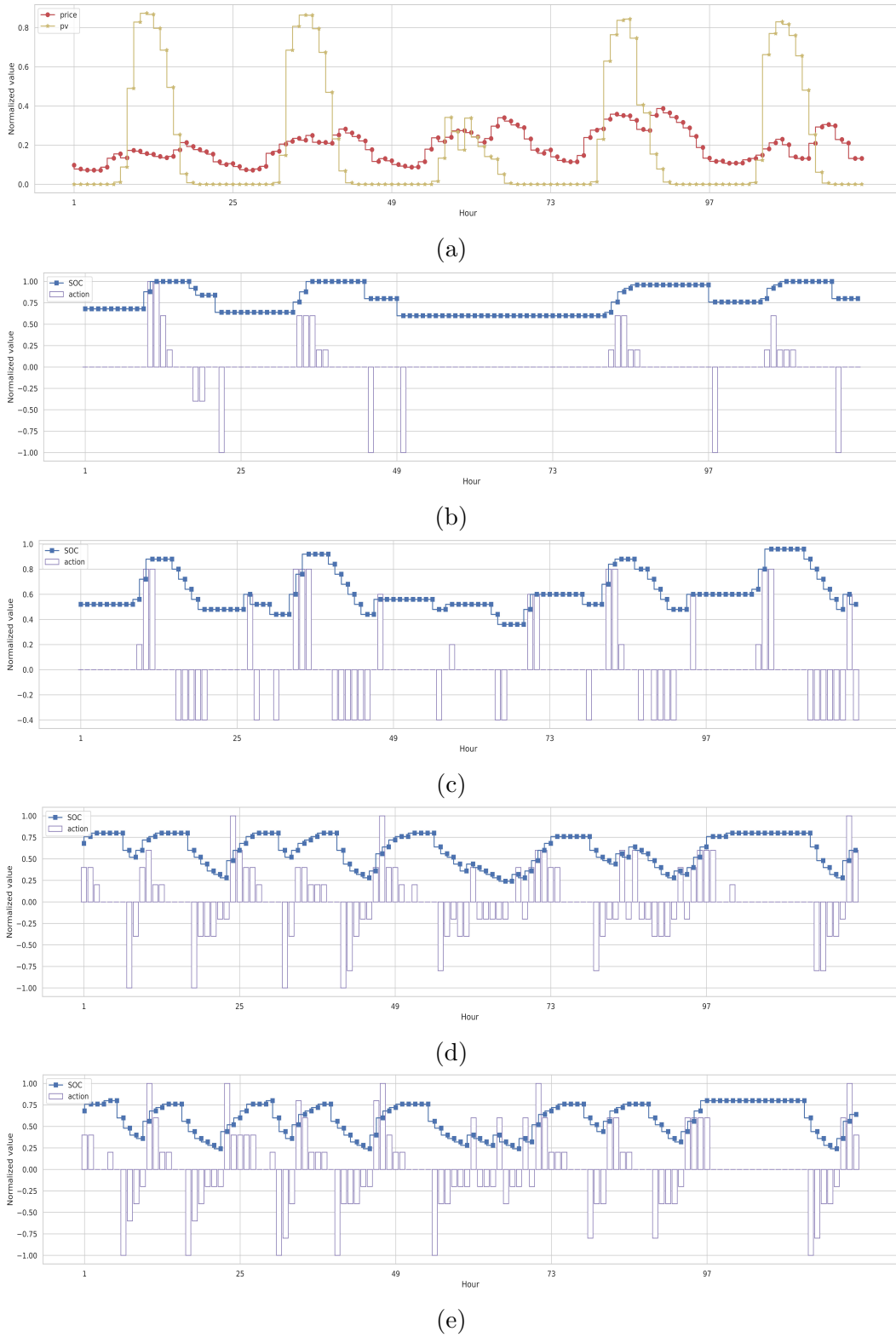


Figure 5.5: The comparison of self-scheduling results for a typical period 2019-06-01 to 2019-06-05 (a) PV and price profiles, (b) model-based step function [126], (c) model-based linear AA [24], (d) DRL, (e) DRL+2D-CNN-BLSTM.

outperforms the DRL and can make more accurate decisions regarding PV output. Moreover, it has more energy interactions with the grid, which bringing a broader SoC control range compared to the model-based ones. It should be noted that the main reason for the proposed model's better performance and generalization capability lies in the fact that these are conditioned to provide an accurate preview of uncertain parameters for DQN agent by the forecasting engine. Overall, this finding can verify the superiority of the proposed mode-free DRL method in controlling the CAES-PV facility.

5.3.4 Effects of Uncertainty Resources

In this section, the performance of DRL+2D-CNN-BLSTM is compared with model-based step function and model-based linear AA in the face of PV power and energy price uncertainties. Moreover, a DRL-based hypothetical full-knowledge model is considered the benchmark for better evaluation of other techniques. In this mode, it is assumed that all information about the uncertain parameters (PV generation and energy price) in future hours is available for the operator. Table 7.3 compares the average scheduling profit and running time of the four scheduling models. This table clearly shows that the proposed framework (DRL+2D-CNN-BLSTM) outperforms the other model-based approaches and has the best performance in terms of revenue and computational costs. DRL+2D-CNN-BLSTM has a \$38,586 per day average profit for the year 2019, which shows a 46.17% improvement over the linear AA model. This improvement is further increased to 56.74% for the step function approach. Furthermore, the results show a huge difference between model-free and model-based approaches in terms of running time. The proposed DRL+2D-CNN-BLSTM model has almost zero running time compared to 4-6 minutes running time of the model-based approaches.

Table 5.3: CAES-PV Scheduling Results For the Year 2019.

Scheduling Method	Average Profit (\$/day)	Profit Change	Max. Computing Time
Step function [126]	24,617	-41.43%	5min 48s
Linear AA [24]	26,398	-37.19%	4min 11s
DRL+2D-CNN-BLSTM	38,586	-8.21%	0.003s
Full-knowledge	42,035	0%	0.002s

5.4 Conclusion

This study develops a comprehensive economic assessment model for a CAES-PV facility participating in the energy market based on the DRL framework. Due to the nonconvex nature and highly intermittent parameters involved in the scheduling problem, the DQN agent is introduced to perform the optimal self-scheduling of the CAES-PV system incorporating the thermodynamic characteristics of the system. To address the uncertainties of electricity price and PV power output, especially during cloudy days, a novel hybrid 2D-CNN-BLSTM model is adopted to predict the price and solar irradiance more accurately. Case Studies using real-world data have demonstrated that a well-trained DQN agent can provide high profitability by making optimal dynamic decisions, making the proposed approach meaningful to the smart energy system industry.

Chapter 6

A Novel Model-Free Deep Reinforcement Learning Framework for Energy Management of a PV-Integrated Energy Hub

In this chapter, a fully model-free and data-driven DRL framework is utilized to develop an intelligent controller that can exploit information to optimally schedule the energy hub with the aim of minimizing energy costs and emissions. In this study, to operate an energy hub in the most cost-effective way while dealing with operational constraints of interacted energy infrastructures, three main challenges have to be addressed. (1) Most studies related to energy hub systems adopt conventional optimization methods, such as SP or RO [30, 32, 59]. Generally, these techniques require detailed and perfect knowledge of the system's parameters and operational model, resulting in high dependencies of decision-making on the accuracy of the employed system model and expert knowledge, which is very costly and challenging. (2) Till now, in the energy hub operation area, most scheduling methods employ piecewise linearization modeling for the system units, such as CHP, distributed generation (DG), and fuel cell. However, this assumption creates some errors in the scheduling results, and consequently, the obtained solution cannot be

optimal for the practical operations of the energy hub. (3) There is rarely any consideration of a comprehensive forecasting framework for the integration of renewables during the energy hub decision-making process, which could cause considerable challenges to the stability and security of the energy hub system.

To bridge this gap, this study proposes a novel model-free DRL framework for energy management of a PV-integrated energy hub incorporating the non-linear characteristics of the CHP, DG, and fuel cell units simultaneously. As a result, the optimal control policy can be gradually learned by the agent of the DDPG framework with no prior knowledge of the energy hub system. The agent repeatedly interacts with the environment and acquires experiences to learn how to decide optimal decisions without modeling the constraint sets of uncertainties or probability distributions. To obtain decent scheduling results, a novel DNN-based BLSTM and 2-D CNNs forecasting framework is incorporated with DDPG. The time series of different meteorological components and sky images are employed and handled by the BLSTM and CNN networks, respectively, to learn complex features.

This Chapter is organized as follows: Section [6.1] describes the proposed DDPG framework for the energy hub system and deep-learning-based hybrid 2-D CNN-BLSTM forecasting model with sky images. Then, Section [6.2] provides the nonlinear physical characteristics of the energy hub environment. The case studies used to assess the effectiveness of the proposed controller are presented in Section [6.3]. Finally, Section [6.4] concludes this study.

6.1 Deep Reinforcement Learning (DRL) and Forecasting Framework

In this Section, the main concepts of DDPG as an actor-critic DRL model is presented. The deep-learning-based hybrid 2-D CNN-BLSTM model for solar irradiance prediction using sky images is presented next.

6.1.1 Deep Deterministic Policy Gradient (DDPG)

In this study, the DDPG is adopted as an actor-critic DRL algorithm to find the optimal control strategy of the PV-integrated energy hub. By avoiding the computationally costly discretization process and providing continuous action spaces, DDPG can explore the action space more effectively. Consequently, the optimal solution can be obtained in various problem sets while requiring fewer iterations than other techniques. Moreover, the generation infrastructures of the energy hub can be regulated more smoothly as opposed to simply acting on simple discrete levels.

During making decisions in each system state, DDPG uses Q-value, $Q(s_t, a_t)$, to determine the most beneficial strategy by estimating the value of choosing a decision over the long-term, $a_t \in \mathcal{A}_t$. As a result of the Bellman equation, by using the Q-value of the most beneficial action at state s_{t+1} and the immediate reward, the Q-value of any action, a_t , at state s_t can be determined as follows.

$$Q(s_t, a_t) = \gamma \mathbb{E} \left[\max_{a_{t+1} \in \mathcal{A}_{t+1}} Q(s_{t+1}, a_{t+1}) \right] + \mathcal{R}(s_t, a_t) \quad (6.1)$$

where \mathcal{R} is the reward function, and the parameter $\gamma \in [0, 1]$ is the discount factor for balancing between the immediate reward and future reward. On the other hand, the energy hub operator has no information regarding both the most beneficial action at state s_{t+1} and its actual value over the long-term period. To address this issue, two separate DNNs are designed and employed in the DDPG method. $\mu(s_t | \theta^\mu)$ is the actor network that estimates the most beneficial action at state s_{t+1} whereas the Q-value of action a_t at state s_t is estimated by the critic network $Q(s_t, a_t | \theta^Q)$. For each time step during the training process, the weight vectors of actor network, θ^μ , and critic network, θ^Q , are continuously updated according to the observed reward. Then, the Q-value can be formulated using the trained networks as below:

$$Q(s_t, a_t) \approx \gamma \mathbb{E} [Q(s_{t+1}, \mu(s_{t+1} | \theta^\mu) | \theta^Q)] + \mathcal{R}(s_t, a_t) \quad (6.2)$$

The actor network takes actions based on the sampled states of the system. Then, based on the observed reward, the two networks can be trained in parallel. The samples of (s_t, a_t) , where $a_t = \mu(s_t | \theta^\mu)$, and \mathcal{R}_t are used as the input and the output for the training of the critic network, respectively, while the actor network takes s_t and $\max_a Q(s_t, a_t | \theta^Q)$ as the input and the output, respectively. To reduce correlation-induced errors, the samples of different time steps, $(s_t, a_t, \mathcal{R}_t, s_{t+1})$, form the replay buffer. Thus, the critic and actor networks can be continuously updated using the past experiences stored in this circular buffer. To achieve a more stable training procedure, target networks, which are the copies of the original critic and actor networks, are considered. The weights of these target networks are gradually updated for stabilizing Q-value estimation. Furthermore, to improve the exploration process during the training, a correlated stochastic-based noise signal is added to the actor network. The Ornstein-Uhlenbeck process is used in this study to model this noise signal, Ω , as follows [49].

$$\Omega_t = \Omega_{t-1} + \Omega_\sigma n \sqrt{T_s} + (\Omega_{mean} - \Omega_{t-1}) \kappa T_s \quad (6.3)$$

where Ω_{mean} and Ω_σ are the mean value and the variance of the noise model, respectively. $n \in [0, 1]$ and κ represent a uniformly generated random number and the mean attraction constant, respectively. This perturbation increases the exploration ability of the DDPG agent and, thus, results in faster convergence.

The loss function $\mathcal{L}(\theta^Q)$ is defined as given in equation (7.36) to train the critic network.

$$\mathcal{L}(\theta^Q) = \frac{1}{N} \sum_{i \in N} [Q(s_i, \mu(s_i | \theta^\mu) | \theta^Q) - \mathcal{Y}_i]^2 \quad (6.4)$$

where N denotes the mini-batch size, and \mathcal{Y}_i , which is the measured value function, is described by (7.37):

$$\mathcal{Y}_i = Q\left(s_{t+1}, \mu\left(s_{t+1} | \theta^{\mu'}\right) | \theta^{Q'}\right) + \mathcal{R}(s_t, a_t) \quad (6.5)$$

Then, the parameters of the critic network, θ^Q , can be updated by minimizing \mathcal{L} across the experiences sampled. To train the actor network, on the other, the following gradient needs to be obtained:

$$\nabla_{\theta^\mu} \mathcal{L}(\theta^\mu) = \frac{1}{N} \sum_{i \in N} \nabla_a Q(s_i, \mu(s_i | \theta^\mu) | \theta^Q) \nabla_{\theta^\mu} \mu(s_i | \theta^\mu) \quad (6.6)$$

where $a_i = \mu(s_i | \theta^\mu)$. Finally, the target networks are gradually updated by (7.39) and (7.40).

$$\theta^{Q'} = \tau \theta^Q + (1 - \tau) \theta^{Q'} \quad (6.7)$$

$$\theta^{\mu'} = \tau \theta^\mu + (1 - \tau) \theta^{\mu'} \quad (6.8)$$

where τ is the smoothing factor.

6.1.2 Deep Hybrid 2-D CNN-BLSTM Forecasting Model

In recent years, solar forecasting has gained increasing attention due to an aggressive increase in PV generation entering power and energy markets. Solar irradiance plays an important role in the forecast of solar power generation, and meteorological and atmospheric conditions greatly influence it. As a result, a comprehensive model for solar irradiance prediction based on sky images can improve the solar irradiance significantly. In this study, as shown in Figure 6.1, a hybrid framework for solar irradiance prediction is proposed. It utilizes deep CNN and BLSTM networks to analyze high-resolution sky images with multiple meteorological time series data that are processed by deep CNN and BLSTM networks, respectively. The proposed framework can effectively capture complex solar data abstractions by incorporating numerical meteorological features such as global horizontal irradiance (GHI), wind speed, relative humidity, temperature, atmospheric pressure, and the calendar features, i.e., the hour of the day and month of the year into the input vector. The details of deep CNN and BLSTM networks can be found in [25, 26], including the mathematical representation of the layers used for the proposed hybrid framework.

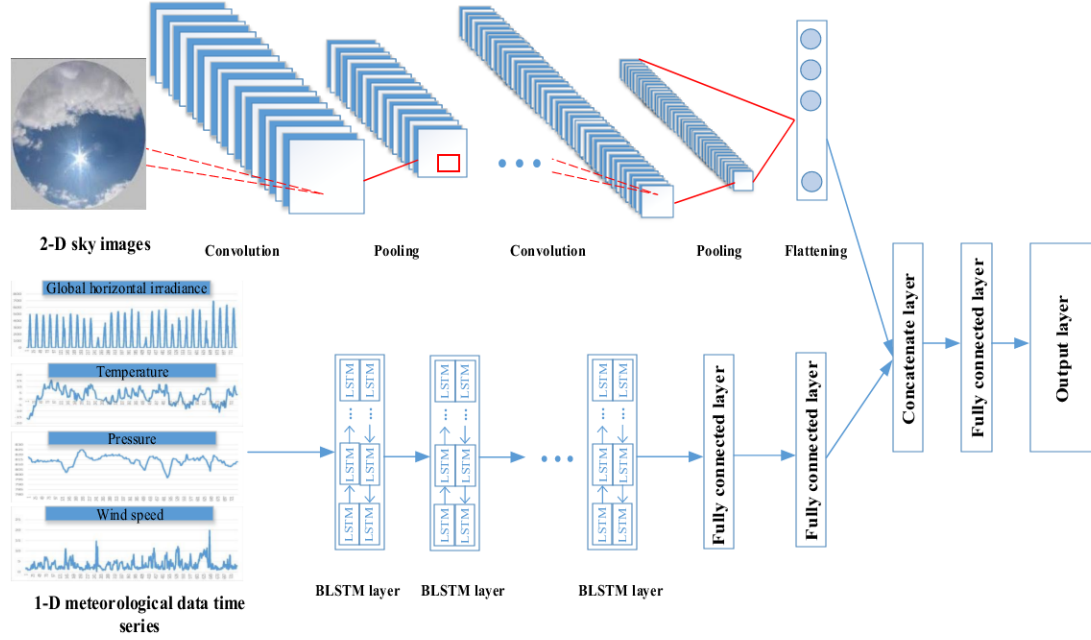


Figure 6.1: Overview of the proposed 2-D CNN-BLSTM prediction framework.

6.2 Environment Model

This Section presents the structure of the proposed PV-integrated energy hub, where nonlinear physical characteristics of the facility components like non-convex feasible operating regions of combined heat and power (CHP) units, valve-point effects of power-only units, and fuel cell dynamic efficiency are taken into account.

6.2.1 CHP Units Modeling

It is worth noting that the generated heat and power of CHP units are mutually interdependent and therefore cannot be controlled independently. In general, as shown in Figure [6.2], there are two types of CHP units with different feasible operating regions (FORs). The first type of CHP can be modeled

by (7.10)-(6.13) [4].

$$P_{j,t}^{chp} - P_{j,A}^{chp} - \frac{P_{j,A}^{chp} - P_{j,B}^{chp}}{H_{j,A}^{chp} - H_{j,B}^{chp}} \times (H_{j,t}^{chp} - H_{j,A}^{chp}) \leq 0 \quad (6.9)$$

$$-\left(1 - I_{j,t}^{CHP}\right) \times \Gamma \leq P_{j,t}^{chp} - P_{j,B}^{chp} \\ - \frac{P_{j,B}^{chp} - P_{j,C}^{chp}}{H_{j,B}^{chp} - H_{j,C}^{chp}} \times (H_{j,t}^{chp} - H_{j,B}^{chp}) \quad (6.10)$$

$$-\left(1 - I_{j,t}^{CHP}\right) \times \Gamma \leq P_{j,t}^{chp} - P_{j,C}^{chp} \\ - \frac{P_{j,C}^{chp} - P_{j,D}^{chp}}{H_{j,C}^{chp} - H_{j,D}^{chp}} \times (H_{j,t}^{chp} - H_{j,C}^{chp}) \quad (6.11)$$

$$0 \leq P_{j,t}^{chp} \leq P_{j,A}^{chp} \times I_{j,t}^{CHP} \quad (6.12)$$

$$0 \leq H_{j,t}^{chp} \leq H_{j,B}^{chp} \times I_{j,t}^{CHP} \quad (6.13)$$

where $P_{j,t}^{chp}$ and $H_{j,t}^{chp}$ are the generated power and heat of the j^{th} CHP unit at time t , respectively. The four marginal points of the FOR of type one are represented by A, B, C , and D . Γ and I^{chp} denote a sufficiently large number and commitment status, respectively. As can be seen from Figure 6.2(b), the non-convex FOR of type two, enclosed by the boundary curve $ABCDEFG$, can be represented by two convex subregions I and II as (6.14)-(6.21) [4].

$$P_{j,t}^{chp} - P_{j,B}^{chp} - \frac{P_{j,B}^{chp} - P_{j,C}^{chp}}{H_{j,B}^{chp} - H_{j,C}^{chp}} \times (H_{j,t}^{chp} - H_{j,B}^{chp}) \leq 0 \quad (6.14)$$

$$P_{j,t}^{chp} - P_{j,C}^{chp} - \frac{P_{j,C}^{chp} - P_{j,D}^{chp}}{H_{j,C}^{chp} - H_{j,D}^{chp}} \times (H_{j,t}^{chp} - H_{j,C}^{chp}) \geq 0 \quad (6.15)$$

$$-\left(1 - \bar{\chi}_{j,t}^{CHP}\right) \times \Gamma \leq P_{j,t}^{chp} - P_{j,E}^{chp} \\ - \frac{P_{j,E}^{chp} - P_{j,F}^{chp}}{H_{j,E}^{chp} - H_{j,F}^{chp}} \times (H_{j,t}^{chp} - H_{j,E}^{chp}) \quad (6.16)$$

$$-\left(1 - \underline{\chi}_{j,t}^{CHP}\right) \times \Gamma \leq P_{j,t}^{chp} - P_{j,D}^{chp} \\ - \frac{P_{j,D}^{chp} - P_{j,E}^{chp}}{H_{j,D}^{chp} - H_{j,E}^{chp}} \times (H_{j,t}^{chp} - H_{j,D}^{chp}) \quad (6.17)$$

$$\bar{\chi}_{j,t}^{CHP} + \underline{\chi}_{j,t}^{CHP} = I_{j,t}^{CHP} \quad (6.18)$$

$$-\left(1 - \underline{\chi}_{j,t}^{CHP}\right) \times \Gamma \leq H_{j,t}^{chp} - H_{j,E}^{chp} \leq \left(1 - \bar{\chi}_{j,t}^{CHP}\right) \times \Gamma \quad (6.19)$$

$$0 \leq P_{j,t}^{chp} \leq P_{j,A}^{chp} \times I_{j,t}^{CHP} \quad (6.20)$$

$$0 \leq H_{j,t}^{chp} \leq H_{j,A}^{chp} \times I_{j,t}^{CHP} \quad (6.21)$$

where $\bar{\chi}$ ($\underline{\chi}$) states the operating status in the first (second) convex section. The total operation cost of the j^{th} CHP unit at time t can be expressed by equation (6.22).

$$\begin{aligned} C_{j,t}^{chp} \left(P_{j,t}^{chp}, H_{j,t}^{chp} \right) &= \bar{\alpha}_j^{chp} \cdot P_{j,t}^{chp^2} + \bar{\beta}_j^{chp} \cdot P_{j,t}^{chp} + \bar{\gamma}_j^{chp} \\ &\quad + \underline{\alpha}_j^{chp} \cdot H_{j,t}^{chp^2} + \underline{\beta}_j^{chp} \cdot H_{j,t}^{chp} + \underline{\gamma}_j^{chp} \cdot H_{j,t}^{chp} \cdot P_{j,t}^{chp} \end{aligned} \quad (6.22)$$

where $\bar{\alpha}_j/\underline{\alpha}_j$, $\bar{\beta}_j/\underline{\beta}_j$, $\bar{\gamma}_j/\underline{\gamma}_j$ represent the cost coefficients of the j^{th} CHP unit.

6.2.2 Power-Only Units Modeling

In most of the literature, convex quadratic cost functions have been employed to model the costs of power-only generation units [34,44,83]. However, these models ignore the ripple in the production cost caused by the valve admission effects; thus, they cannot obtain the optimal solution in the practical operation of the system. In this work, an absolute sinusoidal term is incorporated into the quadratic cost function to model this effect more accurately. Figure 7.2 illustrates the fuel cost of the power-only unit considering valve-point effects.

The total operation cost

$$C_{i,t}^c \left(P_{i,t}^c \right) = \alpha_i^c \cdot (P_{i,t}^c)^2 + \beta_i^c \cdot P_{i,t}^c + \gamma_i^c + VPE_{i,t}^c \left(P_{i,t}^c \right) \quad (6.23)$$

$$VPE_{i,t}^c \left(P_{i,t}^c \right) = \left| \lambda_i^c \sin \left(\rho_i^c \left(P_{i,\min}^c - P_{i,t}^c \right) \right) \right| \quad (6.24)$$

$$P_{i,\min}^c \times I_{i,t}^c \leq P_{i,t}^c \leq P_{i,\max}^c \times I_{i,t}^c \quad (6.25)$$

where α_i^c , β_i^c , γ_i^c , λ_i^c , and ρ_i^c are the cost coefficients of the i^{th} power-only unit.

VPE^c and I^c denote the valve-point effects and commitment status.

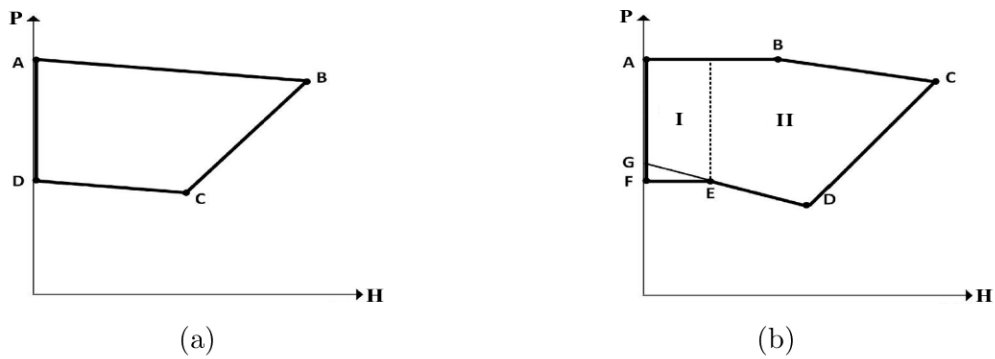


Figure 6.2: CHP units' power-heat feasible region: a) Type 1, b) Type 2.

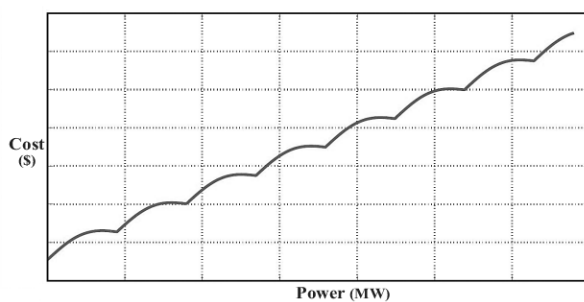


Figure 6.3: Power-only units' valve-point effects.

6.2.3 Heat-Only Units Modeling

The operational cost and the capacity limits of k^{th} heat-only unit at time t are expressed by (7.7) and (7.8).

$$C_{k,t}^b (H_{k,t}^b) = \alpha_k^b \times (H_{k,t}^b)^2 + \beta_k^b \times H_{k,t}^b + \gamma_k^b \quad (6.26)$$

$$H_{k,\min}^b \times I_{k,t}^b \leq H_{k,t}^b \leq H_{k,\max}^b \times I_{k,t}^b \quad (6.27)$$

where α_k^b , β_k^b , and γ_k^b represent the cost coefficients of the k^{th} heat-only unit, and I^b state the commitment status.

6.2.4 Fuel Cell Modeling

In this study, part of the energy hub demand is supplied by the local fuel cell (FC) by providing electricity, recovered heat, and hydrogen production. It is worth noting that hydrogen derived from the reforming of natural gas is the main fuel resource of the system, and the tank containing hydrogen serves as a backup. The electric and hydrogen outputs of the l^{th} FC unit determine the amount of recovered thermal power, $H_{l,t}^{fc}$, as follows:

$$H_{l,t}^{fc} = TER_{l,t}^{fc} \times \left(P_{l,t}^{fc,e} + \underline{P}_{l,t}^{fc,h} \right) \quad (6.28)$$

$$P_{l,t}^{fc,total} = P_{l,t}^{fc,e} + \underline{P}_{l,t}^{fc,h} \quad (6.29)$$

where TER^{fc} , $P^{fc,e}$, and $P^{fc,h}$ are the thermal to electrical power ratio, electrical output power, and equivalent electric power for hydrogen production of FC unit, respectively. FC unit, similar to the other generation units, has limitations for producing, which is satisfied by (7.21).

$$P_{l,\min}^{fc} \times I_{l,t}^{fc} \leq P_{l,t}^{fc,e} + \underline{P}_{l,t}^{fc,h} \leq P_{l,\max}^{fc} \times I_{l,t}^{fc} \quad (6.30)$$

The amount of hydrogen stored in the tank could be calculated by (7.22).

$$H2T_{l,t}^{fc} = H2T_{l,t-1}^{fc} + (\eta_{l,ch}^{H2T} \times H2_{l,t}^{in}) - \left(\frac{H2_{l,t}^{out}}{\eta_{l,dch}^{H2T}} \right) \quad (6.31)$$

The equivalent charged and discharged hydrogen are formulated in (7.23) and (7.24), respectively.

$$H2_{l,t}^{in} = \underline{P}_{l,t}^{fc,h} \times \psi^{P2H} \quad (6.32)$$

$$H2_{l,t}^{out} = \overline{P}_{l,t}^{fc,h} \times \psi^{P2H} \quad (6.33)$$

where ψ^{P2H} is the conversion factor (hydrogen (kg)/electric power(kW)). The amount of hydrogen stored in the tank and the hydrogen charging/discharging rates are limited through (7.25) and (7.26)/(7.27), respectively, and (7.28) guarantees that the hydrogen tank cannot be charged and discharged at the same time.

$$H2T_{l,min}^{fc} \leq H2T_{l,t}^{fc} \leq H2T_{l,max}^{fc} \quad (6.34)$$

$$H2_{l,min}^{in} \times I_{l,t}^{H2T,ch} \leq H2_{l,t}^{in} \leq H2_{l,max}^{in} \times I_{l,t}^{H2T,ch} \quad (6.35)$$

$$H2_{l,min}^{out} \times I_{l,t}^{H2T,dch} \leq H2_{l,t}^{out} \leq H2_{l,max}^{out} \times I_{l,t}^{H2T,dch} \quad (6.36)$$

$$I_{l,t}^{H2T,ch} + I_{l,t}^{H2T,dch} \leq 1 \quad (6.37)$$

A large body of prior research works on FC is considered a constant value for its efficiency, while this value may vary depending on the amount of electrical energy generated. As shown in Figure 7.4, FC efficiency, η_l^{fc} , and thermal to electrical power ratio, TER^{fc} , can be considered as a function of generated electric power to the maximum electric power output ratio, which is expressed as part load ratio variable (ϑ) as follows [38]:

$$\eta_{l,t}^{fc} = \begin{cases} 0.272 & \vartheta_{l,t} \leq 0.05 \\ 0.9033 \times \vartheta_{l,t}^5 - 2.996 \times \vartheta_{l,t}^4 \\ + 3.6503 \times \vartheta_{l,t}^3 - 2.0704 \times \vartheta_{l,t}^2 \\ + 0.4623 \times \vartheta_{l,t} + 0.3747 & \vartheta_{l,t} \geq 0.05 \end{cases} \quad (6.38)$$

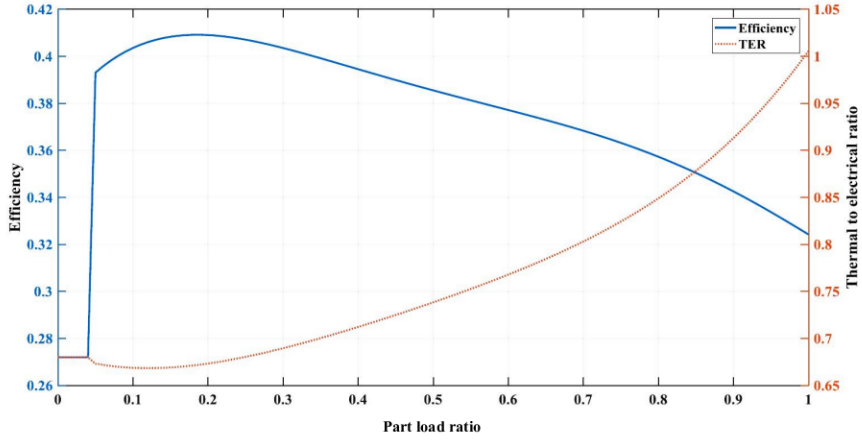


Figure 6.4: Dynamic performance curve of the FC unit.

$$TER_{l,t}^{fc} = \begin{cases} 0.68 & \vartheta_{l,t} \leq 0.05 \\ 1.078 \times \vartheta_{l,t}^4 - 1.974 \times \vartheta_{l,t}^3 + 1.5 \times \vartheta_{l,t}^2 - 0.282 \times \vartheta_{l,t} + 0.6838 & \vartheta_{l,t} \geq 0.05 \end{cases} \quad (6.39)$$

The total operation cost of l^{th} FC unit at time t is given by equation (7.29).

$$C_{l,t}^{fc} \left(P_{l,t}^{fc,e}, P_{l,t}^{fc,h} \right) = \left(\frac{P_{l,t}^{fc,total}}{\eta_{l,t}^{fc}} \times \pi_t^{ng} \right) + \left(C_l^{fc,pump} \times P_{l,t}^{fc,h} \right) + \left(C_l^{fc,OM} \times P_{l,t}^{fc,total} \right) \quad (6.40)$$

6.2.5 Power Balance

Generated and consumed electrical and thermal power at every time instance t should be equal as follows:

$$\sum_{j \in N_{CHP}} P_{j,t}^{chp} + \sum_{i \in N_C} P_{i,t}^c + \sum_{l \in N_{FC}} \left(P_{l,t}^{fc,e} + \bar{P}_{l,t}^{fc,h} \right) = P_t^{bes} + P_t^{pv} + P_t^{grid} = P_t^l \quad (6.41)$$

$$\sum_{j \in N_{CHP}} H_{j,t}^{chp} + \sum_{l \in N_{FC}} H_{l,t}^{fc} + \sum_{k \in N_B} H_{k,t}^b + H_t^{bt} = H_t^l + H_t^{sv} \quad (6.42)$$

where P^{grid} and P^{bes} are the exchanged power with the upstream network and the charging/discharging power, respectively; P^l is the electric load; H^l ,

H^{bt} , and H^{sv} are the thermal load, buffer tank charging/discharging thermal power, and the slack variable [16], respectively. The details of electrical and thermal storages can be found in [31].

6.2.6 Objective Function

The objective function of the energy hub scheduling problem is to minimize the total operation cost and emission functions as follows:

$$OF^{OC} = \sum_{t \in N_T} \left\{ \begin{array}{l} \sum_{i \in N_C} C_{i,t}^c + \sum_{j \in N_{CHP}} C_{j,t}^{chp} + C_t^{grid} \\ + \sum_{l \in N_{FC}} C_{l,t}^{fc} + \sum_{k \in N_B} C_{k,t}^b \end{array} \right\} \quad (6.43)$$

$$OF^{\text{emission}} = \sum_{t \in N_T} \left\{ \begin{array}{l} \sum_{i \in N_C} E_{i,t}^c + \sum_{j \in N_{CHP}} E_{j,t}^{chp} + E_{i,t}^{grid} \\ + \sum_{l \in N_{FC}} E_{l,t}^{fc} + \sum_{k \in N_B} E_{k,t}^b \end{array} \right\} \quad (6.44)$$

$$E_{i,t}^c = (\kappa_{NOx}^c + \kappa_{SO2}^c + \kappa_{CO2}^c) \times P_{i,t}^c \quad (6.45)$$

$$E_{j,t}^{chp} = (\kappa_{NOx}^{chp} + \kappa_{SO2}^{chp} + \kappa_{CO2}^{chp}) \times P_{j,t}^{chp} \quad (6.46)$$

$$E_{i,t}^{grid} = (\kappa_{NOx}^{grid} + \kappa_{SO2}^{grid} + \kappa_{CO2}^{grid}) \times P_{i,t}^{grid} \quad (6.47)$$

$$E_{l,t}^{fc} = (\kappa_{NOx}^{fc} + \kappa_{SO2}^{fc} + \kappa_{CO2}^{fc}) \times P_{l,t}^{fc,total} \quad (6.48)$$

$$E_{k,t}^b = (\kappa_{NOx}^b + \kappa_{SO2}^b + \kappa_{CO2}^b) \times H_{k,t}^b \quad (6.49)$$

where κ_{NOx} , κ_{SO2} , and κ_{CO2} are the emission factors of NOx , $SO2$, and $CO2$, respectively.

6.3 Case Study and Numerical Results

To evaluate the effectiveness of the proposed scheduling approach, the PV-integrated energy hub shown in Figure 6.5 is used as an example for the case

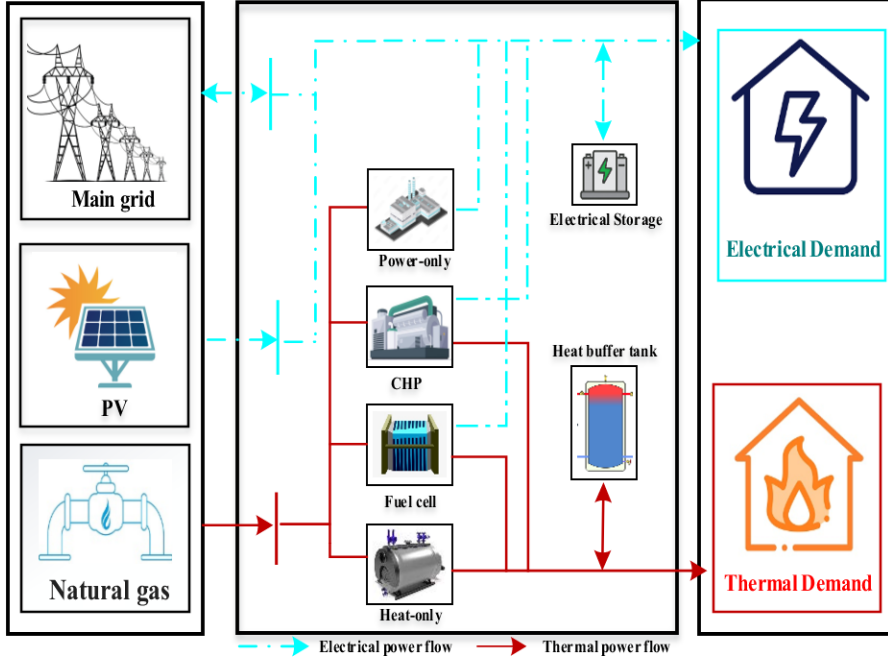


Figure 6.5: Structure of the proposed PV-integrated energy hub.

study. The proposed DRL-based framework seeks to schedule and operate a PV-integrated energy hub facility as a multi-carrier energy system participating in the energy market. The hourly dataset of electrical and thermal demands is adapted from [136]. The data corresponding to the energy prices is extracted from [116]. The operational constraints and economic data of the CHP, power-only and heat-only units are derived and scaled according to the problem requirements from a test case proposed by [11], which is also used in most CHP-related work [106]. The maximum power of PV, power-only, and heat-only units are 0.75 MW, 1.25 MW, and 2.695 MW_{th}, respectively. Moreover, the data of the fuel cell with 1 MW maximum power output and the hydrogen tank are taken from [38]. The numerical values of the emission factors are selected from [107]. The numerical time series data and sky images are both derived from the largest publicly available dataset created by the National Renewable Energy Laboratory (NREL), the solar radiation research laboratory (SRRL), located in Colorado (latitude = 39.74° North, longitude =

105.18° West, elevation =1,828.8m) [133]. Using a 256*256 binary mask, the original images have been circularly cropped to remove the obstacles and hazy sky. Before being put into use by the proposed hybrid forecasting framework, both numerical time series data, as well as sky images, are normalized using maximum values. A one-year period (2017) of meteorological time series and sky images dataset are adopted in the case study. Due to the strong seasonal patterns of solar data and to ensure a stable training process and reduce the overfitting risk, a randomly selected sample of training data is taken from each month, while the remaining samples are considered testing data (there is a 3:1 ratio of training:testing). This data partitioning strategy allows for a better assessment of the model’s generality. It is worth noting that all zeros and negatives in the dataset observed early in the morning or late at night have been discarded.

In the proposed approach, since it is entirely data-dependent, all hyperparameters are optimally tailored using the training data following the recommendations of the deep learning community [48], while on the other hand, the scheme for setting the parameters presented in [140] is referred to. There are six layers in the CNN, including three convolution layers, three pooling layers, and a flattening layer. The BLSTM architecture is composed of three main hidden layers that have 300, 250, and 125 units, respectively. The proposed CNN-BLSTM forecasting framework serves as a representation network, hence its outcome is simply concatenated with the energy hub’s states and then fed into the actor network. The learning rates of the actor and critic networks are 0.0001 and 0.001, respectively. The discount factor and random experience mini-batch size are chosen to be 0.95 and 64, respectively. Both actor and critic networks have two layers of hidden neurons containing 250 and 100 neurons, respectively, that are activated by rectifier linear units (ReLUs). The target networks are updated using a smoothing factor of 0.001. The noise model parameters are selected from [123]. The framework of the proposed DDPG algorithm is shown in Figure 7.5. The DDPG agent’s action vector

corresponds to the energy hub units' decision variables for dynamic dispatch and can be represented by (7.42).

$$a_t = \left\{ P_{j,t}^{chp}, P_{i,t}^c, H_{k,t}^b, P_{l,t}^{fc,e}, P_{l,t}^{fc,h}, P_t^{bes}, H_t^{bt} \right\} \quad (6.50)$$

At the beginning of a day, the DDPG agent receives the current and predicted PV power, energy prices, thermal and electrical storages' status, and thermal and electrical demands from the proposed energy hub environment as follows.

$$s_t = \left\{ P_t^{pv}, \hat{P}_t^{pv}, \pi_t^{ng}, \pi_t^e, SoC_t^{bt}, SoC_t^{bes}, H_t^l, P_t^l \right\} \quad (6.51)$$

Then the agent adjusts the parameters of the DDPG method by calculating the reward as follows:

$$\mathcal{R}(s_t, a_t) = -(OF_t^{OC} + OF_t^{\text{emission}}) \quad (6.52)$$

Algorithm 2 shows how to train a DDPG agent based on the proposed framework. The proposed approach is implemented using the Keras library and TensorFlow as the backend. The training process takes about five hours on a workstation with a Core i7-8700 processor running at 3.2 GHz, 32 GB of RAM, and one NVIDIA GeForce GTX 1070 NVIDIA GPU. The evolution of episodic energy (operation and emission) cost is depicted in Figure 6.6. Since the DDPG agent is merely exploring the environment without an optimized control policy, the episodic cost of the energy hub operation is extremely high during the initial learning phase. As a result, the energy schedule is randomly selected from the action space with the noise. Although the policy continues to be refined as it is updated with more experience, the cost keeps dropping as the learning process continues.

6.3.1 Implementing 2-D CNN-BLSTM Model for Solar Irradiance Forecasting

Three commonly used error metrics are employed in this study to measure the accuracy of the proposed 2-D CNN-BLSTM prediction model: root-mean-

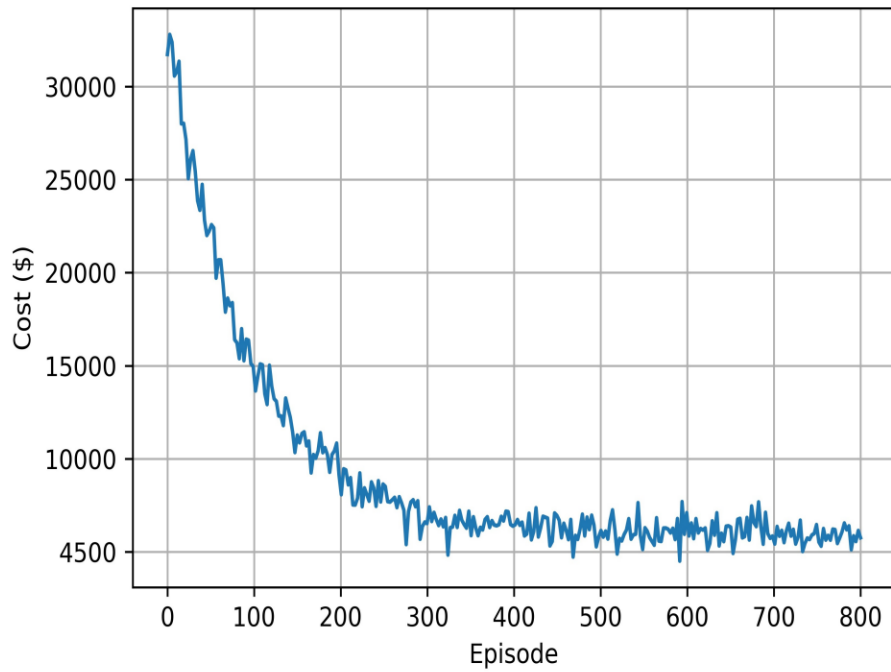


Figure 6.6: The evolution of episodic operational costs associated with the proposed DDPG framework.

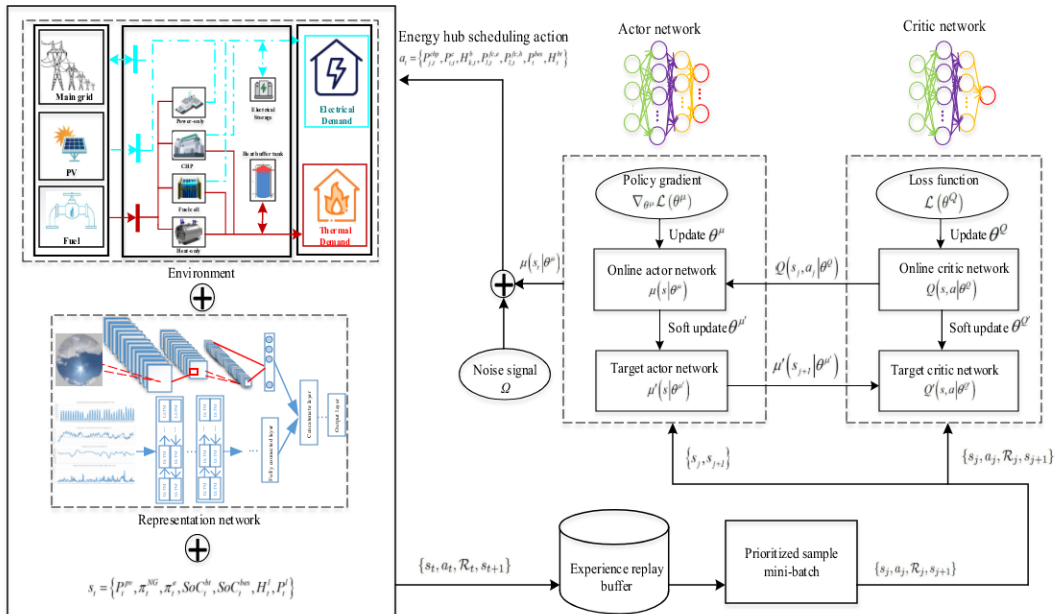


Figure 6.7: The overall architecture of the proposed DDPG+2-D CNN-BLSTM for PV-integrated energy hub scheduling problem.

Algorithm 2: DDPG for the proposed energy hub scheduling problem.

Initialize: Randomly initialize actor and critic networks' weights:
 $\mu(s|\theta^\mu): \theta^\mu = \theta^{\mu_0}$
 $Q(s, a|\theta^Q): \theta^Q = \theta^{Q_0}$

Initialize the experience replay buffer M .

Initialize a random process Ω for action exploration.

for $i \in \{\text{number of episodes}\}$ **do**

- Obtain the initial state space s_t .
- Forecast the PV power generation by the proposed CNN-BLSTM framework
- for** $t \in \{\text{number of time slots}\}$ **do**

 - Select schedule a_t for energy hub based on $a_t = \mu(s_t|\theta^\mu) + \Omega_t$.
 - Execute schedule action a_t and observe immediate reward R_t .
 - Process to the new state s_{t+1} .
 - Store the transition (s_t, a_t, R_t, s_{t+1}) into M .
 - $k \leftarrow k + 1$;
 - if** $|M| \geq \text{batch_size}$ **then**

 - Sample random minibatch of transitions from M :
 - $\mathfrak{F} = \{(s_j, a_j, R_j, s_{j+1})\}_{j=1}^{\#\mathfrak{F}}$.
 - Update the critic network by minimizing the loss using equation (7.36):

$$\theta^Q = \theta^Q + \eta^Q \nabla_{\theta^Q} \mathcal{L}(\theta^Q)$$
 - Update the actor network by the sampled policy gradient using equation (7.38):

$$\theta^\mu = \theta^\mu + \eta^\mu \nabla_{\theta^\mu} \mathcal{L}(\theta^\mu)$$
 - Update the target network using equations (7.39) and (7.40):

$$\theta^{Q'} \leftarrow \theta^Q$$

$$\theta^{\mu'} \leftarrow \theta^\mu$$

 - end if**

- end for**

end for

square error (RMSE), mean absolute error (MAE), and mean absolute percentage error (MAPE) [26].

Table 6.1 provides the average test RMSE, MAE, and MAPE of the proposed 2D CNN-BLSTM framework compared to recently proposed models for solar irradiance forecasting, including UC-M3 [40], LSTM- Choquet [2], PCA-KNN [144], and K-means-CNN [171]. This table clearly indicates the highest level of performance and the lowest error range for the proposed hybrid 2D-CNN-BLSTM model. According to the results, the average RMSE of 2D CNN-BLSTM in this period is 69.44 W/m^2 , while applying LSTM-Choquet and K-means-CNN leads to 98.83 W/m^2 and 109.17 W/m^2 average RMSE, respectively. Compared to the benchmark with the best performance, LSTM-Choquet, significant improvements of 46.51% MAPE and 28.54% MAE are observed for the proposed 2-D CNN-BLSTM framework. Moreover, to provide better visualization, Figs. 6.8 and 6.9 show the hourly forecasting performance for clear, partly cloudy, and cloudy conditions on two typical summer and winter days in the year 2017. For the benchmark models, the process of selecting hyperparameters follows the same procedure as the proposed model. During most of the daytime, except for hours 12 through 14, the solar irradiance on a cloudy day is less than 400 W/m^2 , while it reaches up to 1000 W/m^2 during hours 12 through 13 on a clear day. It can be perceived from figures that on a cloudy day, the maximum solar irradiance is not only lower than half that on a clear day but is also sharply fluctuating. As shown in Figs. 6.8 and 6.9, 2D CNN-BLSTM follows the actual solar irradiance values with higher accuracy compared to other methods. Even though both LSTM-Choquet and K-means-CNN are capable of capturing complex features of nonlinearity with high abstraction, the 2D CNN-BLSTM significantly outperforms all of them, especially when it comes to predicting sharp spike points.

Table 6.1: Comparison of GHI Forecasting Results.

Forecasting Method	RMSE (W/m ²)	MAPE (%)	MAE (W/m ²)
UC-M3 [40]	164.57	22.79	120.51
PCA-KNN [144]	114.64	16.12	79.38
K-means-CNN [171]	109.17	14.71	72.23
LSTM- Choquet [2]	98.83	13.03	66.52
Proposed (CNN+BLSTM)	69.44	6.97	47.53

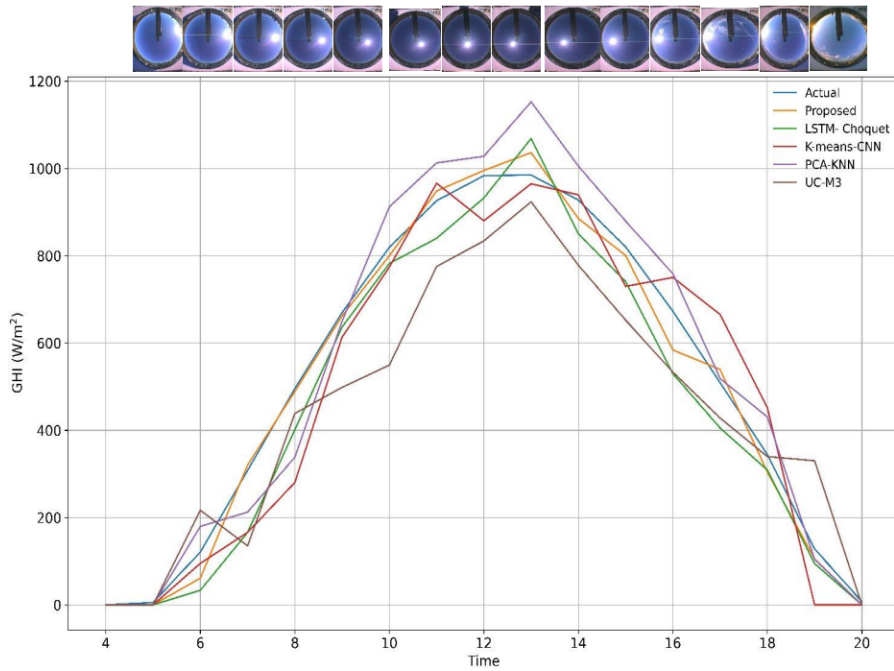


Figure 6.8: Comparison of forecasting results for a typical day in summer with sunny and clear conditions (i.e., 2017-06-26).

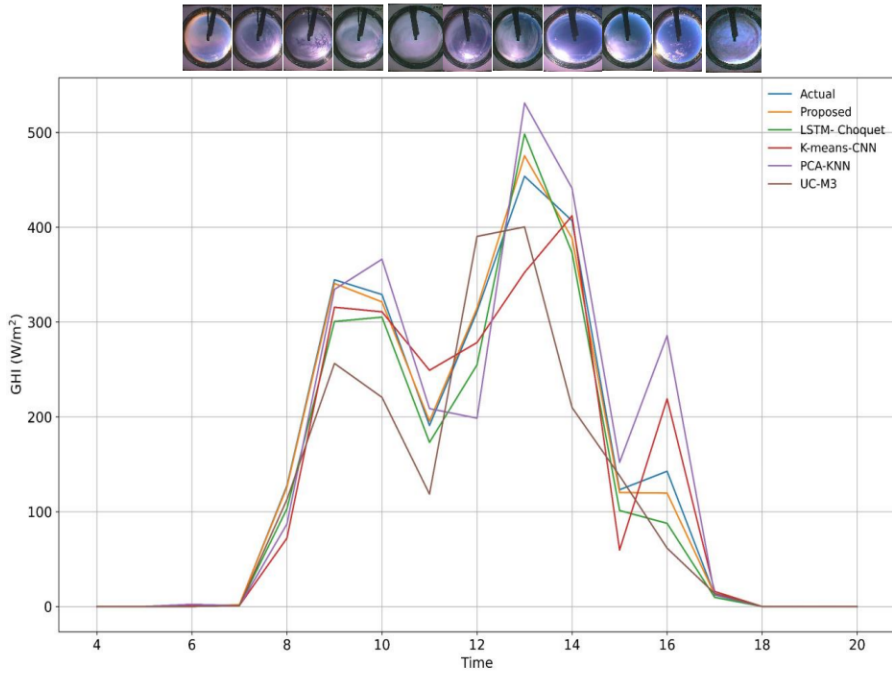


Figure 6.9: Comparison of forecasting results for a typical day in winter with partly cloudy, and cloudy conditions (i.e., 2017-11-17).

6.3.2 PV-Integrated Energy Hub Scheduling Problem Based on 2-D CNN-BLSTM+DDPG Model

The performance of the proposed DDPG-based approach is evaluated to delve into its advantage of making the best possible continuous decisions across the entire action space using the following scenarios:

1. Scheduling of the PV-integrated energy hub with SP approach proposed in [65, 102, 112].
2. Scheduling of the PV-integrated energy hub with RO method presented in [159, 169].
3. Scheduling of the PV-integrated energy hub with stochastic/IGDT method presented in [31].
4. Scheduling of the PV-integrated energy hub with DQN+2D-CNN-BLSTM framework.

Table 6.2: Energy Hub Average Daily Operating Costs.

Scheduling Method	Optimization type	Average Cost (\$/day)	Cost Change (%)
RO [159, 169]	model-based	6,685	+38.66
SP [65, 102, 112]	model-based	6,583	+36.54
Stochastic/IGDT [31]	model-based	6,106	+26.55
DQN+2D-CNN-BLSTM	model-free	5,538	+14.87
Proposed	model-free	4,821	0

5. Scheduling of the PV-integrated energy hub with the proposed DDPG+2D-CNN-BLSTM framework.

An adequate number of scenarios is generated for modeling the uncertain parameters in the stochastic method by the Monte Carlo simulation approach. Furthermore, to reduce the number of scenarios, the fast backward/forward scenario reduction technique is employed. As a result of offline training, the proposed DDPG-based network is saved at convergence for energy hub dynamic energy management. During every decision-making time interval, the current electric and thermal demands, energy storages' SoC, electricity and natural gas prices, and available PV generation are provided as the inputs for the online actor network trained based on Algorithm 1. For the DQN+2D-CNN-BLSTM framework, the action spaces are designed and discretized as suggested in [17] into five integer values. That is, 5^7 different choices make up the action space. The network is trained using the Adam optimizer with a learning rate of 0.001. The discount rate and mini-batch size are chosen to be 0.9 and 64, respectively. The Q network consists of two hidden layers with 150 and 200 ReLU neurons in each hidden layer, respectively.

Table 6.2 compares the average daily operating costs using the five scheduling methods over the test days. Due to the worst-case scenario being taken into consideration, the RO results in a high value of the operating cost compared to other models. SP has slightly better performance in comparison with RO. On

the other hand, as SP solves several deterministic scenarios simultaneously, it takes longer to calculate than RO, which only utilizes one scenario. Among all model-based benchmarks, Stochastic/IGDT, as a hybrid model, has the lowest cost. This model obtains 8.66% and 7.24% less average daily operating cost during the test period, compared to RO and SP, respectively. Although recently proposed hybrid model-based methods, stochastic/IGDT, are able to achieve lower operating costs compared to RO and SP techniques, model-free methods, DQN+2D-CNN-BLSTM and DDPG+2D-CNN-BLSTM, show better results. Between model-free frameworks, the proposed DDPG+2D-CNN-BLSTM generally has the lowest average daily operating cost due to making continuous decisions that find solutions close to the optimal solution of the optimization problem. The sub-optimal scheduling policy obtained by DQN is the result of discarding useful information from the dispatch action domain structure due to the discretization of the action space.

6.4 Conclusion

In this study, the optimal energy management problem of a PV-integrated energy hub is studied. A novel DDPG+2D-CNN-BLSTM approach as a fully model-free and data-driven DRL framework is proposed to provide an intelligent control strategy. Due to the nonconvex nature and highly intermittent parameters involved in the energy hub scheduling problem like nonconvex feasible operating regions of CHP units, valve-point effects of power-only units, and fuel cell dynamic efficiency, the proposed hybrid method is introduced to perform more efficient and cost-effective operations. Moreover, a forecasting model based on CNN and BLSTM networks is developed to provide great potential for the proposed DDPG-based agent to learn an optimal policy efficiently, especially during cloudy days with highly intermittent PV power generation. Case studies on typical summer and winter days demonstrate that, by using meteorological components and sky images, the proposed approach is able to follow the sharp spikes accurately even during hours of highly fluc-

tuating and random solar radiation. The simulation results demonstrate that the continuous decision-making provided by the proposed DRL-based control strategy is approximately 15% more cost-effective than that of the DQN-based method.

Chapter 7

SFNAS-DDPG: A Biomass-based Energy Hub Dynamic Scheduling Approach via Connecting Supervised Federated Neural Architecture Search and Deep Deterministic Policy Gradient

In this chapter, a dynamic scheduling framework for a multi-source multi-product facility with a biomass-solar hybrid renewable system is developed by taking into account the nonlinear characteristics of the biogas production facility and incorporating a novel neural architecture search (NAS) technique to learn the architecture and model parameters of the DNNs. The study is directed toward presenting a dynamic scheduling framework for a biomass-based energy hub. An improved actor-critic DRL algorithm, DDPG, and the supervised federated neural architecture search (SFnAS) are incorporated and employed to form a novel model-free and self-adaptable energy management algorithm for a RES-based multi-carrier energy supply infrastructure. With focusing on the ever-increasing role of biomass energy resources worldwide, the impact of several underlying factors on the cost-benefit analysis of a biomass-

based energy hub is investigated using a fully data-driven and model-free actor-critic DRL-based decision making framework taking into consideration the physical characteristics and thermodynamic effect of temperature-sensitive biogas production at the operation stage. For a diverse and dynamic RES-based energy hub system, these characteristics can facilitate flexible scheduling and coordinated decision-making. The proposed SFNAS tries to investigate the merits and limitations of various NAS methods for learning the architecture and model parameters for a given task. An innovative method is then presented for engaging multiple NAS approaches and improving their individual performance by utilizing a supervising agent to improve their training losses. Based on the FL settings, the proposed SFNAS approach can be used directly to search for the optimal architecture by leveraging training loss reshaping by a supervisor. As a result of repeated interaction with the environment, the DDPG agent can gain experience to provide optimal dynamic control signals without the need to model constrained probability distributions or uncertainty sets. Moreover, a forecasting technique based on convolutional neural networks (CNNs) and gated recurrent units (GRUs) has been incorporated into the DDPG decision-making framework to achieve decent scheduling results.

This Chapter is organized as follows: Section 7.1 presents the proposed SFNAS algorithm and the hybrid DL-based 2-D CNN-GRU prediction approach. Then, Section 7.2 describes the highly nonlinear, realistic model of the system. Following that, Section 7.3 presents the DDPG-based dynamic scheduling method for the biomass-based multi-carrier energy system. Section 7.4 is dedicated to the case studies and simulation results, and finally, conclusions are provided in Section 7.5.

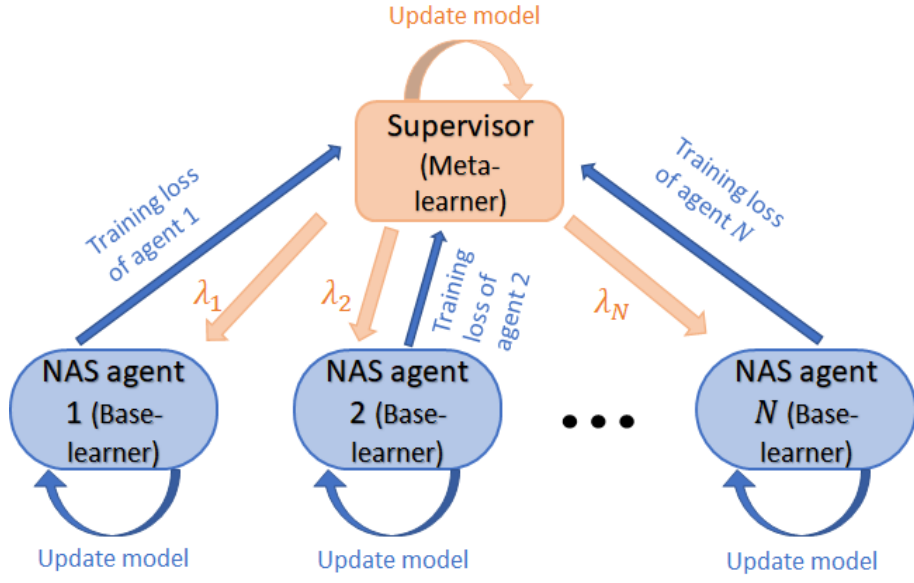


Figure 7.1: Schematic diagram of the proposed SFNAS methodology.

7.1 Supervised Federated Neural Architecture Search And Hybrid 2-D CNN-GRU Forecasting Model

In this Section, the mathematical representation of the proposed SFNAS, which leverages a supervisor to enhance the performance of multiple NAS agents, is presented. The supervisor (meta learner) and NAS agents (base learners) are trained using a bi-level optimization strategy. Figure 7.1 illustrates the schematic diagram of the proposed SFNAS methodology.

7.1.1 NAS Agents As Base Learners

Objective: by learning the architecture, ω_n , and parameters, θ_n , of the model, each base learner i optimizes its own model using *momentum-regularized* NAS technique. (ω_n, θ_n) is learned by each base-learner n using a momentum-

based gradient descent algorithm as follows.

$$\begin{aligned} v_n &:= (1 - \lambda_n)v_n + \lambda_n \nabla_n J_n(\theta_n, \omega_n) \\ \theta_n &\leftarrow \theta_n - \alpha_\theta v_n, \\ \omega_n &\leftarrow \omega_n - \alpha_\omega v_n \end{aligned} \tag{7.1}$$

where α_θ and α_ω correspond to the learning rates for θ and ω , respectively, and, v_n represents the momentum from past steps. When the hyperparameter λ_n is set to a lower value in the updates, longer gradient updates are maintained (this can be demonstrated by expanding the recursive updates, which are not shown here due to limited space). According to the NAS algorithm used by each base-learner, the training loss varies. Hence, for ease of explanation, the training loss is denoted by $J_n(\theta_n, \omega_n)$. The following definition of L_2 -regularized mean squared error (MSE) will be used when we assume identical training losses $J_n(\cdot, \cdot)$ for all agents.

$$J_n(\theta_n, \omega_n) := \|y - \hat{y}_n\|^2 + L_2(\theta_n) \tag{7.2}$$

where \hat{y}_n represents the forecasted value, i.e., the outcome of n -th base-learner's model with architecture ω_n . Model: the weights λ_n that are proportional to r_n are estimated by training the meta-learner model with the input states (or the embedding of the inputs). For this purpose, a N -head classifier structure is employed, corresponding to λ_n , $n \in \{1, 2, \dots, N\}$. Unlike a typical classification problem, r_n s change epoch by epoch, so the target values vary. Selection procedure: the proposed SFNAS methodology includes a model selection procedure that is as follows.

$$\min_A [\zeta_1 \cdot N + \zeta_2 \cdot T + \zeta_3 \cdot RMSE] \tag{7.3}$$

where N , T , and $RMSE$ are the number of trainable parameters of deep learning model, training time, and the RMSE value for agent A , respectively. A FL application designer can determine the importance of the objectives by adjusting ζ_1 , ζ_2 , and ζ_3 .

7.1.2 Hybrid Deep 2-D CNN-GRU Structure

Meteorological and atmospheric variables greatly influence solar irradiance in solar power generation forecasting. A hybrid SFNAS-based DL model for solar irradiance prediction is presented to analyze a sequence of sky images and meteorological components by employing CNN and GRU structures, respectively. Several numerical meteorological features are employed in the proposed hybrid forecasting framework to enhance its capability to capture complex solar abstractions, including global horizontal irradiance (GHI), calendar features, temperature, relative humidity, and atmospheric pressure. The mathematical details of the hybrid deep CNN-GRU network can be found in [25][26][88].

7.2 Environment Model and Problem Formulation

The purpose of this Section is to discuss the main structure of the proposed biomass-based energy hub, taking into account nonlinear characteristics of the facility components such as biogas production thermodynamics, dynamic efficiency of fuel cells, valve admission behavior of power generation systems, and CHPs' non-convex operation regions.

7.2.1 Power-Only Units

Generally, power-only generation units are modeled by convex quadratic cost functions. Due to valve admission effects, these models do not take into account ripples in production cost; therefore, they cannot provide a practical solution for real-life applications. In this regard, the quadratic cost function is modified to include an absolute sinusoidal term to capture this phenomenon efficiently. Figure 7.2 shows the valve-point effects on the fuel cost of a power-only unit. The total operation cost including valve-point effects can be formulated as follows [106]:

$$C_{i,t}^c(E_{i,t}^c) = \alpha_i^{c_1} \cdot (E_{i,t}^c)^2 + \alpha_i^{c_2} \cdot E_{i,t}^c + \alpha_i^{c_3} + V_{i,t}^c(E_{i,t}^c) \quad (7.4)$$

Figure 7.2: Valve-point effects on the fuel cost of a power-only unit.

$$V_{i,t}^c(E_{i,t}^c) = |\lambda_i^c \sin(\rho_i^c (E_{i,\min}^c - E_{i,t}^c))| \quad (7.5)$$

$$E_{i,\min}^c \cdot I_{i,t}^c \leq E_{i,t}^c \leq E_{i,\max}^c \cdot I_{i,t}^c \quad (7.6)$$

where $\alpha_i^{c_1}$, $\alpha_i^{c_2}$, $\alpha_i^{c_3}$, λ_i^c , and ρ_i^c are the cost coefficients of the i^{th} power-only unit. I^c and VPE^c indicate the commitment status and valve-point effects, respectively.

7.2.2 Thermal Units

The k^{th} thermal unit's operating cost and limits at time t are defined by (7.7) and (7.8).

$$C_{k,t}^b(T_{k,t}^b) = \alpha_k^{b_1} \cdot (T_{k,t}^b)^2 + \alpha_k^{b_2} \cdot T_{k,t}^b + \alpha_k^{b_3} \quad (7.7)$$

$$T_{k,\min}^b \cdot I_{k,t}^b \leq T_{k,t}^b \leq T_{k,\max}^b \cdot I_{k,t}^b \quad (7.8)$$

where $\alpha_i^{b_1}$, $\alpha_i^{b_2}$, $\alpha_i^{b_3}$, and k^{th} represent the cost coefficients and commitment status of the k^{th} heat-only unit.

7.2.3 CHP Units

Noteworthy is the fact that the electricity and thermal energy produced in CHP units depend on each other, so they cannot be independently adjusted. The cost function of j^{th} CHP is provided in (7.9). Convex combinations of

extreme points represent the power and heat production in CHP units by (7.10)-(7.13) [4].

$$C_{j,t}^{chp} = \sum_{s=1}^S \sum_{d^s=1}^{D_j^s} \Gamma_{j,t}^{d^s} c_j^{d^s} \quad (7.9)$$

$$E_{j,t}^{chp} = \sum_{s=1}^S \left(\sum_{d^s=1}^{D_j^s} \Gamma_{j,t}^{d^s} x_j^{d^s} \right) \quad (7.10)$$

$$T_{j,t}^{chp} = \sum_{s=1}^S \left(\sum_{d^s=1}^{D_j^s} \Gamma_{j,t}^{d^s} y_j^{d^s} \right) \quad (7.11)$$

$$\sum_{d^s=1}^{D_j^s} \Gamma_{j,t}^{d^s} = V_{j,t}^s \quad (7.12)$$

$$0 \leq \Gamma_{j,t}^{d^s} \leq 1 \quad (7.13)$$

where D_j^s denotes the total number of corner points for the j^{th} CHP in sub-region s and the coefficient $\Gamma_{j,t}^{d^s}$ should satisfy constraints (7.12) and (7.13); $(x_{chp}^{d^s}, y_{chp}^{d^s})$ represents the electricity and thermal generations related to the corner point d^s ; $V_{j,t}^s$ is a binary variable indicating operation in the s^{th} sub-region.

7.2.4 Biomass-based Boiler Units

The m^{th} Biomass-based boiler's operating cost is modeled in (7.14). Based on the energy conservation rules, the thermal energy produced by the biomass-based boiler is calculated by (7.15)-(7.17), while it is restricted within acceptable limits by constraint (7.18) [85].

$$C_{m,t}^{bm} (T_{m,t}^{bm}) = T_{m,t}^{bm} \cdot \alpha_m^{bm} \quad (7.14)$$

$$T_{m,t}^{bm} = \frac{\vartheta^{bm} \cdot \varsigma^{bm} \cdot VOL^{bm}}{T_{HR}^{bm}} \left(1 - \frac{\kappa^{bm}}{(T_{HR}^{bm} \cdot \pi^{bm}) - 1 + \kappa^{bm}} \right) \quad (7.15)$$

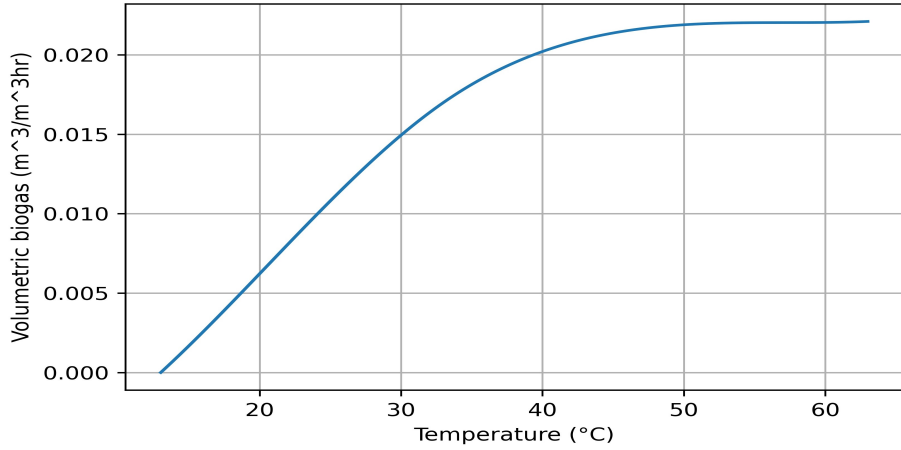


Figure 7.3: Nonlinear relationship between biogas production and temperature.

$$\kappa^{bm} = \alpha_1^{bm} e^{\alpha_2^{bm} \cdot IVS} + \alpha_3^{bm} \quad (7.16)$$

$$T_{m,t}^{bm} = \varpi_{m,t}^{bm} \cdot CV^{bm} \cdot \eta_m^{bm} \quad (7.17)$$

$$T_{m,\min}^{bm} \cdot I_{m,t}^{bm} \leq T_{m,t}^{bm} \leq T_{m,\max}^{bm} \cdot I_{m,t}^{bm} \quad (7.18)$$

where α_m^{bm} , ϖ_m^{bm} , CV^{bm} , and η_m^{bm} denote the cost coefficient, mass of injected biomass feedstock, calorific value of biomass feedstock, and efficiency of the m^{th} biomass-based boiler, respectively; κ^{bm} is the sability and process rate kinetic parameter; π^{bm} is the thermophilic and mesophilic digestion's micro-organism growth rate; ϑ^{bm} , ς^{bm} , T_{HR}^{bm} and VOL^{bm} represent biogas biochemical potential, influent volatile solid concentration, hydraulic retention time and digester's volume, respectively. The nonlinear relationship between biogas production and temperature is illustrated in Figure 7.3.

7.2.5 Fuel Cell unit

Fuel cells (FCs) contribute to the energy hub demand by generating electricity, recovering heat, and producing hydrogen. In the l^{th} fuel cell unit, the amount

of recovered thermal power, $T_{l,t}^{fc}$, can be determined as follows:

$$T_{l,t}^{fc} = TER_{l,t}^{fc} \cdot \left(E_{l,t}^{fc,e} + \underline{E}_{l,t}^{fc,h} \right) \quad (7.19)$$

$$E_{l,t}^{fc,total} = E_{l,t}^{fc,e} + \underline{E}_{l,t}^{fc,h} \quad (7.20)$$

$$E_{l,min}^{fc} \cdot I_{l,t}^{fc} \leq E_{l,t}^{fc,e} + \underline{E}_{l,t}^{fc,h} \leq E_{l,max}^{fc} \cdot I_{l,t}^{fc} \quad (7.21)$$

where $\underline{E}^{fc,h}$, $E^{fc,e}$, and TER^{fc} are equivalent electric power for hydrogen production, electrical output power, and the thermal to electrical power ratio, respectively. The amount of stored hydrogen and charged/discharged hydrogen can be formulated as follows:

$$T2T_{l,t}^{fc} = T2T_{l,t-1}^{fc} + (\eta_{l,ch}^{T2T} \cdot T2_{l,t}^{in}) - \left(T2_{l,t}^{out} / \eta_{l,dch}^{T2T} \right) \quad (7.22)$$

$$T2_{l,t}^{in} = \underline{E}_{l,t}^{fc,h} \cdot \psi^{E2T} \quad (7.23)$$

$$T2_{l,t}^{out} = \overline{E}_{l,t}^{fc,h} \cdot \psi^{E2T} \quad (7.24)$$

$$T2T_{l,min}^{fc} \leq T2T_{l,t}^{fc} \leq T2T_{l,max}^{fc} \quad (7.25)$$

$$T2_{l,min}^{in} \cdot I_{l,t}^{T2T,ch} \leq T2_{l,t}^{in} \leq T2_{l,max}^{in} \cdot I_{l,t}^{T2T,ch} \quad (7.26)$$

$$T2_{l,min}^{out} \cdot I_{l,t}^{T2T,dch} \leq T2_{l,t}^{out} \leq T2_{l,max}^{out} \cdot I_{l,t}^{T2T,dch} \quad (7.27)$$

$$I_{l,t}^{T2T,ch} + I_{l,t}^{T2T,dch} \leq 1 \quad (7.28)$$

where ψ^{E2T} , $T2^{in/out}$, and $T2T$ indicate the hydrogen (kg) to electric power (kW) ratio, equivalent charged/discharged hydrogen, and stored hydrogen. Most existing studies on FC consider its efficiency to be constant, whereas it can vary according to the amount of electricity produced. Based on Figure 7.4, the thermal to electrical power ratio and the efficiency are functions of the part load ratio variable [38]. Equation (7.29) gives the total operating cost of the fuel cell unit.

$$\begin{aligned} C_{l,t}^{fc} \left(E_{l,t}^{fc,e}, \underline{E}_{l,t}^{fc,h} \right) &= \left(\frac{E_{l,t}^{fc,T} \pi_t^{ng}}{\eta_{l,t}^{fc}} \right) \\ &+ \left(C_l^{fc,p} \cdot \underline{E}_{l,t}^{fc,h} \right) + \left(C_l^{fc,OM} \cdot E_{l,t}^{fc,T} \right) \end{aligned} \quad (7.29)$$

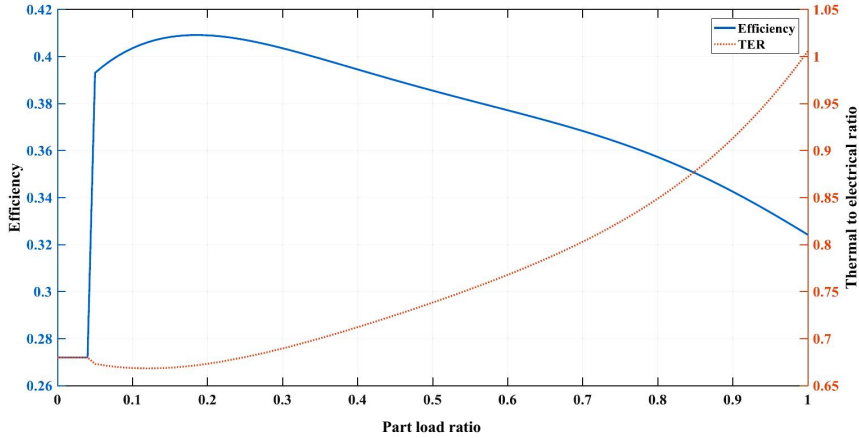


Figure 7.4: An illustration of the FC unit's dynamic performance curve.

7.2.6 Power Balance

During each time interval t , the amount of electrical and thermal power produced and consumed should be equal, as stated in (7.30) and (7.31).

$$\sum_{i \in N_C} E_{i,t}^c + \sum_{j \in N_{CHP}} E_{j,t}^{chp} + \sum_{l \in N_{FC}} \left(E_{l,t}^{fc,e} + \bar{E}_{l,t}^{fc,h} \right) + E_t^{bes} + E_t^{pv} + E_t^{grid} = E_t^l \quad (7.30)$$

$$\sum_{k \in N_B} T_{k,t}^b + \sum_{j \in N_{CHP}} T_{j,t}^{chp} + \sum_{l \in N_{FC}} T_{l,t}^{fc} + \sum_{m \in N_{BM}} T_{m,t}^{bm} + T_t^{bt} = T_t^l + T_t^{sv} \quad (7.31)$$

where E^{grid} , E^{bes} , and E^l indicate the amount of power exchange with the upstream network, the amount of power charged/discharged, and the electrical demand, respectively. T^l , T^{bt} , and T^{sv} represent the thermal demand, thermal power charged/discharged, and the slack variable [16], respectively. Detailed information on electrical and thermal storage systems is available in [31].

7.2.7 Objective Function

In the dynamic scheduling problem for biomass-based energy hub, the objective is to minimize the system operating cost, as stated in (7.32).

$$OC = \sum_{t \in N_T} \left\{ \begin{array}{l} \sum_{i \in N_C} C_{i,t}^c + \sum_{k \in N_B} C_{k,t}^b + \sum_{m \in N_{BM}} C_{m,t}^{bm} \\ + \sum_{j \in N_{CHP}} C_{j,t}^{chp} + \sum_{l \in N_{FC}} C_{l,t}^{fc} + C_t^{grid} \end{array} \right\} \quad (7.32)$$

7.3 Deep Deterministic Policy Gradient Algorithm

This Section discusses the main structure of the proposed optimal control strategy using the actor-critic DRL algorithm. Since DDPG provides continuous action spaces and does not require discretization, which is computationally expensive, it allows for more effective exploration of the action space. Therefore, obtaining an optimum control decision requires fewer iterations than other techniques regardless of the type of problem encountered. And more importantly, the multi-carrier energy system's infrastructure is controlled more smoothly than when they are regulated at a discrete level.

DDPG assesses the cost-benefit of selecting a control signal over a given period, $a_t \in \mathcal{A}_t$, while making decisions in each state of the system using Q-value, $Q(s_t, a_t)$. According to the Bellman equation, the Q-value of any action, a_t , at state s_t can be calculated based on the optimal action's Q-value at state s_{t+1} as follows.

$$Q(s_t, a_t) = \mathcal{R}(s_t, a_t) + \gamma \mathbb{E} \left[\max_{a_{t+1} \in \mathcal{A}_{t+1}} Q(s_{t+1}, a_{t+1}) \right] \quad (7.33)$$

where $\gamma \in [0, 1]$ and \mathcal{R} represent the discount factor and reward function, respectively.

The energy hub operator, however, does not have any information about either the most effective action at state s_{t+1} or what its value would be over time. The DDPG method addresses this challenge by implementing two separate DNNs. The most beneficial action at state s_{t+1} is estimated by the actor

network, $\mu(s_t | \theta^\mu)$, while the critic network, $Q(s_t, a_t | \theta^Q)$, has the responsibility of estimating the Q-value of action a_t at state s_t . The actor and critic network weight vectors, θ^μ and θ^Q , are continuously updated based on the observed rewards at each time step during the training process. Using the trained networks, the Q-value can be derived as follows:

$$Q(s_t, a_t) \approx \mathcal{R}(s_t, a_t) + \gamma \mathbb{E}[Q(s_{t+1}, \mu(s_{t+1} | \theta^\mu) | \theta^Q)] \quad (7.34)$$

Actor networks respond to sampled states of a system by taking action. Then, the two networks can be simultaneously trained according to the received reward. The s_t and $\max_a Q(s_t, a_t | \theta^Q)$ serve as the input and the output for the actor network, while the critic network takes (s_t, a_t) , where $a_t = \mu(s_t | \theta^\mu)$, and \mathcal{R}_t as the input and the output, respectively. A replay buffer consisting of samples from different time steps, $(s_t, a_t, \mathcal{R}_t, s_{t+1})$, is employed to reduce correlation-induced errors during updating the networks. Copies of the original actor and critic networks, the target networks, are taken and gradually updated to make the training process more stable. Moreover, the actor network is enhanced with a correlated stochastic noise signal to improve exploration during the training process. The most commonly used random noises are Ornstein-Uhlenbeck and Gaussian noises. An Ornstein-Uhlenbeck noise can be used to simulate time-related noise data. The Ornstein-Uhlenbeck process is useful for solving physical control problems that are inertia-driven. Through this perturbation, the DDPG agent is more able to explore and achieve faster convergence as a result. The signal Ω is modeled by employing the Ornstein-Uhlenbeck procedure, as stated in (7.35).

$$\Omega^t = \Omega^{t-1} + (\Omega^{mean} - \Omega^{t-1}) \kappa T_s + \Omega^\sigma n \sqrt{T_s} \quad (7.35)$$

where Ω_σ and Ω_{mean} denote the variance of the noise model and the mean value, respectively. κ and $n \in [0, 1]$ represent the mean attraction constant and a uniformly generated random number, respectively. The critic network is trained using $\mathcal{L}(\theta^Q)$ as the loss function.

$$\mathcal{L}(\theta^Q) = \frac{1}{N} \sum_{i \in N} [Q(s_i, \mu(s_i | \theta^\mu) | \theta^Q) - \mathcal{Y}_i]^2 \quad (7.36)$$

where N is the size of the mini-batch, and \mathcal{Y}_i represents the measured value function as follows.

$$\mathcal{Y}_i = \mathcal{R}(s_t, a_t) + Q\left(s_{t+1}, \mu\left(s_{t+1} \mid \theta^{\mu'}\right) \mid \theta^{Q'}\right) \quad (7.37)$$

Meanwhile, the actor network needs to be trained by (7.38).

$$\nabla_{\theta^{\mu}} \mathcal{L}(\theta^{\mu}) = \frac{1}{N} \sum_{i \in N} \nabla_a Q\left(s_i, \mu\left(s_i \mid \theta^{\mu}\right) \mid \theta^Q\right) \nabla_{\theta^{\mu}} \mu\left(s_i \mid \theta^{\mu}\right) \quad (7.38)$$

The final step in the process involves gradually updating the target networks with the smoothing factor τ , as stated in (7.39) and (7.40).

$$\theta^{\mu'} = (1 - \tau) \theta^{\mu'} + \tau \theta^{\mu} \quad (7.39)$$

$$\theta^{Q'} = (1 - \tau) \theta^{Q'} + \tau \theta^Q \quad (7.40)$$

In the dynamic dispatch problem of the multi-carrier energy system, the state and action vectors can be defined by (7.41) and (7.42), respectively.

$$s_t = \left\{E_t^{pv}, \hat{E}_t^{pv}, \pi_t^e, \pi_t^{ng}, SoC_t^{bes}, SoC_t^{bt}, E_t^l, T_t^l\right\} \quad (7.41)$$

$$a_t = \left\{E_{i,t}^c, E_{j,t}^{chp}, T_{k,t}^b, T_{m,t}^{bm}, E_{l,t}^{fc,e}, E_{l,t}^{fc,h}, E_t^{bes}, T_t^{bt}\right\} \quad (7.42)$$

$\mathfrak{S}(s_t, a_t, \omega_t)$ governs the transition from state s_t to state s_{t+1} . It's not just the decision-making signal a_t that determines transitions, but also environmental uncertainty, ω_t , that influences them. There are several exogenous factors, including energy consumption habits and solar irradiance, that influence the alignment of probabilistic models within this context. By learning the transition implicitly from collected data samples, a DRL approach can overcome this challenge without the need for statistical models.

A DDPG reward is calculated by the agent by adjusting the parameters as follows:

$$\mathcal{R}(s_t, a_t) = -(OC_t + C_t^{Penalty}) \quad (7.43)$$

Training with DNN makes DRL-based techniques non-constrained, ignoring the physical limitations of dynamic scheduling. Therefore, the physical constraints cannot be addressed systemically through this process. Nonetheless, energy systems scheduling needs to address security and reliability concerns. For a variable $\aleph \in [\aleph^{\min}, \aleph^{\max}]$ a penalty term is added to the reward function to address the constraint violation problem, , as stated in (7.44) and (7.45).

$$C^{Penalty} = \sum_{\aleph_i \in N_{\aleph_i}} \mathfrak{I}_i.Penalty_{\aleph_i} \quad (7.44)$$

$$Penalty_{\aleph} = \ln \left(\frac{|\aleph - \aleph^{\min}| + |\aleph - \aleph^{\max}|}{2 \cdot (\aleph^{\max} - \aleph^{\min})} \right) \quad (7.45)$$

7.4 Numerical Study

The biomass-based energy hub shown in Figure 7.5 is used as a case study to evaluate the effectiveness of the proposed SFNAS-DDPG dynamic scheduling approach. The proposed SFNAS-DDPG strategy involves scheduling and operating a multi-source multi-product facility that participates in the energy market as a coupled multi-carrier energy supply. The energy loads and prices are adapted from [116][137], respectively. Based on a test case presented in [11], the economic data and operational constraints for the generation plants are derived and scaled. The maximum capacities of heat-only, PV, and power-only units are 2.695 MWth, 0.75 MW, and 1.25 MW, respectively. Moreover, the data of the 0.6 MWth biomass-based boiler and the 1 MW FC units are taken from [38,70], respectively. Both the sky images and numerical time series data are obtained from the Solar Radiation Research Laboratory (SRRL) dataset of the National Renewable Energy Laboratory (NREL), located in Colorado [133]. Based on the FL settings, the SFNAS approach is used directly to search for the optimal architecture of the forecasting network using supervisory training loss reshaping. As a representation network, the output of the CNN-GRU model is concatenated with the states of the energy hub

before being fed into an actor network. For the critic and actor networks, learning rates of 0.001 and 0.0001 are selected, respectively. The mini-batch of random experience and the discount factor have been selected as 0.95 and 64, respectively. The parameters of the noise model are taken from [123]. Algorithm 3 demonstrates the training process of making control decisions using the proposed SFNAS-DDPG methodology. The training process of the proposed technique is performed by Keras library and TensorFlow as the backend on a workstation with an NVIDIA GeForce GTX 1070 GPU and 32 GB of RAM.

7.4.1 Design Prediction Model With SFNAS Method

In this subsection, the SFNAS algorithm is employed to identify the most accurate architectures for the solar irradiance forecasting task. The CNN and LSTM/BLSTM/GRU networks' hyperparameters significantly affect the model's performance in a complicated manner. However, trying to model the complex interactions between the hyperparameters or manually examining a large number of possible architectures is challenging and time-consuming. To overcome these limitations, the SFNAS algorithm is proposed and implemented to efficiently select the networks' architectures. Algorithm 4 shows the procedure of the proposed SFNAS methodology. The goal is to find optimized models that are capable of better solar irradiance forecasting given the baseline structure of the model discussed in Subsection 7.1.2. For this purpose, we seek to optimize the following parameters of the representation network, shown in Figure 7.5:

- Number of convolutional layers in the CNN network (N^C)
- Number of hidden units in the first LSTM/BLSTM/GRU layer (N^{B1})
- Number of hidden units in the second LSTM/BLSTM/GRU layer (N^{B2})
- Number of hidden units in the third LSTM/BLSTM/GRU layer (N^{B3})

Algorithm 3: Offline training process of the DDPG agent

Initialize: Initialize the weights of the actor and critic networks randomly:
 $\mu(s|\theta^\mu) : \theta^\mu = \theta^{\mu_0}$
 $Q(s, a|\theta^Q) : \theta^Q = \theta^{Q_0}$

Initialize Ω as a random process allowing exploration of actions and set up the experience replay buffer M .

for $i \in N^{episodes}$ **do**

Observe s_t as the state space.

Concatenate the output of the CNN-GRU network with the state space s_t .

for $t \in N^{time\ intervals}$ **do**

Choose the dynamic scheduling action $a_t = \mu(s_t|\theta^\mu) + \Omega_t$.

Solve (7.32) by taking energy hub control decision a_t and receive R_t as the immediate reward.

Transfer to s_{t+1} as the new state.

Store the transition (s_t, a_t, R_t, s_{t+1}) into M .

$k \leftarrow k + 1$;

if $batch_size \leq |M|$ **then**

Randomly select $\mathfrak{F} = \{(s_j, a_j, R_j, s_{j+1})\}_{j=1}^{\neq \mathfrak{F}}$ as a mini-batch from M .

Minimize the loss function (7.36) to update the critic network.:
 $\theta^Q \leftarrow \eta^Q \nabla_{\theta^Q} \mathcal{L}(\theta^Q) + \theta^Q$

Use (7.38) and sampled policy gradient to update the actor network:
 $\theta^\mu \leftarrow \eta^\mu \nabla_{\theta^\mu} \mathcal{L}(\theta^\mu) + \theta^\mu$

Use (7.39) and (7.40) to Update the target networks:
 $\theta^Q \leftarrow \theta^{Q'}$
 $\theta^\mu \leftarrow \theta^{\mu'}$

end if

end for

end for

Based on our previous work [29], we find that N^{B1} and N^{B2} with fewer than 100 hidden units are likely to exhibit underfitting, while overfitting occurs when the number is greater than 400. To reduce the number of genotype representations from the range 100 to 400, we divide the range by 25 before exploring the two LSTM/BLSTM/GRU layers. In order to translate genotype to phenotype, a multiplier, 25, is assigned to the genotype. According to our previous knowledge, bounds are also set for the other parameters. Our experiments were conducted using the parameters listed in Table 7.1 as the lower and upper bounds.

Algorithm 4: SFNAS algorithm.

```

for  $epoch \in \{\text{number of epochs}\}$  do
    for  $agent \in \{\text{number of agents}\}$  do
        Forming the best architecture  $Z_i^*$  via agent's NAS
        Compute training loss architecture  $Z_i^*$ :
         $J_i(\theta_i, \omega_i) := \|y - \hat{y}_n\|^2 + L_2(\theta_i)$ 
    end for
    Compute relative contribution of agent:
     $r_i := J_i(\theta_i, \omega_i) / \sum_i J_i(\theta_i, \omega_i)$ 
    Train the classifier using the relative contribution,  $r_i$ , to estimate
    the weights  $\lambda_i$ 
end for
Select the based agent based on:
 $\min_A [\omega_1 RMSE + \omega_2 T + \omega_3 N]$ 

```

From the viewpoint of the EA-based NAS, a genotype then takes the form

Table 7.1: Hyperparameter bounds for SFNAS algorithm

Parameter	Lower bound	Upper bound
CNN network (N^C)	1	4
First LSTM/BLSTM/GRU layer (N^{B1})	4	16
Second LSTM/BLSTM/GRU layer (N^{B2})	4	16
Third LSTM/BLSTM/GRU layer (N^{B3})	4	12

of a sequence of integers based on the values indicated in Table 7.1 and phenotypes are the resulting structures. In the proposed stacking model, hierarchical features can be derived from the feature representation of the previous layer and the next layer serves as a layer of abstraction. This hierarchical feature abstraction cannot be achieved when the next layer (i.e., N^{B^2}) is greater than the previous layer (i.e., N^{B^1}) and results in overfitting. As a result, to ensure that the N^{B^2} is equal to or smaller than N^{B^1} when converting genotypes to phenotypes, a correction mechanism is applied on N^{B^2} (similar correction mechanism is also considered for (N^{B^3})) as follows:

$$N^{B_i} = \begin{cases} N^{B_i} & N^{B_i} \leq N^{B_{i-1}} \\ N^{B_{i-1}} & N^{B_i} \geq N^{B_{i-1}} \end{cases} \quad (7.46)$$

The population is initialized by randomly selecting $N^p - 1$ individuals. The so-called super-fit mechanism is employed to initialize the remaining population based on the parameters of the structure proposed in [29] to begin the evolutionary process with a sufficiently effective individual. An individual's fitness is determined by evaluating the created phenotype for the given genotype based on the root means square error (RMSE), mean absolute error (MAE), and mean absolute percentage error (MAPE) [29]. Both crossover and mutation are used to achieve a reasonable balance between exploration and exploitation. A probability of $P^c = P^m = 0.5$ is applied to each operator independently. Based on the one-point crossover methodology, individuals are firstly ranked according to their fitness, and then the $2n^{th}$ and $(2n + 1)^{th}$ ones are selected for crossover ($n \in [0, \frac{N^p}{2} - 1]$). The population is then uniformly mutated, consisting of individuals generated by crossover and offspring who were not subjected to crossover. Mutation can occur between each architecture parameter (gene) and a value uniformly chosen from its range according to a probability P^{gm} . As a result of this approach, we can conduct searches relatively faster while minimizing disruptive mutations in individuals. The fitness of the parents for each offspring is checked when creating the population of the next generation. Then, to monotonically decrease the population's

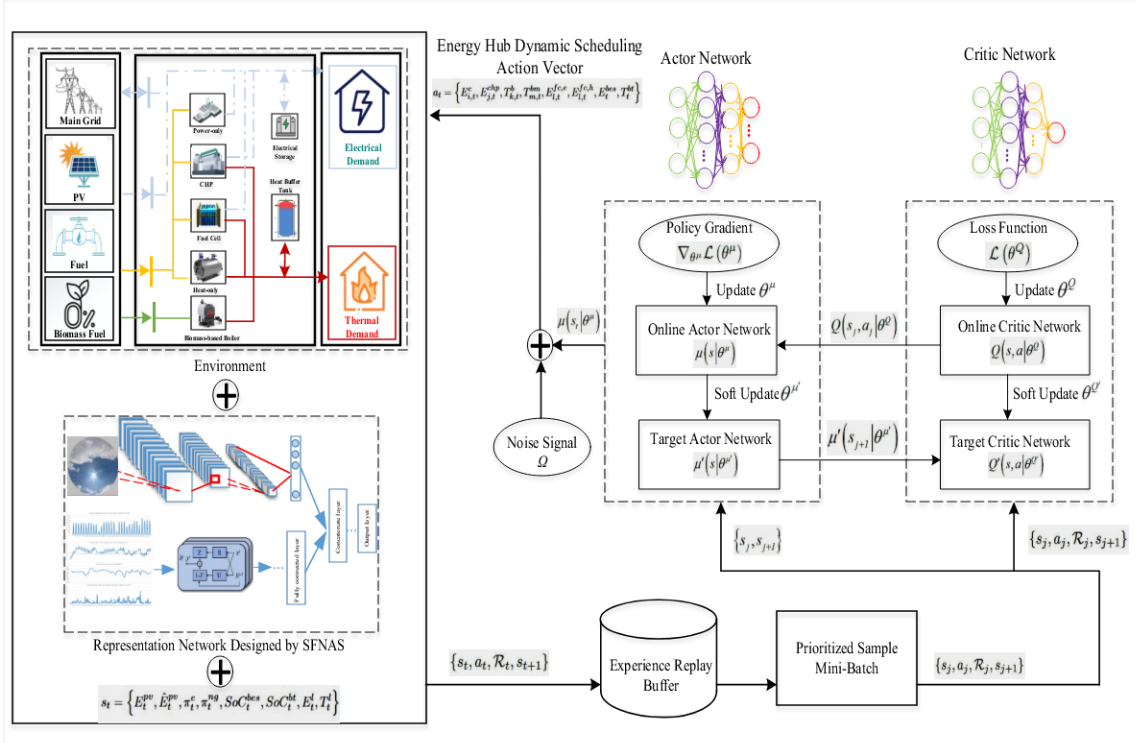


Figure 7.5: The schematic of the proposed SFNAS-DDPG framework for the dynamic scheduling of biomass-based energy hub.

mean fitness, offspring with better fitness than one of the parents replaces the worst parent.

Table 7.2 shows the training time and test RMSE for the best architecture found by each method. According to the results, the proposed SF-NAS technique outperforms the baseline NAS approach in all architectures. Fig 7.6 illustrates the evolution of the weights (λ) for the gradient term in the momentum update of the solar irradiance forecasting task. As can be seen from the evolution-based figures, the supervisor of the SFNAS provided the agents with guidance that ultimately led to a better optimization process. Moreover, the evolution of training and validation losses of the proposed CNN-LSTM/BLSTM/GRU networks is depicted in Figure 7.7 for both baseline and SFNAS strategies. It can be seen from this figure that networks built with SFNAS exhibit smaller spikes and smoother convergence than those based on

Table 7.2: Forecasting Task Results for the Best Architectures Found by SF-NAS and Baseline NAS.

Structure	Test RMSE		Offline training time	
	Baseline [101]	Proposed	Baseline [101]	Proposed
CNN-LSTM	66.23	63.37	4h 52min	4h 19min
CNN-BLSTM	62.88	57.28	5h 47min	5h 11min
CNN-GRU	62.35	56.51	4h 43min	4h 16min

Table 7.3: The Average Daily Operating Cost for the Proposed Multi-Carrier Energy System.

Scheduling Method	Average Profit (\$/day)	Profit Change
DDPG + State-of-the-art model [27]	5,416	0%
DDPG + Baseline NAS [101]	5,156	-4.79%
Proposed SFNAS-DDPG	5,020	-7.31%

baseline NAS.

7.4.2 Biomass-based Energy Hub Dynamic Scheduling Problem based the proposed SFNAS-DDPG

Table 7.3 illustrates the average daily operational cost of the biomass-based energy hub using DDPG + state-of-the-art forecasting [27], DDPG + baseline NAS [101], and the proposed SFNAS-DDPG models. As can be seen from this table, the proposed framework, SFNAS-DDPG, has the lowest average daily operating cost when compared with other models. The SFNAS-DDPG method has \$5,020 per day average operating costs, which shows a 7.31% improvement over the baseline model (DDPG + State-of-the-art). This improvement is due to the fact that the operator has access to more accurate information about the uncertain parameter (PV generation in future hours), enabling the agent to take more efficient actions.

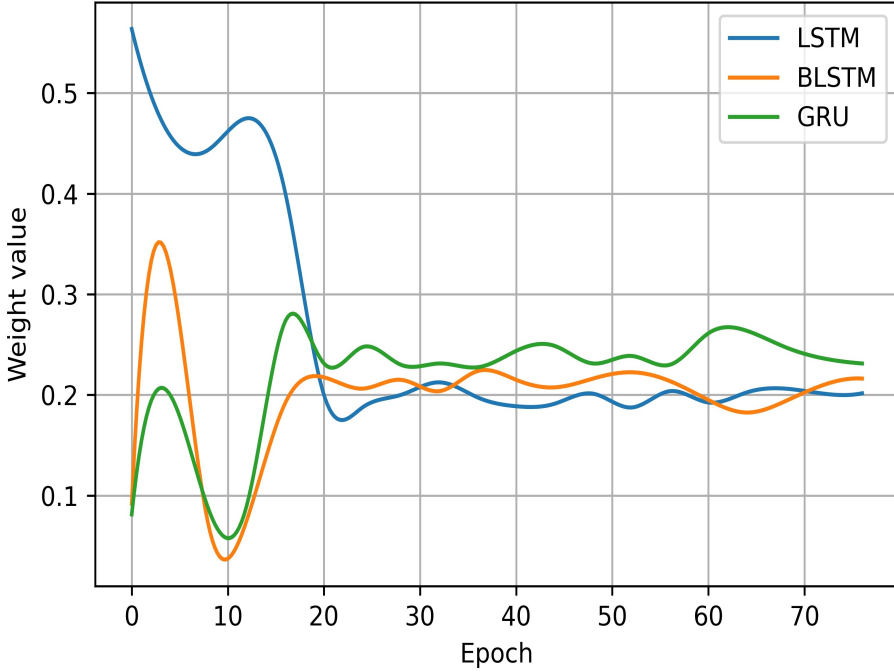


Figure 7.6: The evolution of weight (λ_i) for the gradient term in the momentum update.

7.5 Conclusion

This study presents SFNAS-DDPG as an improved actor-critic DRL framework for the optimal scheduling and operation of a multi-source multi-product facility, taking into account nonlinear characteristics of the facility components such as biogas production thermodynamics, dynamic efficiency of fuel cells, valve admission behavior of power generation systems, and CHPs' non-convex operation regions. To help the DDPG agent choose the most efficient control policy, especially when PV power is highly intermittent on cloudy days, a hybrid CNN-GRU forecasting model that captures high levels of abstraction from sky images and numerical measurements is developed and employed. The novel SFNAS technique is proposed to learn the architecture and model parameters of the representation network. By utilizing supervisor-led training loss reshaping, the proposed SFNAS approach can be used directly to determine the optimal architecture based on the federated settings. As a re-

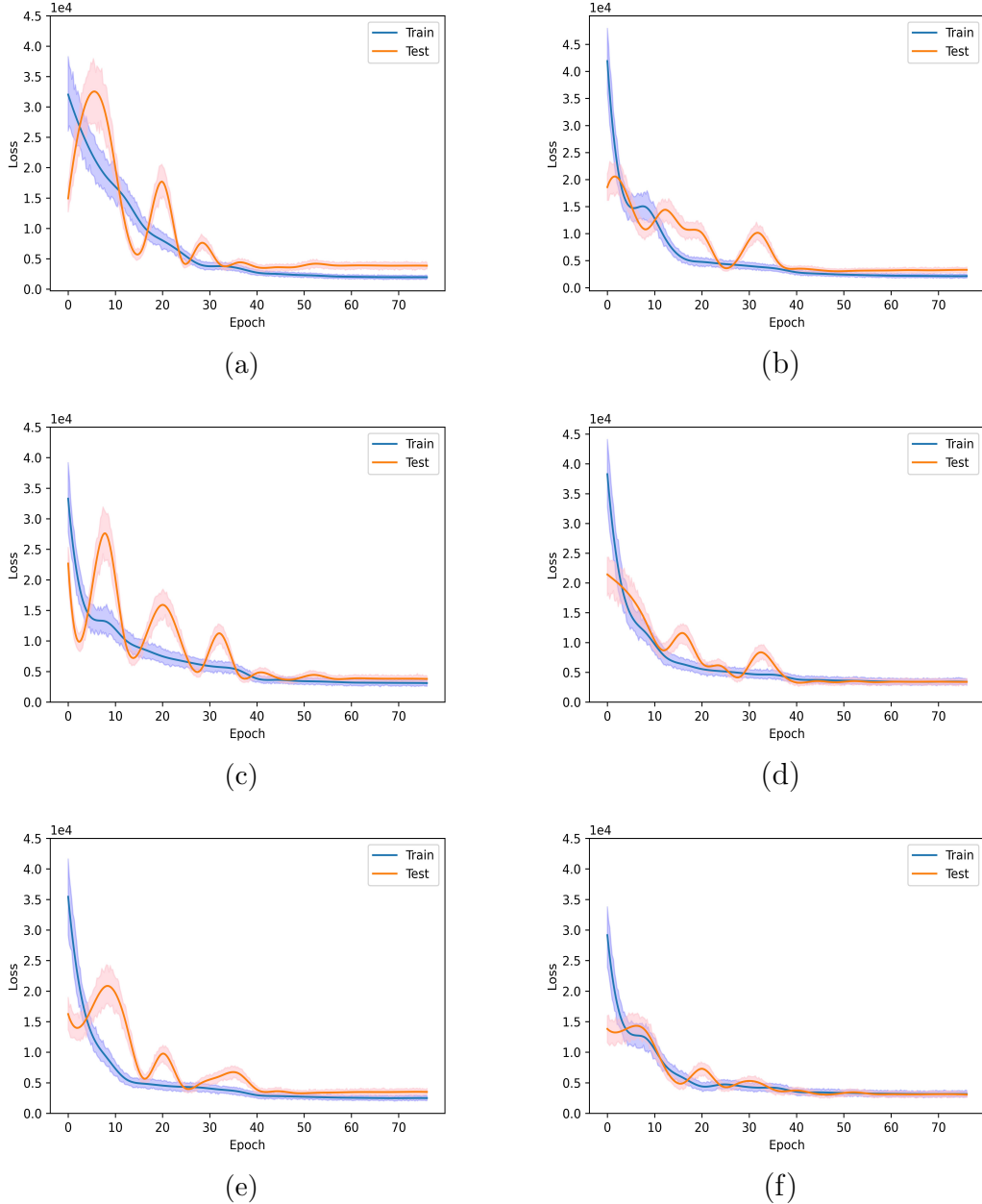


Figure 7.7: The evolution of training and validation losses of the proposed CNN-LSTM/BLSTM/GRU models (a) baseline NAS-based LSTM, (b) SFNAS-based LSTM, (c) baseline NAS-based BLSTM, (d) SFNAS-based BLSTM, (e) baseline NAS-based GRU, and (f) SFNAS-based GRU .

sult of our case studies, the proposed strategy, by selecting different network structures, is more accurate than the respective baseline forecasting methods. Consequently, The SFNAS-DDPG method has \$4,590 per day average operating costs, which shows a 4.79% improvement over the baseline model (DRL+State-of-the-art). While this study was geared toward exploring the effects of the proposed SFNAS methodology on improving actor-critic DRL framework’s control strategies, future work could study the effectiveness of replacing the proposed EA-based NAS with heterogeneous NAS methods.

Chapter 8

Conclusions and Future Work

This chapter makes some concluding remarks on the studies in this thesis and, subsequently, offers some potential research directions and interesting problems for future work.

8.1 Conclusions

This thesis belongs to the field of deep learning-based algorithms for forecasting and energy management problems and focuses on smart grid applications. The outcomes of the work in the thesis are summarized as follows:

1. First, in Chapter 3, a novel deep learning-based approach was proposed for short-term wind speed prediction. The DWPT was applied to effectively extract the features of the signal by decomposing the raw wind speed time series into several sub-layers. The input vector was built by using the theory of dynamic reconstruction, which not only increases the accuracy of the results but also decreases the learning complexity by determining the optimal structure of inputs. Moreover, the BLSTM network as a combination of LSTM networks and bidirectional RNNs was incorporated to capture deep temporal features with high abstractions. The proposed model was evaluated on a publicly available real-world dataset, of which the forecasting accuracy was comprehensively compared to multiple benchmarks in the literature. The proposed

BLSTM+DWPT framework demonstrated the smallest metrics and generally achieves the most accurate forecasting performance in the dataset. For example, BLSTM+DWPT showed 34% and 32% improvement in RMSE and MAE when compared with BLSTM+DWT.

2. Second, Chapter 4 developed a novel LiDAR-assisted deep 2-D CNN-BLSTM model for the ultra-short-term prediction of future wind turbine responses using upcoming sequences of full wind field components and hub-height wind speed time series before reaching the turbine blades as inputs. As a data-driven framework, the performance of the proposed model was determined solely by the potential interactions hidden in the wind field and time series data rather than the physical equations or predetermined distribution types. Thus, it could avoid the dual risks of model incorrectness or distribution type misspecification. The NREL 5-MW reference horizontal axis wind turbine with FAST were utilized for simulations. Realistic 3-D wind field components vectors were generated by NREL TurbSim. The proposed 2-D CNN-BLSTM model was designed for ultra-short-term forecasting of wind turbine response and showed the high-quality outputs with the smallest metrics. For example, it demonstrated 78% and 75% improvement in RMSE when compared with single BLSTM and 2-D CNN models, respectively. The proposed model employed 2-D-CNN and BLSTM networks to better handle complex spatial-temporal features from highly variable wind data compared to conventional forecasting methods which simply used historical time series data. The main advantage of the proposed model over other deep learning-based forecasting methods was that it used wind preview information provided by LIDAR as an advanced remote sensing wind measurement technology. Thus, it could be helpful for wind farm operators as an efficient tool in yaw misalignment and deloading control strategies.
3. Third, Chapter 5 developed a comprehensive economic assessment model for a CAES-PV facility participating in the energy market based on the

DRL framework. Due to the nonconvex nature and highly intermittent parameters involved in the scheduling problem, the DQN agent was introduced to perform optimal self-scheduling of the CAES-PV system incorporating the thermodynamic characteristics of the system. To address the uncertainties of electricity price and PV power output, especially during cloudy days, a novel hybrid 2D CNN BLSTM model was adopted to predict the price and solar irradiance more accurately. Case studies using real-world data demonstrated that a well-trained DQN agent is capable of providing high profitability by making optimal dynamic decisions, which makes the proposed approach meaningful to the smart energy system industry.

4. Fourth, in Chapter 6, the optimal energy management problem of a PV integrated energy hub was studied. A novel DDPG+2D-CNN-BLSTM approach as a fully model-free and data-driven DRL framework was presented to provide an intelligent control strategy. Due to the nonconvex nature and highly intermittent parameters involved in the energy hub scheduling problem like nonconvex feasible operating regions of CHP units, valve-point effects of power-only units, and fuel cell dynamic efficiency, the proposed hybrid method was introduced to perform more efficient and cost-effective operations. Moreover, a forecasting model based on CNN and BLSTM networks was developed to provide great potentials for the proposed DDPG-based agent to learn an optimal policy in an efficient way, especially during cloudy days with highly intermittent PV power generation. Case studies on typical summer and winter days demonstrated that, by using meteorological components and sky images, the proposed approach was able to follow sharp spikes accurately even during hours of highly fluctuating and random solar radiation. The simulation results demonstrated that the continuous decision-making provided by the proposed DRL-based control strategy is approximately 15% more cost effective than that of the DQN-based method.

- Finally, Chapter 7 presented SFNAS-DDPG as an improved actor-critic DRL framework for the optimal scheduling and operation of a multi-source multi-product facility, taking into account nonlinear characteristics of the facility components such as biogas production thermodynamics, dynamic efficiency of fuel cells, valve admission behavior of power generation systems, and CHPs' non-convex operation regions. To help the DDPG agent choose the most efficient control policy, especially when PV power is highly intermittent on cloudy days, a hybrid CNN-GRU forecasting model that captures high levels of abstraction from sky images and numerical measurements was developed and employed. The novel SFNAS technique was proposed to learn the architecture and model parameters of the representation network. By utilizing supervisor-led training loss reshaping, the proposed SFNAS approach could be used directly to determine the optimal architecture based on the federated settings. As a result of our case studies, the proposed strategy, by selecting different network structures, was more accurate than the respective baseline forecasting methods. Consequently, the SFNAS-DDPG method had \$4,590 per day average operating costs, which shows a 4.79% improvement over the baseline model (DRL+State-of-the-art).

8.2 Future Work

The following research studies can be conducted in continuation of the work presented in this thesis:

- Improving the time series wind speed forecasting accuracy by taking into account further feature extraction methodologies such as data clustering methods.
- Extending the proposed forecasting methodology to offshore wind prediction and considering the sea current level as an external input.
- Applying DRL-based methods to a multi-agent setting, targeted to pro-

vide optimal energy management strategies for a group of energy hubs.

4. Enhancing the generalization performance of DRL-based scheduling methods so they can adapt to large variations in environmental conditions, especially extreme weather conditions.
5. Expanding the proposed SFNAS approach by replacing the proposed EA-based NAS with heterogeneous NAS methods.

Bibliography

- [1] M. Abadi, P. Barham, J. Chen, Z. Chen, A. Davis, J. Dean, M. Devin, S. Ghemawat, G. Irving, M. Isard, et al. Tensorflow: A system for large-scale machine learning. In *12th {USENIX} symposium on operating systems design and implementation ({OSDI} 16)*, pages 265–283, 2016.
- [2] M. Abdel-Nasser, K. Mahmoud, and M. Lehtonen. Reliable solar irradiance forecasting approach based on choquet integral and deep LSTMs. *IEEE Transactions on Industrial Informatics*, 17(3):1873–1881, 2020.
- [3] M. Ahrarinouri, M. Rastegar, and A. R. Seifi. Multiagent reinforcement learning for energy management in residential buildings. *IEEE Transactions on Industrial Informatics*, 17(1):659–666, 2020.
- [4] M. Alipour, K. Zare, H. Zareipour, and H. Seyedi. Hedging Strategies for Heat and Electricity Consumers in the Presence of Real-Time Demand Response Programs. *IEEE Transactions on Sustainable Energy*, 10(3):1262–1270, 2019.
- [5] D. Allen, A. Tomlin, C. Bale, A. Skea, S. Vosper, and M. Gallani. A boundary layer scaling technique for estimating near-surface wind energy using numerical weather prediction and wind map data. *Applied Energy*, 208:1246–1257, 2017.
- [6] S. Atef and A. B. Eltawil. Assessment of stacked unidirectional and bidirectional long short-term memory networks for electricity load forecasting. *Electric Power Systems Research*, 187:106489, 2020.

- [7] A. Attarha, N. Amjadi, S. Dehghan, and B. Vatani. Adaptive robust self-scheduling for a wind producer with compressed air energy storage. *IEEE Transactions on Sustainable Energy*, 9(4):1659–1671, 2018.
- [8] H. B. Azad, S. Mekhilef, and V. G. Ganapathy. Long-Term Wind Speed Forecasting and General Pattern Recognition Using Neural Networks. *IEEE Transactions on Sustainable Energy*, 5(2):546–553, 2014.
- [9] B. Baker, O. Gupta, N. Naik, and R. Raskar. Designing neural network architectures using reinforcement learning. *arXiv preprint arXiv:1611.02167*, 2016.
- [10] B. Baker, O. Gupta, R. Raskar, and N. Naik. Accelerating neural architecture search using performance prediction. *arXiv preprint arXiv:1705.10823*, 2017.
- [11] M. Basu. Combined Heat and Power Economic Dispatch by Using Differential Evolution. *Electric Power Components and Systems*, 38(8):996–1004, 2010.
- [12] G. Bender, P.-J. Kindermans, B. Zoph, V. Vasudevan, and Q. Le. Understanding and simplifying one-shot architecture search. In *International conference on machine learning*, pages 550–559. PMLR, 2018.
- [13] A. Brock, T. Lim, J. M. Ritchie, and N. Weston. Smash: one-shot model architecture search through hypernetworks. *arXiv preprint arXiv:1708.05344*, 2017.
- [14] V.-H. Bui, A. Hussain, and H.-M. Kim. Double Deep \mathcal{Q} -Learning-Based Distributed Operation of Battery Energy Storage System Considering Uncertainties. *IEEE Transactions on Smart Grid*, 11(1):457–469, 2020.

- [15] H. Cai, L. Zhu, and S. Han. Proxylessnas: Direct neural architecture search on target task and hardware. *arXiv preprint arXiv:1812.00332*, 2018.
- [16] J. Cao, C. Crozier, M. McCulloch, and Z. Fan. Optimal Design and Operation of a Low Carbon Community Based Multi-Energy Systems Considering EV Integration. *IEEE Transactions on Sustainable Energy*, 10(3):1217–1226, 2019.
- [17] J. Cao, D. Harrold, Z. Fan, T. Morstyn, D. Healey, and K. Li. Deep reinforcement learning-based energy storage arbitrage with accurate lithium-ion battery degradation model. *IEEE Transactions on Smart Grid*, 11(5):4513–4521, 2020.
- [18] J. Cao, D. Harrold, Z. Fan, T. Morstyn, D. Healey, and K. Li. Deep Reinforcement Learning-Based Energy Storage Arbitrage With Accurate Lithium-Ion Battery Degradation Model. *IEEE Transactions on Smart Grid*, 11(5):4513–4521, 2020.
- [19] M.-R. Chen, G.-Q. Zeng, K.-D. Lu, and J. Weng. A Two-Layer Nonlinear Combination Method for Short-Term Wind Speed Prediction Based on ELM, ENN, and LSTM. *IEEE Internet of Things Journal*, 6(4):6997–7010, 2019.
- [20] P. Chen, T. Pedersen, B. Bak-Jensen, and Z. Chen. ARIMA-Based Time Series Model of Stochastic Wind Power Generation. *IEEE Transactions on Power Systems*, 25(2):667–676, 2010.
- [21] Y. Cheng, N. Zhang, Z. Lu, and C. Kang. Planning Multiple Energy Systems Toward Low-Carbon Society: A Decentralized Approach. *IEEE Transactions on Smart Grid*, 10(5):4859–4869, 2019.
- [22] B. Cleary, A. Duffy, A. OConnor, M. Conlon, and V. Fthenakis. Assessing the economic benefits of compressed air energy storage for mit-

- igating wind curtailment. *IEEE Transactions on Sustainable Energy*, 6(3):1021–1028, 2015.
- [23] A. Clifton, P. Clive, J. Gottschall, D. Schlipf, E. Simley, L. Simmons, D. Stein, D. Trabucchi, N. Vasiljevic, and I. Würth. IEA Wind Task 32: Wind lidar identifying and mitigating barriers to the adoption of wind lidar. *Remote Sensing*, 10(3):406, 2018.
- [24] M. Z. De Souza, C. A. Canizares, and K. Bhattacharya. Self-Scheduling Models of a CAES Facility Under Uncertainties. *IEEE Transactions on Power Systems*, 2021.
- [25] A. Dolatabadi, H. Abdeltawab, and Y. A.-R. I. Mohamed. Hybrid deep learning-based model for wind speed forecasting based on DWPT and bidirectional LSTM network. *IEEE Access*, 8:229219–229232, 2020.
- [26] A. Dolatabadi, H. Abdeltawab, and Y. A.-R. I. Mohamed. Deep Spatial-Temporal 2-D CNN-BLSTM Model for Ultrashort-Term LiDAR-Assisted Wind Turbine’s Power and Fatigue Load Forecasting. *IEEE Transactions on Industrial Informatics*, 18(4):2342–2353, 2021.
- [27] A. Dolatabadi, H. Abdeltawab, and Y. A.-R. I. Mohamed. A Novel Model-Free Deep Reinforcement Learning Framework for Energy Management of a PV Integrated Energy Hub. *IEEE Transactions on Power Systems*, pages 1–13, 2022.
- [28] A. Dolatabadi, H. Abdeltawab, and Y. A.-R. I. Mohamed. Deep Reinforcement Learning-Based Self-scheduling Strategy for a CAES-PV System Using Accurate Sky Images-based Forecasting. *IEEE Transactions on Power Systems*, 2022.
- [29] A. Dolatabadi, H. H. Abdeltawab, and Y. A.-R. I. Mohamed. Deep Reinforcement Learning-Based Self-scheduling Strategy for a CAES-PV System Using Accurate Sky Images-based Forecasting. *IEEE Transactions on Power Systems*, 2022.

- [30] A. Dolatabadi, M. Jadidbonab, and B. Mohammadi-ivatloo. Short-term scheduling strategy for wind-based energy hub: a hybrid stochastic/IGDT approach. *IEEE Transactions on Sustainable Energy*, 10(1):438–448, 2018.
- [31] A. Dolatabadi, M. Jadidbonab, and B. Mohammadi-ivatloo. Short-Term Scheduling Strategy for Wind-Based Energy Hub: A Hybrid Stochastic/IGDT Approach. *IEEE Transactions on Sustainable Energy*, 10(1):438–448, 2019.
- [32] A. Dolatabadi, B. Mohammadi-ivatloo, M. Abapour, and S. Tohidi. Optimal Stochastic Design of Wind Integrated Energy Hub. *IEEE Transactions on Industrial Informatics*, 13(5):2379–2388, 2017.
- [33] B. Doucoure, K. Agbossou, and A. Cardenas. Time series prediction using artificial wavelet neural network and multi-resolution analysis: Application to wind speed data. *Renewable Energy*, 92:202–211, 2016.
- [34] Y. Du and F. Li. Intelligent Multi-Microgrid Energy Management Based on Deep Neural Network and Model-Free Reinforcement Learning. *IEEE Transactions on Smart Grid*, 11(2):1066–1076, 2020.
- [35] J. Duan, D. Shi, R. Diao, H. Li, Z. Wang, B. Zhang, D. Bian, and Z. Yi. Deep-Reinforcement-Learning-Based Autonomous Voltage Control for Power Grid Operations. *IEEE Transactions on Power Systems*, 35(1):814–817, 2020.
- [36] J. Duan, H. Xu, and W. Liu. Q-Learning-Based Damping Control of Wide-Area Power Systems Under Cyber Uncertainties. *IEEE Transactions on Smart Grid*, 9(6):6408–6418, 2018.
- [37] S. Eckroad and I. Gyuk. EPRI-DOE handbook of energy storage for transmission & distribution applications. *Electric Power Research Institute, Inc*, pages 3–35, 2003.

- [38] M. El-Sharkh, M. Tanrioven, A. Rahman, and M. Alam. Economics of hydrogen production and utilization strategies for the optimal operation of a grid-parallel PEM fuel cell power plant. *International Journal of Hydrogen Energy*, 35(16):8804–8814, 2010.
- [39] T. Elsken, J. H. Metzen, and F. Hutter. Neural architecture search: A survey. *The Journal of Machine Learning Research*, 20(1):1997–2017, 2019.
- [40] C. Feng, M. Cui, B.-M. Hodge, S. Lu, H. F. Hamann, and J. Zhang. Unsupervised clustering-based short-term solar forecasting. *IEEE Transactions on Sustainable Energy*, 10(4):2174–2185, 2018.
- [41] P. A. Fleming, A. Scholbrock, A. Jehu, S. Davoust, E. Osler, A. D. Wright, and A. Clifton. Field-test results using a nacelle-mounted lidar for improving wind turbine power capture by reducing yaw misalignment. In *J. Phys. Conf. Ser.*, volume 524, page 012002. IOP Publishing, 2014.
- [42] A. M. Fraser. Reconstructing attractors from scalar time series: A comparison of singular system and redundancy criteria. *Physica D: Nonlinear Phenomena*, 34(3):391–404, 1989.
- [43] P. Gangwar, A. Mallick, S. Chakrabarti, and S. N. Singh. Short-term forecasting-based network reconfiguration for unbalanced distribution systems with distributed generators. *IEEE Trans. Ind. Inf.*, 16(7):4378–4389, 2019.
- [44] S. Gao, C. Xiang, M. Yu, K. T. Tan, and T. H. Lee. Online Optimal Power Scheduling of a Microgrid via Imitation Learning. *IEEE Transactions on Smart Grid*, 13(2):861–876, 2022.
- [45] A. Ghadertootoonchi, M. M. Aghtaie, and M. Davoudi. A Hybrid Linear Programming-Reinforcement Learning Method for Optimal Energy Hub Management. *IEEE Trans. Smart Grid*, pages 1–1, 2022.

- [46] S. Ghavidel, M. J. Ghadi, A. Azizivahed, J. Aghaei, L. Li, and J. Zhang. Risk-constrained bidding strategy for a joint operation of wind power and CAES aggregators. *IEEE Transactions on Sustainable Energy*, 11(1):457–466, 2019.
- [47] I. González-Aparicio, F. Monforti, P. Volker, A. Zucker, F. Careri, T. Huld, and J. Badger. Simulating European wind power generation applying statistical downscaling to reanalysis data. *Applied Energy*, 199:155–168, 2017.
- [48] I. Goodfellow, Y. Bengio, A. Courville, and Y. Bengio. *Deep learning*, volume 1. MIT press Cambridge, 2016.
- [49] F. S. Gorostiza and F. M. Gonzalez-Longatt. Deep reinforcement learning-based controller for SOC management of multi-electrical energy storage system. *IEEE Transactions on Smart Grid*, 11(6):5039–5050, 2020.
- [50] S. J. Hadi, M. Tombul, S. Q. Salih, N. Al-Ansari, and Z. M. Yaseen. The Capacity of the Hybridizing Wavelet Transformation Approach With Data-Driven Models for Modeling Monthly-Scale Streamflow. *IEEE Access*, 8:101993–102006, 2020.
- [51] L. Han, C. E. Romero, and Z. Yao. Wind power forecasting based on principle component phase space reconstruction. *Renewable Energy*, 81:737–744, 2015.
- [52] A. D. Hansen, F. Iov, P. E. Sørensen, N. A. Cutululis, C. Jauch, and F. Blaabjerg. Dynamic wind turbine models in power system simulation tool DIgSILENT. 2007.
- [53] M. Harris, M. Hand, and A. Wright. Lidar for turbine control. *National Renewable Energy Laboratory, Golden, CO, Report No. NREL/TP-500-39154*, 2006.

- [54] M. Hemmati, B. Mohammadi-Ivatloo, M. Abapour, and M. Shafiee. Thermodynamic modeling of compressed air energy storage for energy and reserve markets. *Applied Thermal Engineering*, 193:116948, 2021.
- [55] S. Hochreiter and J. Schmidhuber. Long Short-Term Memory. *Neural Computation*, 9(8):1735–1780, 1997.
- [56] Y.-Y. Hong and T. R. A. Satriani. Day-ahead spatiotemporal wind speed forecasting using robust design-based deep learning neural network. *Energy*, 209:118441, 2020.
- [57] H. Huang, M. Lin, L. T. Yang, and Q. Zhang. Autonomous Power Management With Double-Q Reinforcement Learning Method. *IEEE Transactions on Industrial Informatics*, 16(3):1938–1946, 2020.
- [58] Q. Huang, R. Huang, W. Hao, J. Tan, R. Fan, and Z. Huang. Adaptive Power System Emergency Control Using Deep Reinforcement Learning. *IEEE Transactions on Smart Grid*, 11(2):1171–1182, 2020.
- [59] M. Jadidbonab, A. Dolatabadi, B. Mohammadi-Ivatloo, M. Abapour, and S. Asadi. Risk-constrained energy management of PV integrated smart energy hub in the presence of demand response program and compressed air energy storage. *IET Renewable Power Generation*, 13(6):998–1008, 2019.
- [60] M. Jadidbonab, B. Mohammadi-Ivatloo, M. Marzband, and P. Siano. Short-Term Self-Scheduling of Virtual Energy Hub Plant Within Thermal Energy Market. *IEEE Transactions on Industrial Electronics*, 68(4):3124–3136, 2021.
- [61] A. Jager, D.; Andreas. NREL National Wind Technology Center (NWTC): M2 Tower; Boulder, Colorado (Data). *NREL Report No. DA-5500-56489*, 1996.

- [62] H. Jahangir, H. Tayarani, S. S. Gougheri, M. A. Golkar, A. Ahmadian, and A. Elkamel. Deep learning-based forecasting approach in smart grids with microclustering and bidirectional LSTM network. *IEEE Transactions on Industrial Electronics*, 68(9):8298–8309, 2020.
- [63] H. Jahangir, H. Tayarani, S. S. Gougheri, M. A. Golkar, A. Ahmadian, and A. Elkamel. Deep Learning-Based Forecasting Approach in Smart Grids With Microclustering and Bidirectional LSTM Network. *IEEE Transactions on Industrial Electronics*, 68(9):8298–8309, 2021.
- [64] H. Jahangir, H. Tayarani, S. S. Gougheri, M. A. Golkar, A. Ahmadian, and A. Elkamel. Deep Learning-Based Forecasting Approach in Smart Grids With Microclustering and Bidirectional LSTM Network. *IEEE Transactions on Industrial Electronics*, 68(9):8298–8309, 2021.
- [65] M. S. Javadi, M. Lotfi, A. E. Nezhad, A. Anvari-Moghaddam, J. M. Guerrero, and J. P. S. Catalão. Optimal Operation of Energy Hubs Considering Uncertainties and Different Time Resolutions. *IEEE Transactions on Industry Applications*, 56(5):5543–5552, 2020.
- [66] B. J. Jonkman. TurbSim user’s guide: Version 1.50. Technical report, National Renewable Energy Lab.(NREL), Golden, CO (United States), 2009.
- [67] J. Jonkman, S. Butterfield, W. Musial, and G. Scott. Definition of a 5-MW reference wind turbine for offshore system development. Technical report, National Renewable Energy Lab.(NREL), Golden, CO (United States), 2009.
- [68] J. M. Jonkman and M. L. Buhl Jr. FAST user’s guide-updated august 2005. Technical report, National Renewable Energy Lab.(NREL), Golden, CO (United States), 2005.
- [69] H. Khaloie, J.-F. Toubeau, F. Vallée, C. S. Lai, and L. L. Lai. An Innovative Coalitional Trading Model for a Biomass Power Plant Paired With

- Green Energy Resources. *IEEE Trans. Sustainable Energy*, 13(2):892–904, 2022.
- [70] H. Khaloie, F. Vallée, C. S. Lai, J.-F. Toubeau, and N. D. Hatziargyriou. Day-Ahead and Intraday Dispatch of an Integrated Biomass-Concentrated Solar System: A Multi-Objective Risk-Controlling Approach. *IEEE Trans. Power Syst.*, 37(1):701–714, 2022.
- [71] H. Khani, M. R. D. Zadeh, and A. H. Hajimiragha. Transmission congestion relief using privately owned large-scale energy storage systems in a competitive electricity market. *IEEE Transactions on Power Systems*, 31(2):1449–1458, 2015.
- [72] R. Khatami, K. Oikonomou, and M. Parvania. Look-ahead optimal participation of compressed air energy storage in day-ahead and real-time markets. *IEEE Transactions on Sustainable Energy*, 11(2):682–692, 2019.
- [73] M. Khodayar, O. Kaynak, and M. E. Khodayar. Rough deep neural architecture for short-term wind speed forecasting. *IEEE Transactions on Industrial Informatics*, 13(6):2770–2779, 2017.
- [74] M. Khodayar, O. Kaynak, and M. E. Khodayar. Rough Deep Neural Architecture for Short-Term Wind Speed Forecasting. *IEEE Transactions on Industrial Informatics*, 13(6):2770–2779, 2017.
- [75] M. Khodayar and J. Wang. Spatio-temporal graph deep neural network for short-term wind speed forecasting. *IEEE Trans. Sustainable Energy*, 10(2):670–681, 2018.
- [76] M. Khodayar and J. Wang. Spatio-Temporal Graph Deep Neural Network for Short-Term Wind Speed Forecasting. *IEEE Transactions on Sustainable Energy*, 10(2):670–681, 2019.

- [77] M. Khodayar, J. Wang, and M. Manthouri. Interval Deep Generative Neural Network for Wind Speed Forecasting. *IEEE Transactions on Smart Grid*, 10(4):3974–3989, 2019.
- [78] S. Kim and H. Lim. Reinforcement Learning Based Energy Management Algorithm for Smart Energy Buildings. *Energies*, 11(8):2010, 2018.
- [79] J. Konečný, H. B. McMahan, F. X. Yu, P. Richtárik, A. T. Suresh, and D. Bacon. Federated learning: Strategies for improving communication efficiency. *arXiv preprint arXiv:1610.05492*, 2016.
- [80] W. Kong, Z. Y. Dong, Y. Jia, D. J. Hill, Y. Xu, and Y. Zhang. Short-Term Residential Load Forecasting Based on LSTM Recurrent Neural Network. *IEEE Transactions on Smart Grid*, 10(1):841–851, 2019.
- [81] B. Krause, L. Lu, I. Murray, and S. Renals. Multiplicative LSTM for sequence modelling. *arXiv preprint arXiv:1609.07959*, 2016.
- [82] Y. LeCun, Y. Bengio, and G. Hinton. Deep learning. *nature*, 521(7553):436–444, 2015.
- [83] L. Lei, Y. Tan, G. Dahlenburg, W. Xiang, and K. Zheng. Dynamic Energy Dispatch Based on Deep Reinforcement Learning in IoT-Driven Smart Isolated Microgrids. *IEEE Internet of Things Journal*, 8(10):7938–7953, 2021.
- [84] C. Li, G. Tang, X. Xue, A. Saeed, and X. Hu. Short-Term Wind Speed Interval Prediction Based on Ensemble GRU Model. *IEEE Trans. Sustainable Energy*, 11(3):1370–1380, 2020.
- [85] C. Li, H. Yang, M. Shahidehpour, Z. Xu, B. Zhou, Y. Cao, and L. Zeng. Optimal Planning of Islanded Integrated Energy System With Solar-Biogas Energy Supply. *IEEE Transactions on Sustainable Energy*, 11(4):2437–2448, 2020.

- [86] G. Li, G. Qian, I. C. Delgadillo, M. Muller, A. Thabet, and B. Ghanem. Sgas: Sequential greedy architecture search. In *Proceedings of the IEEE/CVF Conference on Computer Vision and Pattern Recognition*, pages 1620–1630, 2020.
- [87] G. Li and J. Shi. On comparing three artificial neural networks for wind speed forecasting. *Applied Energy*, 87(7):2313–2320, 2010.
- [88] H. Li, Z. Ren, Y. Xu, W. Li, and B. Hu. A Multi-Data Driven Hybrid Learning Method for Weekly Photovoltaic Power Scenario Forecast. *IEEE Transactions on Sustainable Energy*, 13(1):91–100, 2022.
- [89] Y. Liang, C. Guo, Z. Ding, and H. Hua. Agent-Based Modeling in Electricity Market Using Deep Deterministic Policy Gradient Algorithm. *IEEE Transactions on Power Systems*, 35(6):4180–4192, 2020.
- [90] Y. Liang, W. Wei, and C. Wang. A Generalized Nash Equilibrium Approach for Autonomous Energy Management of Residential Energy Hubs. *IEEE Transactions on Industrial Informatics*, 15(11):5892–5905, 2019.
- [91] T. P. Lillicrap, J. J. Hunt, A. Pritzel, N. Heess, T. Erez, Y. Tassa, D. Silver, and D. Wierstra. Continuous control with deep reinforcement learning, 2015.
- [92] K.-P. Lin, P.-F. Pai, and Y.-J. Ting. Deep Belief Networks With Genetic Algorithms in Forecasting Wind Speed. *IEEE Access*, 7:99244–99253, 2019.
- [93] H. Liu, K. Simonyan, and Y. Yang. Darts: Differentiable architecture search. *arXiv preprint arXiv:1806.09055*, 2018.
- [94] T. Liu, X. Hu, W. Hu, and Y. Zou. A heuristic planning reinforcement learning-based energy management for power-split plug-in hybrid elec-

- tric vehicles. *IEEE Transactions on Industrial Informatics*, 15(12):6436–6445, 2019.
- [95] Y. Liu, H. Qin, Z. Zhang, S. Pei, Z. Jiang, Z. Feng, and J. Zhou. Probabilistic spatiotemporal wind speed forecasting based on a variational bayesian deep learning model. *Applied Energy*, 260:114259, 2020.
- [96] Y. Liu, Y. Sun, B. Xue, M. Zhang, G. G. Yen, and K. C. Tan. A Survey on Evolutionary Neural Architecture Search. *IEEE Trans. Neural Networks Learn. Syst.*, pages 1–21, 2021.
- [97] J. Ma, M. Yang, and Y. Lin. Ultra-Short-Term Probabilistic Wind Turbine Power Forecast Based on Empirical Dynamic Modeling. *IEEE Transactions on Sustainable Energy*, 11(2):906–915, 2020.
- [98] L. Ma, N. Liu, J. Zhang, and L. Wang. Real-Time Rolling Horizon Energy Management for the Energy-Hub-Coordinated Prosumer Community From a Cooperative Perspective. *IEEE Transactions on Power Systems*, 34(2):1227–1242, 2019.
- [99] A. Meng, J. Ge, H. Yin, and S. Chen. Wind speed forecasting based on wavelet packet decomposition and artificial neural networks trained by crisscross optimization algorithm. *Energy Conversion and Management*, 114:75–88, 2016.
- [100] V. Mnih, K. Kavukcuoglu, D. Silver, A. A. Rusu, J. Veness, M. G. Bellemare, A. Graves, M. Riedmiller, A. K. Fidjeland, G. Ostrovski, et al. Human-level control through deep reinforcement learning. *nature*, 518(7540):529–533, 2015.
- [101] H. Mo, L. L. Custode, and G. Iacca. Evolutionary neural architecture search for remaining useful life prediction. *Applied Soft Computing*, 108:107474, 2021.

- [102] S. Moazeni, A. H. Miragha, and B. Defourny. A Risk-Averse Stochastic Dynamic Programming Approach to Energy Hub Optimal Dispatch. *IEEE Transactions on Power Systems*, 34(3):2169–2178, 2019.
- [103] E. Mocanu, D. C. Mocanu, P. H. Nguyen, A. Liotta, M. E. Webber, M. Gibescu, and J. G. Slootweg. On-line building energy optimization using deep reinforcement learning. *IEEE transactions on smart grid*, 10(4):3698–3708, 2018.
- [104] E. Mocanu, D. C. Mocanu, P. H. Nguyen, A. Liotta, M. E. Webber, M. Gibescu, and J. G. Slootweg. On-Line Building Energy Optimization Using Deep Reinforcement Learning. *IEEE Transactions on Smart Grid*, 10(4):3698–3708, 2019.
- [105] M. A. Mohandes and S. Rehman. Wind speed extrapolation using machine learning methods and LiDAR measurements. *IEEE Access*, 6:77634–77642, 2018.
- [106] M. Moradi-Dalvand, M. Nazari-Heris, B. Mohammadi-ivatloo, S. Galavani, and A. Rabiee. A Two-Stage Mathematical Programming Approach for the Solution of Combined Heat and Power Economic Dispatch. *IEEE Systems Journal*, 14(2):2873–2881, 2020.
- [107] M. Nazari-Heris, S. Abapour, and B. Mohammadi-Ivatloo. Optimal economic dispatch of FC-CHP based heat and power micro-grids. *Applied Thermal Engineering*, 114:756–769, 2017.
- [108] M. Nehrir, C. Wang, K. Strunz, H. Aki, R. Ramakumar, J. Bing, Z. Miao, and Z. Salameh. A review of hybrid renewable/alternative energy systems for electric power generation: Configurations, control, and applications. *IEEE transactions on sustainable energy*, 2(4):392–403, 2011.
- [109] M. H. Nehrir, C. Wang, K. Strunz, H. Aki, R. Ramakumar, J. Bing, Z. Miao, and Z. Salameh. A Review of Hybrid Renewable/Alternative

- Energy Systems for Electric Power Generation: Configurations, Control, and Applications. *IEEE Transactions on Sustainable Energy*, 2(4):392–403, 2011.
- [110] S. Nojavan, A. Najafi-Ghalelou, M. Majidi, and K. Zare. Optimal bidding and offering strategies of merchant compressed air energy storage in deregulated electricity market using robust optimization approach. *Energy*, 142:250–257, 2018.
 - [111] D. J. Olsen, N. Zhang, C. Kang, M. A. Ortega-Vazquez, and D. S. Kirschen. Planning Low-Carbon Campus Energy Hubs. *IEEE Transactions on Power Systems*, 34(3):1895–1907, 2019.
 - [112] M. Z. Oskouei, B. Mohammadi-Ivatloo, M. Abapour, M. Shafiee, and A. Anvari-Moghaddam. Strategic Operation of a Virtual Energy Hub With the Provision of Advanced Ancillary Services in Industrial Parks. *IEEE Transactions on Sustainable Energy*, 12(4):2062–2073, 2021.
 - [113] A. Peña, C. B. Hasager, J. Lange, J. Anger, M. Badger, F. Bingöl, O. Bischoff, J.-P. Cariou, F. Dunne, S. Emeis, et al. *Remote sensing for wind energy*. DTU Wind Energy, 2013.
 - [114] H. Pham, M. Guan, B. Zoph, Q. Le, and J. Dean. Efficient neural architecture search via parameters sharing. In *International conference on machine learning*, pages 4095–4104. PMLR, 2018.
 - [115] D. Polap. An adaptive genetic algorithm as a supporting mechanism for microscopy image analysis in a cascade of convolution neural networks. *Applied Soft Computing*, 97:106824, 2020.
 - [116] D. Qiu, Z. Dong, X. Zhang, Y. Wang, and G. Strbac. Safe reinforcement learning for real-time automatic control in a smart energy-hub. *Applied Energy*, 309:118403, 2022.

- [117] E. Ranganai and C. Sigauke. Capturing Long-Range Dependence and Harmonic Phenomena in 24-Hour Solar Irradiance Forecasting: A Quantile Regression Robustification via Forecasts Combination Approach. *IEEE Access*, 8:172204–172218, 2020.
- [118] E. Real, S. Moore, A. Selle, S. Saxena, Y. L. Suematsu, J. Tan, Q. V. Le, and A. Kurakin. Large-scale evolution of image classifiers. In *International Conference on Machine Learning*, pages 2902–2911. PMLR, 2017.
- [119] A. Reis and A. da Silva. Feature extraction via multiresolution analysis for short-term load forecasting. *IEEE Transactions on Power Systems*, 20(1):189–198, 2005.
- [120] P. Ren, Y. Xiao, X. Chang, P.-Y. Huang, Z. Li, X. Chen, and X. Wang. A comprehensive survey of neural architecture search: Challenges and solutions. *ACM Computing Surveys (CSUR)*, 54(4):1–34, 2021.
- [121] A. Saeed, C. Li, M. Danish, S. Rubaiee, G. Tang, Z. Gan, and A. Ahmed. Hybrid Bidirectional LSTM Model for Short-Term Wind Speed Interval Prediction. *IEEE Access*, 8:182283–182294, 2020.
- [122] H. Samet, S. Katabipoor, M. Afrasiabi, S. Afrasiabi, and M. Mohammadi. Deep Learning Forecaster based Controller for SVC: Wind Farm Flicker Mitigation. *IEEE Trans. Ind. Inf.*, 2020.
- [123] F. Sanchez Gorostiza and F. M. Gonzalez-Longatt. Deep Reinforcement Learning-Based Controller for SOC Management of Multi-Electrical Energy Storage System. *IEEE Transactions on Smart Grid*, 11(6):5039–5050, 2020.
- [124] M. J. Sanjari, H. B. Gooi, and N.-K. C. Nair. Power generation forecast of hybrid PV–wind system. *IEEE Transactions on Sustainable Energy*, 11(2):703–712, 2019.

- [125] D. Schlipf, P. Fleming, F. Haizmann, A. Scholbrock, M. Hofsäß, A. Wright, and P. W. Cheng. Field testing of feedforward collective pitch control on the CART2 using a nacelle-based lidar scanner. In *J. Phys. Conf. Ser.*, volume 555, page 012090. IOP Publishing, 2014.
- [126] S. Shafiee, H. Zareipour, and A. M. Knight. Considering thermodynamic characteristics of a CAES facility in self-scheduling in energy and reserve markets. *IEEE Transactions on Smart Grid*, 9(4):3476–3485, 2016.
- [127] S. Shafiee, H. Zareipour, A. M. Knight, N. Amjadi, and B. Mohammadi-Ivatloo. Risk-constrained bidding and offering strategy for a merchant compressed air energy storage plant. *IEEE Transactions on Power Systems*, 32(2):946–957, 2016.
- [128] S. Sharda, M. Singh, and K. Sharma. RSAM: Robust Self-Attention Based Multi-Horizon Model for Solar Irradiance Forecasting. *IEEE Transactions on Sustainable Energy*, 12(2):1394–1405, 2021.
- [129] X. Shi, X. Lei, Q. Huang, S. Huang, K. Ren, and Y. Hu. Hourly Day-Ahead Wind Power Prediction Using the Hybrid Model of Variational Model Decomposition and Long Short-Term Memory. *Energies*, 11(11), 2018.
- [130] Z. Shi, H. Liang, and V. Dinavahi. Direct Interval Forecast of Uncertain Wind Power Based on Recurrent Neural Networks. *IEEE Transactions on Sustainable Energy*, 9(3):1177–1187, 2018.
- [131] Z. Shi, H. Liang, and V. Dinavahi. Direct Interval Forecast of Uncertain Wind Power Based on Recurrent Neural Networks. *IEEE Transactions on Sustainable Energy*, 9(3):1177–1187, 2018.
- [132] T. Stoffel and A. Andreas. NREL Solar Radiation Research Laboratory (SRRL): Baseline Measurement System (BMS); Golden, Colorado (Data).

- [133] T. Stoffel and A. Andreas. NREL Solar Radiation Research Laboratory (SRRL): Baseline Measurement System (BMS); Golden, Colorado (data). Technical report, National Renewable Energy Lab.(NREL), Golden, CO, USA, DA-5500-56488, 1981.
- [134] X. Sun and J. Qiu. Two-Stage Volt/Var Control in Active Distribution Networks With Multi-Agent Deep Reinforcement Learning Method. *IEEE Transactions on Smart Grid*, 12(4):2903–2912, 2021.
- [135] K. Swersky, D. Duvenaud, J. Snoek, F. Hutter, and M. A. Osborne. Raiders of the lost architecture: Kernels for Bayesian optimization in conditional parameter spaces. *arXiv preprint arXiv:1409.4011*, 2014.
- [136] S. Taheri, M. Jooshaki, and M. Moeini-Aghetaie. Long-term planning of integrated local energy systems using deep learning algorithms. *International Journal of Electrical Power and Energy Systems*, 129:106855, 2021.
- [137] S. Taheri, M. Jooshaki, and M. Moeini-Aghetaie. Long-term planning of integrated local energy systems using deep learning algorithms. *International Journal of Electrical Power Energy Systems*, 129:106855, 2021.
- [138] J.-F. Toubeau, J. Bottieau, F. Vallée, and Z. De Grève. Deep Learning-Based Multivariate Probabilistic Forecasting for Short-Term Scheduling in Power Markets. *IEEE Transactions on Power Systems*, 34(2):1203–1215, 2019.
- [139] Z. Wan, H. Li, H. He, and D. Prokhorov. Model-free real-time EV charging scheduling based on deep reinforcement learning. *IEEE Transactions on Smart Grid*, 10(5):5246–5257, 2018.
- [140] Z. Wan, H. Li, H. He, and D. Prokhorov. Model-Free Real-Time EV Charging Scheduling Based on Deep Reinforcement Learning. *IEEE Transactions on Smart Grid*, 10(5):5246–5257, 2019.

- [141] H. Wang, G. Wang, G. Li, J. Peng, and Y. Liu. Deep belief network based deterministic and probabilistic wind speed forecasting approach. *Applied Energy*, 182:80–93, 2016.
- [142] H. Wang, G. Wang, G. Li, J. Peng, and Y. Liu. Deep belief network based deterministic and probabilistic wind speed forecasting approach. *Applied Energy*, 182:80–93, 2016.
- [143] J. Wang, C. Jiang, K. Zhang, X. Hou, Y. Ren, and Y. Qian. Distributed Q-Learning Aided Heterogeneous Network Association for Energy-Efficient IIoT. *IEEE Transactions on Industrial Informatics*, 16(4):2756–2764, 2020.
- [144] J. Wang, H. Zhong, X. Lai, Q. Xia, Y. Wang, and C. Kang. Exploring key weather factors from analytical modeling toward improved solar power forecasting. *IEEE Transactions on Smart Grid*, 10(2):1417–1427, 2017.
- [145] L. Wang, Z. Zhang, H. Long, J. Xu, and R. Liu. Wind Turbine Gearbox Failure Identification With Deep Neural Networks. *IEEE Transactions on Industrial Informatics*, 13(3):1360–1368, 2017.
- [146] L. Wang, Z. Zhang, H. Long, J. Xu, and R. Liu. Wind Turbine Gearbox Failure Identification With Deep Neural Networks. *IEEE Transactions on Industrial Informatics*, 13(3):1360–1368, 2017.
- [147] Y. Wang, S. Lou, Y. Wu, M. Miao, and S. Wang. Operation strategy of a hybrid solar and biomass power plant in the electricity markets. *Electr. Power Syst. Res.*, 167:183–191, 2019.
- [148] Y. Wang, H. Tan, Y. Wu, and J. Peng. Hybrid Electric Vehicle Energy Management With Computer Vision and Deep Reinforcement Learning. *IEEE Transactions on Industrial Informatics*, 17(6):3857–3868, 2021.

- [149] M. Wistuba. Deep learning architecture search by neuro-cell-based evolution with function-preserving mutations. In *Joint European Conference on Machine Learning and Knowledge Discovery in Databases*, pages 243–258. Springer, 2018.
- [150] M. Wistuba, A. Rawat, and T. Pedapati. A survey on neural architecture search. *arXiv preprint arXiv:1905.01392*, 2019.
- [151] Y.-X. Wu, Q.-B. Wu, and J.-Q. Zhu. Data-driven wind speed forecasting using deep feature extraction and LSTM. *IET Renewable Power Generation*, 13(12):2062–2069, 2019.
- [152] Y.-X. Wu, Q.-B. Wu, and J.-Q. Zhu. Data-driven wind speed forecasting using deep feature extraction and LSTM. *IET Renewable Power Generation*, 13(12):2062–2069, 2019.
- [153] Y.-X. Wu, Q.-B. Wu, and J.-Q. Zhu. Data-driven wind speed forecasting using deep feature extraction and LSTM. *IET Renewable Power Gener.*, 13(12):2062–2069, 2019.
- [154] Z. Wu, Q. Li, and X. Xia. Multi-timescale Forecast of Solar Irradiance Based on Multi-task Learning and Echo State Network Approaches. *IEEE Transactions on Industrial Informatics*, 17(1):300–310, 2021.
- [155] L. Xiang, Z. Deng, and A. Hu. Forecasting Short-Term Wind Speed Based on IEWT-LSSVM Model Optimized by Bird Swarm Algorithm. *IEEE Access*, 7:59333–59345, 2019.
- [156] L. Xiang, J. Li, A. Hu, and Y. Zhang. Deterministic and probabilistic multi-step forecasting for short-term wind speed based on secondary decomposition and a deep learning method. *Energy Conversion and Management*, 220:113098, 2020.

- [157] D. Xu, B. Zhou, K. W. Chan, C. Li, Q. Wu, B. Chen, and S. Xia. Distributed Multienergy Coordination of Multimicrogrids With Biogas-Solar-Wind Renewables. *IEEE Trans. Ind. Inf.*, 15(6):3254–3266, 2019.
- [158] Z. Xue and Y. Xue. Multi long-short term memory models for short term traffic flow prediction. *IEICE TRANSACTIONS on Information and Systems*, 101(12):3272–3275, 2018.
- [159] M. Yan, N. Zhang, X. Ai, M. Shahidehpour, C. Kang, and J. Wen. Robust Two-Stage Regional-District Scheduling of Multi-carrier Energy Systems With a Large Penetration of Wind Power. *IEEE Transactions on Sustainable Energy*, 10(3):1227–1239, 2019.
- [160] H. Yang, C. Li, M. Shahidehpour, C. Zhang, B. Zhou, Q. Wu, and L. Zhou. Multistage Expansion Planning of Integrated Biogas and Electric Power Delivery System Considering the Regional Availability of Biomass. *IEEE Trans. Sustainable Energy*, 12(2):920–930, 2021.
- [161] Q. Yao, J. Liu, and Y. Hu. Optimized active power dispatching strategy considering fatigue load of wind turbines during de-loading operation. *IEEE Access*, 7:17439–17449, 2019.
- [162] S. Ye, J. Jiang, J. Li, Y. Liu, Z. Zhou, and C. Liu. Fault Diagnosis and Tolerance Control of Five-Level Nested NPP Converter Using Wavelet Packet and LSTM. *IEEE Transactions on Power Electronics*, 35(2):1907–1921, 2020.
- [163] Y. Yu, X. Han, M. Yang, and J. Yang. Probabilistic prediction of regional wind power based on spatiotemporal quantile regression. *IEEE Trans. Ind. Appl.*, 56(6):6117–6127, 2020.
- [164] A. Zela, A. Klein, S. Falkner, and F. Hutter. Towards automated deep learning: Efficient joint neural architecture and hyperparameter search. *arXiv preprint arXiv:1807.06906*, 2018.

- [165] L. Zhang and Q. Yang. A Method for Yaw Error Alignment of Wind Turbine Based on LiDAR. *IEEE Access*, 8:25052–25059, 2020.
- [166] W. Zhang, H. Yang, X. Bu, and L. Wang. Deep Learning for Mandarin-Tibetan Cross-Lingual Speech Synthesis. *IEEE Access*, 7:167884–167894, 2019.
- [167] P. Zhao, L. Gao, J. Wang, and Y. Dai. Energy efficiency analysis and off-design analysis of two different discharge modes for compressed air energy storage system using axial turbines. *Renewable Energy*, 85:1164–1177, 2016.
- [168] P. Zhao, C. Gu, Z. Cao, Z. Hu, X. Zhang, X. Chen, I. Hernando-Gil, and Y. Ding. Economic-Effective Multi-Energy Management Considering Voltage Regulation Networked With Energy Hubs. *IEEE Trans. Power Syst.*, 36(3):2503–2515, 2021.
- [169] P. Zhao, C. Gu, D. Huo, Y. Shen, and I. Hernando-Gil. Two-Stage Distributionally Robust Optimization for Energy Hub Systems. *IEEE Transactions on Industrial Informatics*, 16(5):3460–3469, 2020.
- [170] X. Zhao and B. Ye. Convolution wavelet packet transform and its applications to signal processing, journal = Digital Signal Processing. 20(5):1352–1364, 2010.
- [171] Z. Zhen, J. Liu, Z. Zhang, F. Wang, H. Chai, Y. Yu, X. Lu, T. Wang, and Y. Lin. Deep learning based surface irradiance mapping model for solar PV power forecasting using sky image. *IEEE Transactions on Industry Applications*, 56(4):3385–3396, 2020.
- [172] Z. Zhong, J. Yan, W. Wu, J. Shao, and C.-L. Liu. Practical Block-Wise Neural Network Architecture Generation. In *2018 IEEE/CVF Conference on Computer Vision and Pattern Recognition*, pages 2423–2432, 2018.

- [173] B. Zhou, D. Xu, C. Li, C. Y. Chung, Y. Cao, K. W. Chan, and Q. Wu. Optimal Scheduling of Biogas-Solar-Wind Renewable Portfolio for Multicarrier Energy Supplies. *IEEE Transactions on Power Systems*, 33(6):6229–6239, 2018.
- [174] S. Zhou, Z. Hu, W. Gu, M. Jiang, and X.-P. Zhang. Artificial intelligence based smart energy community management: A reinforcement learning approach. *CSEE J. Power Energy Syst*, 5(1):1–10, 2019.